NEUTRINO SIGNALS FROM DARK MATTER

by

Arif Emre Erkoca

A Dissertation Submitted to the Faculty of the

DEPARTMENT OF PHYSICS

In Partial Fulfillment of the Requirements
For the Degree of

DOCTOR OF PHILOSOPHY

In the Graduate College

THE UNIVERSITY OF ARIZONA

2010

THE UNIVERSITY OF ARIZONA
GRADUATE COLLEGE

As members of the Dissertation Committee, we certify that we have read the dissertation prepared by Arif Emre Erkoca
entitled Neutrino Signals from Dark Matter
and recommend that it be accepted as fulfilling the dissertation requirement for the Degree of Doctor of Philosophy.

Date: 2 December 2010
Ina Sarcevic

Date: 2 December 2010
Mary Hall Reno

Date: 2 December 2010
Michael Shupe

Date: 2 December 2010
Alex Cronin

Final approval and acceptance of this dissertation is contingent upon the candidate's submission of the final copies of the dissertation to the Graduate College.
I hereby certify that I have read this dissertation prepared under my direction and recommend that it be accepted as fulfilling the dissertation requirement.

Date: 2 December 2010
Dissertation Director: Ina Sarcevic

STATEMENT BY AUTHOR

This dissertation has been submitted in partial fulfillment of requirements for an advanced degree at the University of Arizona and is deposited in the University Library to be made available to borrowers under rules of the Library.

Brief quotations from this dissertation are allowable without special permission, provided that accurate acknowledgment of source is made. Requests for permission for extended quotation from or reproduction of this manuscript in whole or in part may be granted by the head of the major department or the Dean of the Graduate College when in his or her judgment the proposed use of the material is in the interests of scholarship. In all other instances, however, permission must be obtained from the author.

SIGNED: Arif Emre Erkoca

ACKNOWLEDGEMENTS

It is a great pleasure to thank my advisor Professor Ina Sarcevic for mentoring me throughout my graduate studies. I am very grateful for everything she has taught me and for her endless support. I would also like to thank Professor Mary Hall Reno and Professor Graciela Gelmini for the very useful discussions we had together, and for accepting me as their collaborator. I would also like to thank Professor Mary Hall Reno for traveling a long way to attend my defense. In addition, my thanks also go to Professor Michael Shupe and Professor Alex Cronin for being my committee members and providing me with very beneficial feedback.

My gratitude also goes to the Staff of the Department of Physics who has helped me over the last years.

Special thanks go to Tolga Guver for his valuable suggestions, and for helping me resolve some numerical problems. He and his wife Funda Guver have been my best friends and great support.

I would like to express my gratitude to Jean Claude Malterre for being my family in Tucson and having taken care of me since my first day in the US. I would also like to thank deeply Akash and Padma Taggarse, Ron and Linda Hill, as well as their families for considering me part of their families. They all occupy a special place in my heart for everything they have done for me.

I am so much grateful to my aunt Katibe Aytun and my uncle Alkut Aytun for sharing experiences that have always guided me.

I thank all my family and friends for their love and support, especially my grandmother Muazzez Celebi who raised me with all her love and care. I would like to acknowledge the support of my uncle Arif Celebi who has given me so much love and many creative ideas that have helped me see new horizons. I am so much grateful to my wife Antonella Cassia for her love, support and care since the day we got married. She has always cheered me up, and her presence in my life brought so much fun, comfort, harmony and peace. I also thank so much my Italian parents, Luciano and Maria Rosaria Cassia, for sending their good wishes and warm feelings. Finally, an immeasurable gratitude goes to my sister Eris Erkoca for having me always in her heart as she is in mine, my mother Jale Erkoca for her unconditional love and making my life so much beautiful, and my father Serdar Erkoca for his endless efforts to make us all happy, and for giving me the strength in life. They have always helped me by all means, and they have made me happy and joyful throughout my life. This work would not have been possible without them.

DEDICATION

To My family

TABLE OF CONTENTS

TABLE OF CONTENTS – *Continued*

LIST OF FIGURES

LIST OF FIGURES – *Continued*

LIST OF TABLES

ABSTRACT

Large-scale neutrino telescopes will be powerful tools to observe multitude of mysterious phenomena happening in the Universe. The dark matter puzzle is listed as one of them. In this study, indirect detection of dark matter via neutrino signals is presented. The upward muon, the contained muon and the hadronic shower fluxes are calculated, assuming annihilation/decay of the dark matter in the core of the astrophysical objects and in the Galactic center. Direct neutrino production and secondary neutrino production from the decay of Standard Model particles produced in the annihilation/decay of dark matter are studied. The results are contrasted to the ones previously obtained in the literature, illustrating the importance of properly treating muon propagation and energy loss for the upward muon flux. The dependence of the dark matter signals on the density profile, the dark matter mass and the detector threshold are discussed.

Different dark matter models (gravitino, Kaluza-Klein and leptophilic) which can account for recent observations of some indirect searches are analyzed regarding their detection in the kilometer size neutrino detectors in the near future. Muon and shower rates and the minimum observation times in order to reach 2σ detection significance are evaluated, with the result suggesting that the optimum cone half angles chosen about the Galactic center are about 10° (50°) for the muon (shower) events. A detailed analysis shows that for the annihilating dark matter models such as the leptophilic and Kaluza-Klein models, upward and contained muon as well as showers yield promising signals for dark matter detection in just a few years of observation, whereas for decaying dark matter models, the same observation times can only be reached with showers. The analytical results for the final fluxes are also obtained as well as parametric forms for the muon and shower fluxes for the dark matter models considered in this study.

CHAPTER 1

INTRODUCTION

The dark matter (DM) puzzle, which is still an open question in cosmology, has persisted for more than seven decades [1, 2]. The presence of DM is inferred from gravitational effects on visible matter at astronomical scales. Observations of galactic rotation curves [3], orbital velocities of galaxies within clusters [1], anisotropies of the cosmic microwave background (CMB) [4, 5, 6, 7], distance measurements from Type Ia supernovae (SN) [8, 9], baryon acoustic oscillations (BAO) [10, 11] and large scale structure [12] all imply the existence of cold (non-relativistic) dark matter (CDM) with an abundance of 23% of the total density of the Universe ($\Omega_{CDM} = 0.233 \pm 0.013$). In addition, the combination of the CMB, SN and BAO data predicts that only 4% of the total density of the Universe can be attributed to the baryonic matter ($\Omega_{baryons} = 0.0462 \pm 0.0015$) whose particle content is given by the Standard Model (SM) of particle physics.

The current density of CDM is explained in the context of cold relic scenario. According to that, DM particles are abundant and in thermodynamic equilibrium in the early Universe and then "freeze out" or decouple from the hot plasma due to the Hubble expansion and form the DM today. The freeze-out occurs at the temperature T_f (freeze-out temperature) which typically satisfies $m_\chi/T_f \simeq 20 - 30$ for a DM particle with mass m_χ [13]. It can be shown that the current density of DM is inversely proportional to the annihilation cross section at freeze-out (see, e.g Ref. [14]). The higher the annihilation cross section at the time of freeze-out, the smaller is the current density of DM in the Universe. Thus, the observed density of DM in the Universe today constrains the annihilation cross section in the early Universe, specifically at the time of freeze-out. Considering the results of the above mentioned observations, the thermal average of annihilation cross section times the relative velocity satisfies $\langle \sigma v \rangle = 3 \times 10^{-26}$ cm^3 s^{-1} at the time of freeze-out [13].

On dimensional grounds, a DM particle of mass in the range of 100 GeV to several TeV with weak scale couplings can have annihilation cross sections of that order at freeze-out, providing a natural explanation for the observed density of DM today [15, 16].

An interesting coincidence, independent of the DM issue, is that the TeV scale is the characteristic scale of new physics beyond the SM according to naturalness arguments [17] which imply that above the TeV scale there should be cancellations in the loop-level corrections to the SM Higgs mass. Collider experiments such as the Large Hadron Collider (LHC) at CERN will explore this new scale physics in the near future [18]. The detection and characterization of DM particles is possible in these LHC searches. However, collider searches will not be sufficient to determine the stability of DM particles on cosmological time scales and their current abundance in the Universe [16]. Therefore, apart from the colliders, the two independent but complementary approaches; direct and indirect searches (see e.g, [19]) are necessary in exploring the nature of DM.

Direct searches look for energy deposition via nuclear recoils from DM scattering by using different target nuclei and detection strategies and can provide valuable data on the couplings of DM to the SM particles. On the other hand, indirect DM searches look for DM annihilation (or decay) products, either photons [20, 21, 22, 23, 24, 25, 26] or anomalous cosmic rays, such as positrons and antiprotons [27, 28, 29, 30, 31, 32, 33, 34], or neutrinos [35, 36, 37, 38, 39, 40, 41, 42, 43, 44, 45, 46, 47, 48].

Theoretical studies of the indirect DM detection via neutrino signals have recently received a lot of attention [49, 50, 51, 52], including DM accumulation in the astrophysical objects (the Earth or Sun) [15, 53, 54, 55, 56, 57, 58] and in the Galaxy [59, 60, 61, 62, 63, 64, 65, 66], and subsequent annihilation (or decay) to neutrinos, which are produced at energies of the order of the mass of the DM. These neutrinos with energies, $E_\nu < m_\chi$, propagate without being absorbed or deflected in transit toward the Earth in the free space. However, during their travel, vacuum (and matter) oscillation effects mix the three flavors and the interactions in the astrophysical objects may yield absorption effects. Finally, the ones that reach

the Earth interact on their way to the detector or inside the detector producing observable muon and shower fluxes. Next generation neutrino telescopes will have the capabilities to probe energies, $E_\nu > 100$ GeV [39, 41, 67, 68, 69] and they will be potentially useful to discover DM in the Universe.

In this study, we present a comprehensive picture of the detection of DM signals in the next generation large-scale neutrino telescopes based on our results given in Refs. [70, 71, 72]. We mainly focus on DM signals from Galactic center (GC), and from astrophysical objects (the Sun and the Earth). We consider different signal topologies, such as upward muon and contained muon events, as well as shower events. We study the energy distributions for the muon and shower fluxes and we also calculate the total event rates to be observed in kilometer scale neutrino detectors. We also study the neutrino signals from annihilating and decaying DM particles and the model parameter space for each DM particle to be probed by these large-scale neutrino telescopes in the near future. The organization of the chapters is as follows.

In the second chapter, the evidence that has been collected for the last seven decades implying the presence of DM in the Universe is reviewed. The detection strategies including the direct and indirect searches are presented with the current limits on the DM-nucleon cross sections. In the following section, the DM candidates which were proposed to account for recent observations of several indirect searches are presented. Among the indirect searches, the large-scale neutrino telescopes will play a major role in the quest of DM. Therefore, in the last section of this chapter, the on-going and future large scale neutrino telescopes are described.

The third chapter presents a brief review of neutrino physics, starting with the description of neutrinos in the SM of particle physics. In the following section, neutrino oscillations and the current limits on the oscillation parameters are presented. The evidence for neutrino oscillations indicates that neutrinos are massive and an extension of the SM is required. In addition, the neutrino oscillations mix different neutrino flavors as the neutrinos travel in the free space or in matter and the final fluxes for different neutrino flavors are affected accordingly. The DM signals

in the neutrino telescopes are due to charged leptons produced in neutrino-nucleon interactions and thus depend on the incident neutrino spectra. Therefore, in the following sections, the theoretical framework for neutrino-nucleon scatterings and the neutrino spectra from the decay of SM particles are described.

So far, current neutrino telescopes have been very successful in the detection of the predicted atmospheric neutrino signal. The fourth chapter starts with presenting the most recent data of atmospheric muon neutrino flux from AMANDA-II experiment [73]. In the following sections, the required theoretical tools for calculating the DM signals in the neutrino detectors are presented, including the dependence of the signal on the nature of DM (annihilating or decaying), on the choice of the DM density profile, on the location of neutrino production (Sun, Earth or Galactic center). Possessing quite different topologies in neutrino detectors, contained muon, upward muon and shower events are described separately, and the theoretical framework for calculating energy distributions and total counts for each topology is presented.

Neutrino signals in underground or underwater detectors from DM annihilation in the GC or in the astrophysical objects are the subject of the fifth chapter. The results for the neutrino induced upward and contained muon flux, as well as the neutrino induced muon and shower event rates calculated for different annihilation channels of DM are given. The muon propagation and energy loss in the Earth is taken into account for the upward muon flux calculation [70]. The results are compared with the backgrounds due to atmospheric muon neutrinos and the rates of contained and upward muon events relevant to IceCube and future neutrino detectors like KM3NeT are discussed. The results from this study are also compared with those obtained using other theoretical frameworks widely used in the literature, [53, 57] and the importance of the inclusion of the muon propagation in the rock for the upward muon events is discussed. A brief summary and discussion of the results obtained in this chapter are given in the last section.

In chapter six, results for the neutrino induced contained and upward muon flux, hadronic shower flux and the muon and shower event rates for different DM models are presented. The considered DM models are those which can explain

the results from other indirect DM searches. In that respect, annihilation of the lightest Kaluza-Klein particle [74, 75], annihilation of leptophilic DM particle [76, 77, 78, 79, 80, 81, 82, 83], two-body and three-body decay channels of gravitino [59, 60, 84, 85, 86, 87], as well as the decay of the leptophilic DM [77] are studied. Furthermore, detection significances of the DM signals at IceCube+DeepCore [67, 88, 89] detector are evaluated. The above mentioned DM models are also compared in terms of their energy spectra and the total counts of the muon and shower events. In the last section, a short summary and discussion of the results are presented.

In Appendix A, a brief review of the current cosmological model, ΛCDM is presented. The definitions of some relevant cosmological parameters are given and the thermal cold relic density calculation and the so-called "WIMP Miracle" are reviewed.

The DM signals from the astrophysical objects depend on the details of the interplay between the capture and the annihilation processes taking place in the cores of the astrophysical objects. In Appendix B, the earlier derivation of the capture rates in the astrophysical objects by Gould [90, 91] is reviewed. The effect of different nuclear species on the DM capture rate is analyzed.

CHAPTER 2

DARK MATTER (DM)

In cosmology, dark matter (DM) has been a very exciting and popular research area for the last 70 years and is hypothesized to explain the discrepancy between the mass of galaxies, clusters of galaxies measured via dynamical and gravitational effects and the mass inferred from the visible "luminous" matter. Its existence was first revealed by Fritz Zwicky in 1930 during his study of the Coma cluster [1, 2]. If the DM is a thermal relic, its abundance depends on two parameters; its mass and the annihilation cross section (see Appendix A). Depending on the mass, DM can be relativistic (Hot Dark Matter,HDM), non-relativistic (Cold Dark Matter,CDM) or can have an intermediate mass (Warm Dark Matter, WDM) which shares the properties of both HDM and CDM. Among the particles in the SM of particle physics, only neutrinos can be part of DM as HDM. However, they can only form 2% of the DM. Thus, potentially the DM particles are expected to have either warm (sterile neutrinos, light gravitinos, non thermal neutralinos, etc.) or CDM (e.g weakly interacting massive particles; WIMPs) properties. In this study, we will mostly concentrate on the neutrino signals from the neutralino, lightest Kaluza-Klein particle, leptophilic particle and gravitino DM particles.

In the standard CDM model (SCDM), the DM relic density is given by Eq. (A.38). In this model, DM particles are assumed to be massive and interact very weakly with the ordinary matter. The most important motivation to consider such a model actually lies in the growth of the cosmological perturbations. According to the model, the presence of DM can develop potential wells before the matter-radiation equality since it is decoupled from the radiation earlier and thus causes the observed contrast in density today. SCDM can be extended to ΛCDM model where the Universe is dominated by the dark energy and most of the matter content is not known. This model is very successful in the sense that (1) the observations of

large-scale structure are in agreement with its predictions, (2) high-energy physics proposes many candidates and (3) if the DM particles interact via weak interactions, then they have the correct relic density suggested by the thermal cold relic scenario (see, Eq. (A.38) and following arguments). So far, some N-body numerical computations which simulate the structure formations in the Universe have suggested the DM density profiles to be in the form [92]

$$\rho(r) = \frac{\rho_s}{(r/r_s)^{\gamma}[1+(r/r_s)^{\alpha}]^{(\beta-\gamma)/\alpha}} \tag{2.1}$$

where the parameters for different density profiles are presented in the Table (2.1). Several different groups have obtained different results for the spectral shapes especially in the innermost regions of galaxies and galaxy clusters, i.e the precise value of the power-law index γ is still under debate. However, Klypin, Zhao and Somerville [93] found a good agreement between NFW profiles and observational data due to microlensing events for our galaxy and M31 whereas considering DM models in which DM annihilates into charged leptons, the current data from indirect detection experiments (i.e observed positron excess) can better be explained by DM density profiles with $\gamma = 0$ (core models) [34].

Table 2.1: Typical values for the parameters in Eq. (2.1) for different DM density profiles.

Model	α	β	γ	r_s (kpc)
Navarro-Frenk-White (NFW) [92]	1	3	1	20
Moore [94]	1.5	3	1.5	28
Kravstov [95]	2	3	0.4	10
Isothermal with core radius [96]	2	2	0	3.5

The characteristic density ρ_s can be determined from the total mass and the size of the galaxy. In Fig. 2.1, different DM density profiles are compared in terms of the dependence of the linear density ($r^2\rho(r)$) on the distance from the GC (r) [1].

[1] In our calculations, we fix ρ_s for a given density profile by requiring ρ(r=8.5 kpc)=0.3 GeV/cm^3 which gives an estimated value for the DM density in our Solar System [96, 97].

Compared to isothermal (dotted line) and Kravstov (dashed line) profiles, Moore (dot-dashed line) and NFW (solid line) profiles exhibit cuspier halo structures.

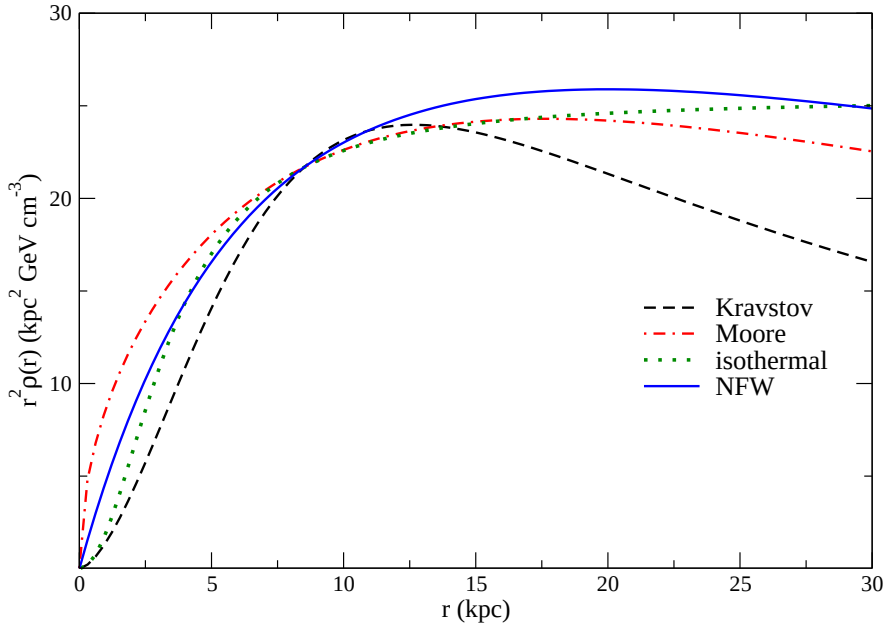

Figure 2.1: Linear density $r^2\rho(r)$ as a function of the distance from the Galactic center (r) for Kravstov (dashed line), Moore (dot-dashed line), isothermal (dotted line) and NFW (solid line) density profiles.

According to several independent observations that we will discuss later in this chapter, DM is assumed to be cold non-baryonic matter which accounts for 23% of the density of the Universe, about five times more than the ordinary baryonic matter which accounts for only 4%. It does not interact with the ordinary matter via electromagnetic forces, and it does not take part in the production of the elements in the early Universe. Its presence can mostly be observed through its gravitational attraction unless it undergoes annihilation processes with its anti-particle or decays and produces observable by-products (photons, neutrinos, etc.).

In the following sections, we discuss some signatures of DM in the Universe, direct and indirect detection techniques.

2.1 Dark Matter Signatures in the Universe

2.1.1 Dark Matter in Galaxies

One of the best evidences for the presence of DM comes from the rotation curves of the stars in the spiral galaxies. Spiral galaxies have flat disks in which stars follow circular orbits and the rotation curves depict the orbital velocities of these stars as a function of the distance from the center of the galaxy. The orbital velocities $v(r)$ can be calculated by using the Keplerian law

$$G_N M_{dyn}(r) = r v^2(r) \tag{2.2}$$

where $M_{dyn}(r)$ is the dynamical mass contained inside the orbit. The surface brightness of the spiral galaxies exhibit an exponential decrease with the distance measured from the GC. So, if there were no non-luminous matter, the dynamical mass of a spiral galaxy would reach an asymptotic value beyond the optical disk (with radius R_d) and the orbital velocities approach zero at far distances;

$$M_{dyn}(r) \to \text{constant}, \quad v(r) \propto \frac{1}{\sqrt{r}} \quad \text{if} \quad r \leq R_d. \tag{2.3}$$

The rotation curve measurements for different spiral galaxies, however, show a very different behavior. The orbital velocities tend towards a non-vanishing value v_∞. This indicates the existence of a non-luminous matter with density profile in the form

$$\rho \propto \frac{1}{r^2} \tag{2.4}$$

at large distances from the center.

2.1.2 Dark Matter in Galaxy Clusters

Galaxy clusters are structures which contain from hundred to several thousands of galaxies. The mass of a cluster can be determined via the application of the virial theorem and/or studying the profile of X-ray emission of the hot radiation from the intracluster gas. Then, the mass of the galaxy cluster can be inferred independent

of the total emitted radiation. High mass to luminosity ratios relative to that of the Sun as a measure give evidence for DM in the galaxy clusters.

The first hint of DM in the Universe was obtained by Zwicky during his study of Coma cluster in 1930 [1]. He inferred that mass to luminosity ratio of the cluster was about two orders of magnitude larger than the mass to luminosity ratio of the Sun. In addition to the dynamical properties, another means of measuring DM is via the gravitational lensing, a general relativistic effect which causes the light coming from a distant source (such as a quasar) to bend near a massive object (such as a cluster of galaxies). Strong distortion of the trajectories of the light from far galaxies as they pass through a gravitational lens has been observed and by measuring the geometry of the distortion the mass of the cluster that causes the distortion was obtained. In almost all cases, the mass to light ratios agree well with the dynamical DM measurements of the clusters. Unfortunately, it is not always possible to detect significant distortion in the image of a single background source due to a massive foreground object. However, even in these cases, a statistical measurement technique called the weak lensing can be used to detect minute distortions [98]. It includes the systematic alignment of background sources around the lensing object so that the mass of the lensing object can be determined. Using this method, so far in several searches the mean distribution of DM has been characterized which shows a strong correlation with the DM densities predicted by the other large scale structure measurements.

It was shown in Ref. [99] that the combination of all the above mentioned studies indicate that about 80% of the matter is composed of DM and the density profiles can be described by NFW profiles.

2.1.3 Dark Matter Signatures in CMB Radiation

The cosmic background radiation (CMBR) is a relic radiation from the early Universe which was about 400,000 years after the Big-Bang. The CMBR was emitted after the recombination epoch when the neutral atoms were formed and the Universe became transparent to photons. The photon temperature was about 3000 K

at the time of recombination, however, it has redshifted due to the expansion of the Universe over the last 13 billion years. Today it is observed as a blackbody radiation peaked at $T = 2.726$ K which corresponds to a microwave frequency of 160.2 GHz. After the discovery and the confirmation of CMBR in 1964 [100], NASA Cosmic Background Explorer (COBE) [101, 102] made further searches and observed for the first time the fluctuations (anisotropies) in CMBR which was later detected by BOOMERANG [103], Degree Angular Scale Interferometer (DASI) [104] and the Cosmic Background Imager (CBI) [105] experiments. So far, the most detailed measurements have been done by the COBE's successor, the Wilkinson Microwave Anisotropy Probe (WMAP) [5]. WMAP's measurements support the ΛCDM model according to which the Universe is flat, dominated by dark energy and has a considerable amount of DM which constitutes about 30% of the density of the Universe. The anisotropies in CMBR are at a level of about one part in 10^5 and can be explained as the acoustic oscillations in the photon-baryon plasma which took place before the recombination. The matter can be attracted towards the small overdense regions in the primordial plasma and the heat produced by photon-baryon interactions creates a large amount of outward pressure. DM interacts weakly with matter and mostly populate the central regions of the overdense regions. The strongly coupled photon-baryon plasma, while moving away from the center of perturbation, is pulled back by the gravity and oscillations take place. Until recombination, photons and baryons move outward together and after photons decouple from baryons they diffuse away, leaving a shell of baryons at a fixed radius called the sound horizon and the DM at the center of the perturbation (see Ref. [98] for a review). The acoustic oscillations are supposed to leave their imprint in the visible matter by Baryon Acoustic Oscillation (BAO) [10] clustering which refers to an overdensity or clustering of baryonic matter at certain length scales (~ 150 Mpc) related to sound horizon due to acoustic waves propagated in the early Universe. BAO were studied by the Sloan Digital Sky Survey (SDSS) [12] by observing more than 200,000 galaxies. SDSS detected BAO length scales of the order of ~ 150 Mpc which are consistent with the WMAP results.

In short, according to the observations ranging from the galactic scale to cosmological scale, a form of "non-luminous" matter which only interacts gravitationally must prevail in the Universe (see, e.g [98] for a review). Current data from WMAP imply that DM is five times more abundant than the ordinary matter in the Universe [10, 11]. The best fit values for the density parameters (see Appendix A) from WMAP data combined with BAO and SN measurements read [10, 11]

$$\begin{aligned} \Omega_\chi h^2 &\simeq 0.1131 \mp 0.0034 \\ \Omega_\mathrm{b} h^2 &\simeq 0.02267 \mp 0.0006 \\ \Omega_\Lambda &\simeq 0.726 \mp 0.015. \end{aligned} \tag{2.5}$$

2.2 Dark Matter Detection Strategies

As mentioned in the previous section, there is plenty of evidence that can safely make one believe in the existence of the DM in the Universe. However, its detection is still an issue. Several independent experiments have been running over the years to "see" this mysterious matter that is supposed to reside in the Universe. These experiments can be grouped into two independent but complementary classes : direct and indirect detection experiments.

2.2.1 Direct Detection Searches

If the galaxy is composed of DM particles, they should pass through the Earth and interact with the matter. In direct detection searches, the signatures of these interaction are looked for. In that respect, these searches can provide valuable data on the DM's couplings to the SM. In principle, they all look for energy deposition via nuclear recoils from DM scattering by using different target nuclei and detection strategies, and expect to observe the same DM mass and cross sections. Most of the direct detection experiments can detect recoil energies of the order of $\sim$ 1-10 keV [106].

There are vast number of direct detection experiments in operation or in construction. We can classify them according to the detection strategies that they use [19]. In general, they all tend to measure the effects due to the recoil of DM and a target nucleus. The observed signals are in the form of phonons (heat), ionization or scintillation. There are those which measure only scintillation (DAMA, NAIAD, KIMS, DEAP/CLEAN), only phonons (CRESST-I,CUORE), ionization and phonons (CDMS,EDELWEISS,EURECA), ionization and scintillation (ZEPLIN,XENON,WARP,LUX), scintillation and phonons (CRESST-II).

The DM signal rates at the detectors depend mainly on the DM density and the velocity distributions in the solar neighborhood and the DM-nucleon cross sections. The DM particles can scatter off of nuclei either via spin dependent or spin independent (scalar) interactions. The cross sections for the spin dependent scattering are proportional to the spin content of the nucleon that arises in general due to axial-vector interactions between DM and the quarks in the nucleons. Thus, very little or nothing is gained by using heavier target nuclei. However, for the scalar interactions the cross section increases considerably with the mass of the target nuclei, typically for DM heavier than the target nuclei, the scalar cross sections can scale as N^4 [53, 106] where N is the number of nucleons in the target nucleus.

Currently, the strongest upper bounds on the spin-independent ($\sim 10^{-7}$pb) and spin-dependent ($\sim 10^{-2}$pb) DM-nucleon cross section of a DM particle with mass ~ 100 GeV come from the XENON Dark Matter Search (XENON) [107] and the Cryogenic Dark Matter Search (CDMS) [108, 109] experiments. Recently, CDMS-II have observed two events in the signal region and put tighter constraints on DM-nucleon spin-independent cross sections ($\sim 4 \times 10^{-8}$pb) for DM particle with mass ~ 100 GeV [109].

Among the direct DM searches, the very first positive signal was reported by the DArk MAtter (DAMA) collaboration after the detection of an annual modulation (expected to be due to the motion of the Earth around the Sun) in the 13 years of combined data of the DAMA/NaI and DAMA/Libra experiments [110]. The compatibility of the DAMA results with those of all other searches which have

reported null results has been studied in the literature (see, e.g [111] for a review). One possible explanation to this is given in the context of inelastically scattering DM (IDM) models where the DM particle, χ, with mass m_χ is postulated to have an excited state, χ^* with mass difference $\delta = m^*_\chi - m_\chi \simeq 100$keV and where the inelastic scattering with a nucleon N, $\chi + N \rightarrow \chi^* + N$ is more dominant than the elastic scattering. For elastic collisions, in order to provide a particular recoil energy E_R, the DM is required to have a minimum velocity of $v^{el}_{min} = \sqrt{m_N E_R/2\mu^2}$ where μ is the reduced mass of the DM-nucleus system. However, the minimum DM velocity required for an inelastic collision is somewhat higher, i.e $v^{inel}_{min} = v^{el}_{min} + \delta/\sqrt{2m_N E_R}$. Therefore, for IDM models, only-high velocity DM particles can be excited, low E_R events can not be seen and since v^{inel}_{min} decreases with increasing target mass, m_N, targets with high mass are favored as is the case for the DAMA experiments. For IDM models with spin independent interactions, the current CDMS results constrain the DAMA results significantly, however, for several other versions of the IDM where the DM has spin dependent couplings, DAMA results are compatible with all other experimental bounds [111].

Other than IDM, the DAMA results can also be explained by a light elastically scattering DM. For those scenarios, the DAMA results favor DM with mass $\sim 5-10$ GeV both for spin dependent and spin independent interactions [19]. Recently, CoGeNT collaboration has also observed an excess of events which is compatible with DM particles with spin independent interaction with mass $\sim$10 GeV. In the near future, these possible DM signals will be better understood by CoGeNT, CDMS and XENON100 experiments.

2.2.2 Indirect Detection Searches

Indirect searches mostly rely on the detection of photons, electrons, positrons and neutrinos from the DM annihilations ($\chi\chi \rightarrow \cdots$) or decays ($\chi \rightarrow \cdots$). In the CDM scenarios, since the DM is considered to be non-relativistic the signals are expected to have a cutoff at an energy of the order of DM mass (m_χ). The final state particles can be monoenergetic due to the direct production channel (for example, $\chi\chi \rightarrow \gamma\gamma$)

or can have an energy distribution due to the secondary productions.

The very first indirect detection makes use of the gamma-ray astronomy which is conducted by both ground based and space based telescopes. There are four large ground based Atmospheric Cherenkov Telescopes (ACTs): HESS [25], MAGIC [112], VERITAS [113] and CANGAROO-III [114] which can detect photons with energies in between 20 GeV and several TeV (see, e.g [19] and references therein). In addition to ACTs, the space based Large Area Telescope (LAT) which is the main instrument on Fermi Gamma-ray Space Telescope (FGST) [20] also detects γ rays in the 20 MeV to 300 GeV energy range with a much better sensitivity than its predecessor Energetic Gamma Ray Experiment Telescope (EGRET) [115]. FGST was launched on June 11, 2008 and has been collecting data since then. It also detects electron and positron fluxes and is expected to discover subhalos and test the signals from other indirect searches.

Other than the photons, antimatter (positrons, antiprotons, etc.) is an interesting potential discovery signal of DM due to lack of antimatter in the Universe. Thus, the detection of an excess in positron and antiproton flux with a unique spectrum presenting a cutoff with respect to the approximated power-law spectrum expected from astrophysical sources would lead to the discovery of the DM. Space based Payload of Antimatter Matter Exploration and Light-nuclei Astrophysics (PAMELA) [116], Advanced Thin Ionization Calorimeter (ATIC) [117] and balloon born Polar Patrol Balloon and Balloon borne Electron Telescope with Scintillation fibers (PPB-BETS) [31] and High Energy Antimatter Telescope (HEAT) [29] telescopes have been exploring these excesses.

For some years, observations of an excess in the positron fraction $e^+/(e^+ + e^-)$ by HEAT, a bright 511 keV gamma-ray line from the GC by the European Space Agency (ESA) satellite INTEGRAL [22] and a possible unaccounted-for component of the foreground of WMAP around the GC, the "WMAP Haze" [23], have been considered as possible hints of DM annihilations. Furthermore, there has also been a great interest in the high energy ($\sim$ 200 GeV - 10 TeV) gamma ray signal observed by HESS telescope within a cone half angle of 0.1° about the GC [24] and some

possible DM explanations have been proposed to account for that signal [74, 77].

More recently, PAMELA reported an excess in the positron fraction in the energy range of 10-100 GeV with respect to what is expected from cosmic ray secondaries, which confirmed the HEAT excess. Also ATIC and PPB-BETS observed a bump in the e^++e^- flux from 200 to 800 GeV, but this was not confirmed by the air Cherenkov telescope HESS [32] nor by the FGST. FGST found a slight excess in the e^++e^- flux between 200 GeV and 1 TeV [33]. The positron excess observed by PAMELA may be explained by the presence of particular astrophysical sources [77, 118, 119, 120, 121, 122], or by the annihilation [76, 123] or decay [84] of DM particles. If the observed anomalies in the PAMELA and FERMI data are due to DM annihilation, a larger annihilation rate than expected for typical thermal relics must be assumed. This enhancement may happen due to either large inhomogeneities in the DM distribution near Earth (subhaloes) [54, 124] and/or a larger annihilation cross section of the DM particles. This last possibility may happen if the DM particles are not thermal relics in which case annihilation cross sections can take large values without changing the present DM density in the Universe [19, 123], or if there is an enhancement of the annihilation cross section only at very low velocities [30, 125, 126, 127, 128], which would not affect the annihilation in the early Universe and thus would not conflict with the cold relic scenario.

The low velocity enhancement is often called the Sommerfeld enhancement, which is an elementary effect in nonrelativistic quantum mechanics (see Ref. [126] for a review). A typical example is a DM particle with mass m_χ interacting with a light force carrier ϕ with fine structure constant α_X. In the low velocity limit, the annihilation of DM particles via the exchange of ϕ can be characterized by an attractive Yukawa type potential. The range of the force is determined by the inverse mass of the force carrier, m_ϕ^{-1}. For massless ϕ, the annihilation cross section is enhanced by the Sommerfeld enhancement factor

$$S = \frac{\pi\alpha_X/v_{rel}}{1 - e^{-\pi\alpha_X/v_{rel}}} \tag{2.6}$$

which reduces to

$$S = \frac{\pi \alpha_X}{v_{rel}} \tag{2.7}$$

in the low velocity limit, i.e $v_{rel} \ll 1$. However, for massive ϕ the Sommerfeld enhancement saturates at a value $\sim \alpha_X m_\chi / m_\phi$ due to the finite range of the Yukawa potential. At the time of freeze-out in the early Universe, $v_{rel} \sim 0.3$ and taking ϕ to be massless is a reasonable assumption. Then, Eq. (2.6) gives $S \approx 1 + \pi \alpha_X / 2 v_{rel}$ which ensures that at the time of freeze out there was no enhancement for the annihilation cross section which would alter the thermal relic density observed today. In the present Universe, however, $v_{rel} \sim 10^{-3}$ and Sommerfeld enhancement can be effective and lead to an increase in the annihilation cross section of DM above the value at the time of freeze-out ($\sim 3 \times 10^{26} cm^3/s$) which is required for a thermal relic. Whatever its origin may be, the needed enhancement to explain the data is quantified by a "boost factor", B, ranging from 10 to 10^4 [47, 65, 66, 129, 130].

Besides the positron excess, PAMELA Collaboration has also reported the non-observation of any anomaly in the antiproton flux [131] which also puts an additional constraint on the proposed DM models. Indirect searches for DM annihilations via neutrinos with experiments such as AMANDA (Antarctic Muon And Neutrino Detector Array) [132] and IceCUBE [133, 134] also constrain DM models. The cubic kilometer size neutrino telescope (KM3NeT), planned to be built at the bottom of the Mediterranean Sea [41], will provide additional constraints. With its different view of the sky, in particular for the neutrino signals from the GC, it will be complementary to IceCUBE. In the following section, we will describe some DM candidates that can account for the signals observed by the indirect searches described here and after this section we will present a brief description of the past, present and the future developments in the the large-scale neutrino detectors that are relevant to DM search.

2.3 Dark Matter Candidates (neutralino, gravitino $\psi_{3/2}$, Kaluza-Klein)

The problems that can not be answered in the context of SM motivate physics beyond the SM. These problems can be grouped into two [14]. The first group consists of the experimental data which can not be explained by the SM predictions (DM, neutrino masses, etc.). The second group is composed of experimental data that can be explained by SM, but only after some fine-tuning of the parameters in the model (gauge hierarchy problem, strong CP problem, new physics flavor problem, etc.). Among the second class, the gauge hierarchy problem is the leading motivation for DM candidates, such as WIMPs (weakly interacting massive particles). In SM, the loop-level corrections to the Higgs boson mass introduce large corrections which is proportional to the Planck mass which is about sixteen orders of magnitude larger than the weak scale mass ($m_{weak} \sim 1$ TeV). The question of why these two mass scales are very different than each other is still an unresolved issue (see, e.g Ref. [135] for a review). However, from the theoretical point of view, the problem is most elegantly solved in supersymmetry by introducing new particles with weak scale masses.

In supersymmetry, every SM particle has a super-partner which has the same quantum numbers and gauge interactions, but differs in spin by 1/2. In the loop-level calculations, the new spin-statistics from the supersymmetry part introduces similar corrections to the Higgs boson mass as the ones from SM part but with opposite sign. Therefore, doubling SM particle spectrum stabilizes the gauge hierarchy problem. In addition, this introduces a list of neutral particles as possible DM candidates which contains spin 3/2 fermion (gravitino), spin 1/2 fermions (neutralinos) and spin 0 scalars (sneutrinos). Having large annihilation and scattering cross sections, the sneutrinos are not considered to be good DM candidates since they would be under-abundant and also excluded by the direct detection experiments for all masses up to weak scale. On the other hand, the lightest neutral spin 1/2 neutralino can be a DM with the correct relic density, only for certain values of parameters constrained by cosmology [14].

In addition to the neutralino, the gravitino, the supersymmetric counterpart of the graviton, is also an excellent candidate for the cold DM in the Universe. Assigning gravitino to be the lightest supersymmetric particle (LSP), however, causes some severe problems due to the late decay of the next-to-lightest supersymmetric particle (NLSP). In supersymmetric models, gravitino DM interacts only gravitationally and its interactions are suppressed by the Planck scale. Due to a discrete symmetry called R-parity invoked in order to prevent the proton decay, NLSP can only decay into gravitinos and SM particles with a small decay rate. As a result, NLSP becomes long lived and present in the Universe at the time of Bing Bang nucleosynthesis. If the NLSP is a neutralino, it can decay into hadrons, leading to the dissociation of the primordial elements [136], or if the NLSP is a stau, the formation of a bound state with ^{4}He enhances the production of ^{6}Li by a factor of 300-600 [137], which is in strong conflict with observations [138].

One possible solution to this problem is given by allowing a small breaking of R-parity without violating any experimental bounds. With the presence of R-parity violation, the neutralino LSP becomes too-short lived to be considered as a DM, however, the gravitino LSP can still have sufficiently long life time (10^{23}-10^{27}s) which is typically orders of magnitude larger than the age of the Universe ($\sim 10^{17}$s) [85] and NLSP decays into SM particles via R-parity violating interactions before the onset of the primordial nucleosynthesis.

Even though it is long lived, the gravitino after R-parity breaking is no longer invisible and can decay into SM particles, yet at a very slow rate. For instance, the gravitino DM with mass of a few 100 GeV and lifetime $\sim 10^{26}$s can explain anomalous excesses in the positron fraction data [84, 86]. If the gravitino is lighter than the $W^{\mp}$ bosons, it decays mainly into a photon and a neutrino, whereas if it is heavier than the gauge boson masses, new decay modes arise. The gravitino can decay into a $W^{\mp}$ boson and a charged lepton, or into a Z boson and a neutrino. The branching fractions for all these channels are determined by the size of the R-parity breaking mixing parameters and can be found in the literature [85, 86]. In addition to the two-body decay channels, the gravitino ($\psi_{3/2}$) has also three-body

decay channels. The three-body decay channel of gravitino, $\psi_{3/2} \rightarrow l^+ l^- \nu$, where the gravitino decay into leptons (l) and neutrino (ν) is well motivated due to the fact that it can be a viable explanation for the positron excess observed by PAMELA as mentioned before. For certain values of the parameters the three-body decay can dominate over the two-body decay and the gauge boson production, which may yield overproduction of antiprotons, can be suppressed [87]. Thus, the gravitino can possess a pure leptophilic nature (i.e the DM annihilation/decay products are only leptons). Some other leptophilic DM models in which DM annihilates or decays only into charged leptons are also well studied in the literature [76, 77], with an aim to explain the observed anomalous positron excess.

An interesting alternative for the new-scale physics is the models with extra dimensions. One such a model is the Universal Extra Dimensions (UED) in which all particles propagate in flat, compact extra dimensions of size 10^{-18} m or smaller [139]. In contrast to supersymmetry, UED models do not solve the gauge hierarchy problem and are assumed to be a low-energy approximation of a more complete theory [14]. In minimal UED, there is one extra dimension of size R compactified on a circle and every SM particle has infinite number of partners which obey the same spin statistics. At a given Kaluza-Klein (KK) level n, the partner particle mass is $\sim nR^{-1}$ [42, 75]. The discrete parity known as KK-parity assures the stability of the lightest KK particle (LKP), rendering it a viable DM candidate. In general, the LKP is considered to be the first KK excitation of the hypercharge gauge boson which is denoted as $B^{(1)}$ [140]. This LKP couples to all fermions (and the Higgs) proportionally to their hypercharges with coupling g_1, and is approximately decoupled from the gauge bosons when the effects of electroweak symmetry breaking are negligible [75]. Taking g_1 to be close to weak scale coupling, the annihilation cross section of $B^{(1)}$ turns out to be $\sigma \sim$ O(pb) for the mass of LKP of the order of TeV [75]. The cold relic density criteria imposes that the $B^{(1)}$ mass must lie in the range 600 GeV $\leq m \leq$ 1.4 TeV [14].

2.4 Large Scale Neutrino Telescopes

The very first neutrino searches were conducted in 1960s in two deep mines; one in India and the other in South Africa where both experiments used scintillation detectors (see, e.g Ref. [134] for a review). In addition to the detection of atmospheric neutrinos by these two experiments, by 1967 Davis' geochemical experiment also detected solar neutrinos [141]. In the following decade, the scintillation detectors evolved and by the late 1980s, Monopole, Astrophysics and Cosmic Ray Observatory (MACRO) had observed over 1000 neutrinos over a period of six years [142]. In the meantime, the Frejus experiment measured the atmospheric muon neutrino spectrum and set an upper limit on extraterrestrial neutrinos up to TeV energies [143]. Later on the researchers started to use a new technique for detecting neutrinos, which was first suggested by Markov in 1960 [144]. The technique relies on the charged particle detection via the observation of Cherenkov radiation emitted in the water or ice (see, e.g [134]). The first-generation of neutrino detectors which followed this new strategy were Irvine-Michigan-Brookhaven (IMB) [145] and Kamiokande [146] detectors where both of them used kilo-tons of purified water tanks monitored by thousands of photomultiplier tubes (PMTs) which are optimized to GeV energies. In addition to collecting data which led to the "solar neutrino puzzle", IMB and Kamiokande also detected some neutrinos in the MeV range from supernova 1987A. Then, the second-generation 50000 ton Super-Kamiokande [147], which is a scaled-up version of Kamiokande, and 1000 ton heavy-water (D_2O)-based Sudbury Neutrino Observatory (SNO) [148] detectors confirmed the neutrino oscillations in both solar and atmospheric neutrinos. This was the first evidence which showed that neutrinos are massive in conflict with the SM of particle physics.

In the search of cosmic neutrinos whose spectra extend to energies where the atmospheric neutrino flux becomes negligible, the neutrino detectors are required to have larger (kilometer-scale) volumes. The detection of these high energy neutrinos has a considerable impact on understanding the most violent processes in the Universe, such as jets originated from AGNs or Gamma Ray Bursts (GRBs),

interaction of ultra-high energy cosmic rays with the cosmic microwave background photons, etc. In addition, the observations of high energy neutrinos will also help in exploring the properties of DM in the Universe. To detect these high energy neutrinos, large scale neutrino telescopes have been being built in deep seas or in lakes or in ice. In these detectors, the neutrinos with energies ~ 10 GeV and above can be detected by observing the Cherenkov radiation from the charged leptons (muons and electrons) resulted in neutrino-nucleon interactions in or near the detector. The Cherenkov light is detected by PMTs embedded in transparent pressure spheres which, in most designs, are attached to vertical strings. In general, the spheres are 10-20 meters apart along a string and the spacing between the strings is about 30-100 meters which allows large volumes to be covered. However, large spacing between the PMTs make it difficult for the detector to be sensitive to the phenomena below 10-100 GeV [149].

In the search for cosmic neutrinos, atmospheric muons and atmospheric neutrinos yield significant background signals that need to be reduced or if possible eliminated. Therefore, neutrino telescopes mainly look for neutrinos coming from the other hemisphere, using the Earth as a shield against the atmospheric muons. However, atmospheric neutrinos which are produced in the interaction of the cosmic rays introduce an irreducible background. In that respect, the energy distribution of observed neutrinos plays a crucial role since the neutrino spectra from cosmic sources or DM are expected to be harder than the atmospheric one [132]. The PMTs, which record the arrival time of the Cherenkov light with an accuracy of a few nanoseconds, can also measure the amplitude of the Cherenkov light and the neutrino energy can be estimated from the amount of light detected in these optical sensors. In addition, the pattern of Cherenkov light can be used to identify the flavor of the incident neutrino. Muon (electron) neutrinos produce muons (electrons) via charged current (CC) interactions. In the detector, a muon travels in an almost straight line and loses energy by ionization whereas an electron produces an electromagnetic shower by going through multiple scatterings. Thus, muons produce track-like events and electrons produce cascades. For track-like events, the effec-

tive volume for detection exceeds the actual detector volume, however, the effective volume for cascade detection is close to the geometrical volume of the detector.

In the search of point-like neutrino sources, having a good angular resolution is also crucial. Compared to telescopes in the ice, water based telescopes, in general, have better angular resolutions due to lack of dust and/or bubbles which can make light to scatter as is the case in the ice. On the other hand, the drawbacks of the water based telescopes are the additional light produced by beta decay of ^{40}K salt that exists in the sea water, bioluminescent light from biological organisms and the instability of the deep-sea currents [150]. In the following section, the deep-sea and the ice-based detectors will be introduced.

2.4.1 Deep-Sea Neutrino Telescopes

The very first effort to transform large volumes of natural water into a neutrino telescope was made by the Deep Underwater Muon and Neutrino Detector (DUMAND) collaboration [151]. The plan was to build a deep-ocean detector in the sea off the main island of Hawaii, however, the project was in 1995 after a pressure vessel leaked during the first string deployment [134]. The first atmospheric neutrinos underwater were detected by the BAIKAL collaboration which was the first to deploy three strings at a depth of 1100 m in the Siberian Lake Baikal [152].

The first neutrino telescope project in the Mediterranean Sea was the Neutrino Extended Submarine Telescope with Oceanographic Research (NESTOR) that started in 1989 [153]. The telescope has a tower-like structure residing at the deepest part of the Mediterranean Sea (in the Ionian Sea at a depth of about 4000 m). The completed tower consists of 12 floors and 144 Optical Modules (OMs) and a height of 220 m. The OMs are in pairs of one upward and one downward looking OMs. In March 2003, a fully equipped prototype with 12 OMs was deployed and more than 5 million events were recorded. The zenith distribution of atmospheric muons was made.

In addition to NESTOR, since 1998 the Neutrino Mediterranean Observatory (NEMO) collaboration has also made a considerable progress in developing and

validating key technologies for a deep-sea cubic-kilometer scale neutrino telescope [154]. The basic design of the NEMO detector is composed of 16 storeys each of which hosts 4 OMs. Similar to NESTOR, half of the OMs look vertically downwards and the other half look upwards. During the period between 2002 and 2006 (The NEMO Phase-I) the Collaboration collected data for the down-going atmospheric muons and also obtained angular distributions by using a fully equipped underwater test detector deployed at the depth of 2100 m undersea 25 km off-shore Catania port. The agreement between the data and the Monte Carlo simulations were also reported. As a continuation of the first phase, in the NEMO Phase-II a 16 storey tower will be deployed in the harbour area of Portopalo di Capo Passero with a goal of finalizing the validation of the deployment and connection techniques and the efficiency of the detector at the depth of 3500 m.

Among all the other deep sea neutrino telescopes, Astronomy with a Neutrino Telescope and Abyss Environmental Research (ANTARES) telescope is currently the most sensitive one located 40 km off Toulon in the French coast at a depth of 2500 meters [155, 156]. It consists of 12 450-meter-long lines each of which has 25 floors separated by 14.5 meters vertically. Each floor contains three optical modules separated by 120° from each other on a horizontal plane and looking 45° vertically downwards to optimize the detection of Cherenkov photons from upgoing tracks. The detector construction was completed in 2008. ANTARES is designed for the detection of all three neutrino flavors coming from either Galactic or extra-Galactic sources. In addition, it is also sensitive to the detection of neutrinos produced in the cores of the astrophysical objects (Sun or Earth) via DM annihilation. The total sky coverage of ANTARES is close to 3.5πsr which exhibits an overlap of about 0.5πsr with that of the IceCUBE experiment at the South Pole. Thus, both detectors provide complete coverage of the high-energy neutrino sky.

With an aim to unify the three pilot projects (ANTARES, NEMO, NESTOR), a kilometer-cube neutrino telescope, KM3NeT is planned to be built as a future research infrastructure in the Mediterranean Sea [155, 157]. KM3Net will be operating to detect neutrinos from distant astrophysical sources which consist of supernovae,

colliding stars, gamma ray bursters and will be a very powerful tool in the quest of DM. For the muon events, its projected angular resolution is as low as 0.1° for neutrino energies above 10 TeV [155]. It will be sensitive to all neutrino flavors and have an energy threshold of a few 100 GeV. Due to its location in Northern Hemisphere, it will be complementary to IceCUBE operating at the South Pole, for example in the searches of neutrino signals from the GC.

2.4.2 Ice-based Neutrino Telescopes

In addition to the water based detectors, the neutrino detectors which are built in the ice play also an important role in detecting high energy neutrinos over the atmospheric neutrino background. For instance, the Antarctic Muon And Neutrino Detector Array (AMANDA) [39] which was constructed between 1996 and 2000 at the South Pole uses the polar ice as a medium to detect charged leptons via Cherenkov light. It consists of 677 PMTs attached to 19 strings at depths of 1500-2000 m. The average angular resolution reached by AMANDA detector for track-like events is about 2°. For the present AMANDA-II detector, the muon effective area is about 10^4 m^2 for 1 TeV muons.

The kilometer scale IceCube detector (see Fig. 2.2), the successor of AMANDA, is still under construction at the South Pole [134]. The complete detector will consist of 86 kilometer-size strings that contain a total of 5160 digital optical modules (DOMs) whose separation is 17 m along each string. IceCube will make use of a volume of about 1 km^3 of clear ice at the depths of 1450-2450 m. Altough it will detect neutrinos with energies in excess of 100 GeV, the sub-detector called Deep Core which will be making up the bottom half of the IceCube detector will decrease the threshold to $\sim$ 10 GeV with the help of closely spaced ($\sim$ 7 m) high quantum-efficiency DOMs [40]. Deep Core consists of an infill of 6 strings with 60 DOMs. The outer DOMs in IceCube and 10 DOMs in the top portion of Deep Core will be used to veto events originating outside the central detector. This design, in effect, will greatly reduce the atmospheric muon background in the analysis of downward-going muons.

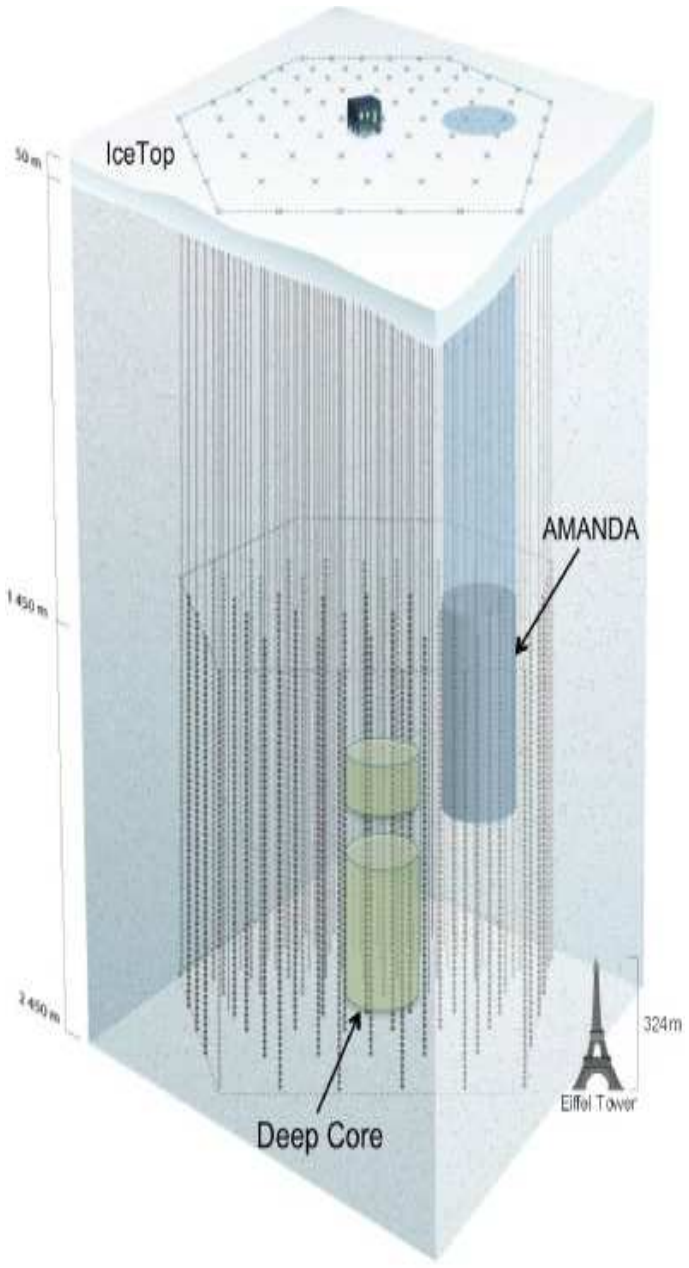

Figure 2.2: From [40]. The IceCube detector, consisting of AMANDA and DeepCore detectors

In addition, IceCube also includes a surface air shower array (IceTop) to detect cosmic-ray air showers, with a threshold of 300 TeV. The array consists of 160 ice-filled tanks each of which hosts two IceCube DOMs.

So far, AMANDA and IceCube 22-string data sets have not found any significant deviations from the expected atmospheric background neutrino flux [132]. However, IceCube 22-string has improved the limits of Super-Kamiokande and AMANDA by a factor of 3 to 5 for the muon flux due to muon neutrinos produced in the Sun during the annihilation of DM (for DM masses, $m_\chi > 250$ GeV). These limits can also be transformed into upper bounds for the DM-nucleon spin-dependent (SD) cross sections assuming that DM annihilates mainly into W^+W^- and $b\bar{b}$, i.e., $\sigma_{\rm SD} \leq 3 \times 10^{-4}(4 \times 10^{-2})$ pb for $m_\chi = 0.25(5)$ TeV, giving more stringent limits than the direct detection experiments [158].

CHAPTER 3

NEUTRINO PHYSICS

In the previous chapter, we described the large-scale neutrino telescopes that will play very important role in detecting signals from DM which depend on the interactions of neutrinos with matter and the initial neutrino spectra. Therefore, in this chapter, we present the theoretical framework for neutrino-nucleon interactions and the neutrino spectra from the decays of SM particles. We start with a short historical background for the discovery of neutrino and different flavors of neutrino, followed by the SM description of neutrino, and vacuum and matter oscillation effects on mixing of neutrino flavors.

The neutrino was first postulated by Wolfgang Pauli in 1930 to satisfy the conservation of energy, momentum and angular momentum in beta decay [159],

$$n^0 \rightarrow p^+ + e^- + \bar{\nu}_e. \tag{3.1}$$

Pauli originally called this particle "neutron". However, in 1932 James Chadwick discovered a much more massive nuclear particle and named it a "neutron" as well [160]. Enrico Fermi was the first to propose the theory for the beta decay and resolve the confusion by introducing the name "neutrino" (meaning the little neutral one) in 1934 [161]. The neutrino was first detected in 1956 in the neutrino experiment which is now known as the Cowan-Reines neutrino experiment [162]. The neutrinos produced by the beta decay were shot into protons resulting in neutrons and positrons

$$\bar{\nu}_e + p \rightarrow n^0 + e^+. \tag{3.2}$$

In the final stage, positron interacts with an electron and they annihilate into two gamma rays (positron annihilation) and neutron is captured by the medium, releas-

ing a gamma ray (neutron capture). Detection of both positron annihilation and the neutron capture gives a unique signature of the interaction given in Eq. (3.2). It was shown by the discovery of the muon neutrino in 1962 that the neutrinos could appear in different flavors [163]. After the discovery of the tau lepton in 1975 at the Stanford Linear Accelerator Center [164], an associated neutrino was looked for until the DONUT collaboration at Fermilab announced its discovery in 2000 [165].

In SM of particle physics, particle masses arise from Yukawa interaction terms ($\ell_R LH$) which couple right-handed fermion (ℓ_R) with its left-handed doublet (L) and the Higgs field (H). A left-handed doublet constitutes a left handed lepton and its corresponding neutrino, i.e.,

$$L \equiv \begin{pmatrix} \nu \\ \ell \end{pmatrix}_L , \tag{3.3}$$

where the left-handed neutrino state is

$$\nu_L = \frac{1}{2}(1-\gamma_5)\nu \ . \tag{3.4}$$

In SM, right-handed neutrinos do not exist, so Yukawa interactions leave the neutrinos massless. The neutrinos are also electrically neutral and interact only through the weak force. So, their interactions include exchange of massive vector bosons W and Z. Since W bosons are charged, the neutrino interactions with W exchange are often called charged-current (CC) interactions whereas the ones with Z exchange are called neutral-current (NC) interactions.

The interaction Lagrangian for the neutrino-W boson-charged lepton vertex is given by [166],

$$\mathcal{L}_{W-\ell} = -\Big(\frac{G_F M_W^2}{\sqrt{2}}\Big)^{1/2}\Big[\bar{\nu}\gamma^\mu(1-\gamma_5)\ell W_\mu^+ + \bar{\ell}\gamma^\mu(1-\gamma_5)\nu W_\mu^-\Big] \tag{3.5}$$

while the corresponding piece for the neutral gauge boson Z^0 ($\nu Z^0 \bar{\nu}$) is given by

$$\mathcal{L}_{0-\ell} = \frac{-1}{\sqrt{2}}\Big(\frac{G_F M_Z^2}{\sqrt{2}}\Big)^{1/2}\bar{\nu}\gamma^\mu(1-\gamma_5)\nu Z_\mu. \tag{3.6}$$

The term $G_F = 1.15 \times 10^{-5}$ GeV^{-2} represents the strength of the Fermi interaction. The masses of the weak bosons are related through the weak mixing angle θ_W by

$$M_Z^2 = M_W^2 / \cos^2 \theta_W. \tag{3.7}$$

In SM, the neutrinos are massless. However, the observation of neutrino oscillations implies nonzero neutrino mass [167] and a need for theory beyond SM.

3.1 Neutrino Oscillations

3.1.1 Neutrino Oscillations in Vacuum

In 1957 Bruno Pontecorvo [168] proposed that the neutrinos could change flavors in a process known as oscillations. Oscillations occur due to the difference between the flavor and mass eigenstates. The flavor eigenstates can be described as mixtures of the mass eigenstates, indicating that if a specific flavored neutrino is produced, it is plausible that a different flavor will be detected after traveling a certain distance for a fixed value of neutrino energy. This probability is a function of the distance between the source and the detector.

We can write the weak (flavor) eigenstate as a superposition of the mass eigenstates for a neutrino in the following way

$$|\nu_\ell(t=0)> = \sum_i U_{\ell j} |\nu_j> \tag{3.8}$$

where ν_ℓ represents the neutrino of a corresponding charged lepton ℓ of flavor e, μ, or τ and $|\nu_j>$ represents the mass eigenstate with eigenvalue m_j, with energy E_j and momentum p. The matrix $U_{\ell j}$ is the lepton mixing matrix which takes the form

$$\begin{pmatrix} \cos\theta & \sin\theta \\ -\sin\theta & \cos\theta \end{pmatrix} \tag{3.9}$$

for two-flavor mixing where θ represents the weak mixing angle. The mass eigenstates are actually the eigenstates of the time evolution operator $U = e^{-i\hat{H}t}$ where $\hat{H}$ is the Hamiltonian operator. Then, the neutrino flavor state at time t can be

found by evaluating the effect of the time evolution operator on the initial state, i.e.,

$$|\nu_\ell(t)>=\sum_j U_{\ell j} e^{-\imath E_j t}|\nu_j> \tag{3.10}$$

The neutrinos are highly relativistic ($E_\nu \gg m_\nu$), so that the ultra-relativistic approximation gives

$$p_{1,2} = E_\nu - \frac{m_{1,2}^2}{2E_\nu} \tag{3.11}$$

Then, the probability of finding a neutrino with flavor ℓ at a location L ($L \simeq t$) and time t becomes

$$P(\ell \to \ell; t) = |<\nu_\ell(t)|\nu_\ell(0)>|^2 = 1 - \sin^2 2\theta \sin^2\left(1.27\frac{\Delta m^2}{\mathrm{eV}^2}\frac{L}{\mathrm{km}}\frac{\mathrm{GeV}}{E_\nu}\right) \tag{3.12}$$

For three-flavor oscillations with a 3×3 matrix, there are 3 mass squared differences to consider: Δm^2_{12}, Δm^2_{13}, and Δm^2_{23}. The mixing matrix for this scenario is given by the Maki-Nakagawa-Sakata (MNS) matrix [169],

$$\begin{aligned} U &= \begin{pmatrix} c_{12}c_{13} & s_{12}s_{13} & s_{13}e^{-i\delta} \\ -s_{12}c_{23} - c_{12}s_{23}s_{13}e^{i\delta} & c_{12}c_{23} - s_{12}s_{23}s_{13}e^{i\delta} & s_{23}c_{13} \\ s_{12}s_{23} - c_{12}c_{23}s_{13}e^{i\delta} & -c_{12}s_{23} - s_{12}c_{23}s_{13}e^{i\delta} & c_{23}c_{13} \end{pmatrix} \\ &\times \begin{pmatrix} e^{i\alpha_1/2} & 0 & 0 \\ 0 & e^{i\alpha_2/2} & 0 \\ 0 & 0 & 1 \end{pmatrix} \end{aligned} \tag{3.13}$$

where $c_{ij} = \cos\theta_{ij}$ and $s_{ij} = \sin\theta_{ij}$. The terms α_1, α_2, and δ represent CP violating phases. In this scenario, the probability that a neutrino with flavor α will oscillate to a neutrino with flavor β is given by

$$\begin{aligned} P(\nu_\alpha \to \nu_\beta) = \delta_{\alpha,\beta} &- 4\sum_{i>j} Re(U^*_{\alpha i}U_{\beta i}U_{\alpha j}U^*_{\beta j})\sin^2(\frac{\pi L}{\lambda_{ij}}) \\ &+ 2\sum_{i>j} Im(U^*_{\alpha i}U_{\beta i}U_{\alpha j}U^*_{\beta j})\sin^2(\frac{2\pi L}{\lambda_{ij}}) \end{aligned} \tag{3.14}$$

where oscillation length in this case is λ_{ij} is defined as the oscillation length and given by

$$\lambda_{ij} = \frac{\pi}{1.27}\frac{E_\nu}{\mathrm{GeV}}\frac{\mathrm{eV}^2}{\Delta m^2_{ij}} \tag{3.15}$$

in units of kilometers.

In neutrino searches, in addition to the atmospheric neutrinos produced in air showers due to cosmic ray interactions in Earth's atmosphere, the extra-terrestrial neutrinos have also been detected from the Sun and from the Supernovae SN1987A. The neutrinos with energies of the order of few MeV originated from SN1987A were observed by the large neutrino detector experiments Irvine-Michigan-Brookhaven (IMB) [145, 170] and Kamiokande-II [146, 171]. Atmospheric neutrinos can have energies in the range of a few MeV to the energy of an incoming cosmic ray whereas solar neutrinos have energies in between a few MeV to about 18 MeV as also suggested by the Standard Solar Model (SSM) [172]. Evidence for the neutrino oscillations was observed in both solar and atmospheric neutrino studies. Having different neutrino energy regimes, these neutrino sources were useful in giving information about neutrino oscillation mechanisms and also putting bounds on the oscillation parameters (e.g mass splittings, mixing angles, etc.) which are summarized in Table 3.1.

Table 3.1: Solar neutrino experiments along with the reactor experiment KamLAND have placed constraints on the smaller mass splitting Δm^2_{12} and the mixing angle, θ_{12}. The atmospheric mixing parameters (Δm^2_{23}, θ_{23}) are found from experiments such as SuperK. The third mixing parameter θ_{13} has been determined to be $< 13^\circ$ from the Chooz collaboration. Atmospheric and solar neutrino experiments have shown that the MNS matrix consists of two large and one small mixing angles.

Mixing parameter	Value	References
θ_{12}	$33.9^{\circ+2.4^\circ}_{-2.2^\circ}$	[173]
Δm^2_{12}	$8.0^{+0.6}_{-0.4} \times 10^{-5}\mathrm{eV}^2$	[173]
θ_{23}	$45 \pm 7^\circ$	[174]
Δm^2_{23}	$2.4^{+0.6}_{-0.5} \times 10^{-3}\mathrm{eV}^2$	[174]
θ_{13}	$< 13^\circ$	[175]
Δm^2_{13}	$\approx \Delta m^2_{23}$	[175]

The atmospheric tau neutrinos are produced primarily due to $\nu_\mu \leftrightarrow \nu_\tau$ mixing. According to Eq. (3.15), for $E_\nu \gg$ GeV, atmospheric tau neutrino flux becomes negligible due to the large oscillation lengths.

3.1.2 Neutrino Oscillations in matter

The neutrino oscillation formalism changes significantly when the neutrinos propagate in the medium. Mass eigenstates acquire corrections due to interactions of flavor states with the matter in the medium. As an example, we can consider a two-flavor neutrino state propagation in a medium composed of free electrons with number density N_e. Due to CC interactions with the free electrons, an effective potential $V_e = \sqrt{2} G_F N_e$ is induced for the electron neutrinos [176]. With the addition of this potential term in the mass matrix, the lepton mixing matrix can be written in the form

$$\begin{pmatrix} \cos\theta_m & \sin\theta_m \\ -\sin\theta_m & \cos\theta_m \end{pmatrix} \tag{3.16}$$

which is similar to Eq. (3.9). Furthermore, the mixing angle in matter, θ_m, is given in terms of the vacuum mixing angle as

$$tan2\theta_m = \frac{\Delta m^2 \; sin2\theta}{\Delta m^2 \; cos2\theta - 2EV_e} \tag{3.17}$$

for neutrinos with energy, E. The eigenvalues of the mass matrix which are the effective masses in matter are given by

$$\mu_{1,2} = \frac{m_1^2 + m_2^2}{2} + EV_e \mp \frac{1}{2}\sqrt{(\Delta m^2 \; cos2\theta - 2EV_e)^2 + (\Delta m^2 \; sin2\theta)^2}. \tag{3.18}$$

Hence $\mu_{1,2}$ reduces to $m_{1,2}$ in the limit V_e goes to zero, i.e the vacuum case. Since V_e depends on the density of the medium, the mixing angle can also vary with the location. In matter oscillations, the resonance condition is defined as the value of the effective potential $V_{e,R}$ at which the difference between the effective masses is minimal and $tan2\theta_m$ changes sign, i.e

$$V_{e,R} = \frac{\Delta m^2\ cos2\theta}{2E}. \tag{3.19}$$

The survival probability calculations for the matter oscillations are in general done numerically, but some analytical expressions can be obtained in certain conditions. For example, in the adiabatic transition approximation, when the effective potential varies slowly relative to the difference between the effective masses at all points in the medium, the survival probability ($P(\nu_e \rightarrow \nu_e; t)$) of ν_e produced in the medium at $t = 0$ and exiting the medium at $t > 0$ depends on the initial state (mixing angle in the medium at the production point,$\theta_{m,0}$), the final state (vacuum mixing angle,θ) and a phase ($\delta(t)$);

$$\begin{aligned} P(\nu_e \rightarrow \nu_e; t) &= cos^2\theta_{m,0} cos^2\theta + sin^2\theta_{m,0} sin^2\theta + \\ &+ \frac{1}{2} sin2\theta_{m,0}\ sin2\theta\ cos\left(\frac{\delta(t)}{2E}\right), \end{aligned} \tag{3.20}$$

where

$$\delta(t) = \int_0^t \sqrt{(\Delta m^2\ cos2\theta - 2EV_e(t'))^2 + (\Delta m^2\ sin2\theta)^2}\, dt'. \tag{3.21}$$

The last term in Eq. (3.20) can be averaged out for $\delta(t) \gg E$ and the survival probability takes the form

$$P(\nu_e \rightarrow \nu_e; t) = \frac{1}{2}[1 + cos2\theta_m cos2\theta] \tag{3.22}$$

which can be much smaller than 1/2 since $cos2\theta_{m,0}$ and $cos2\theta$ can have opposite signs. It is interesting to note that the smaller the mixing angle in vacuum, the larger the deficit of the electron neutrinos in the final state. This is called Mikheyev-Smirnov-Wolfenstein (MSW) effect [177, 178].

The MSW effect has been widely studied in the literature: Three flavor oscillations in matter with constant density have been studied in [179, 180] and some approximate solutions have been presented in [181]. The analytical expressions for

the three flavor neutrino oscillation evolution operator and the transition probabilities can be found in [182]. Neutrino oscillations have also been studied in the case for varying matter densities [183, 184]. Lately, these neutrino oscillation effects have been included in some Monte Carlo approaches to compute the neutrino yields from DM annihilations [51, 185]. It has been presented that the yield of the neutrinos from DM annihilations in the Sun is enhanced or suppressed, depending on the DM annihilation channel. In addition, for DM particles with mass of order of few 100 GeV annihilating inside the Earth, the oscillation effects turned out to be negligible due to short distance between the source and the detector [51] and they are further suppressed when equal amounts of all neutrino flavors are produced at the source (a typical example is the neutralino DM which decays mainly into top quarks, W and Z bosons) [15]. For DM annihilations in the Sun, this symmetry in different neutrino flavors can be broken in the case for DM particles with mass close to 1 TeV and the neutrino oscillations can still be significant regardless of the symmetry at the source. This is due to tau leptons produced via CC interactions as the neutrinos propagate through, and tau decays into different neutrino flavors with different branching fractions (tau regeneration). All these results indicate that the neutrino flux that reach the detectors on the Earth due to the DM annihilation in the cores of the astrophysical objects strongly depends on the choice of the DM model and the model parameters.

3.2 Neutrino-Nucleon scattering

The DM signals in the neutrino telescopes depend mainly on the neutrino-nucleon interactions. The muon and shower fluxes are produced as a consequence of neutrino-nucleon interactions in the Earth or in the detector medium. The relevant processes are NC ($\nu_\ell N \to \nu_\ell X$) and CC ($\nu_\ell N \to \ell X$) processes.

According to SM, the amplitude M for scattering of neutrinos on target nucleons at rest ($E = m_p$) satisfies $M \sim G_F m_p E_\nu$ and the total cross section which is proportional to the ratio of the squared amplitude and the square of the center of

mass energy s, i.e $\sigma \sim |M|^2/s$, becomes $\sigma \sim G_F^2 E_\nu^2$ for $E_\nu \ll m_p$ (e.g solar and reactor neutrinos) and $\sigma \sim G_F^2 m_p E_\nu$ for $E_\nu \gg m_p$ (e.g; atmospheric neutrinos). For $E_\nu \gg m_p$ the neutrinos interact with the quarks inside the nucleon. Neutrinos and quarks can interact via an exchange of a W boson (CC interaction) or a Z boson (NC interaction). The neutrino gauge boson couplings are given in Eqs. (3.5) and (3.6). Corresponding interaction Lagrangians for the quarks are given by

$$\mathcal{L}_{W-q} = -\Big(\frac{G_F M_W^2}{\sqrt{2}}\Big)^{1/2}\Big[\bar{u}\gamma^\mu(1-\gamma_5)dW_\mu^+ + \bar{d}\gamma^\mu(1-\gamma_5)uW_\mu^-\Big] \tag{3.23}$$

for W exchange and

$$\mathcal{L}_{Z-q} = 2\sqrt{2}\Big(\frac{G_F M_Z^2}{\sqrt{2}}\Big)^{1/2}\sum_{A,q} g_{Aq}[\bar{q}_A\gamma^\mu q_A]Z_\mu \tag{3.24}$$

for Z exchange, where $A = \{L, R\}$ and $q = \{u, d, s, c, t, b\}$ and the couplings g_{Aq} (Z couplings) are given in Table 3.2 where θ_W ($s_W \equiv \sin\theta_W$) is defined in Eq. (3.7).

Table 3.2: Couplings for the interactions presented in Eq. (3.24) with Z boson exchange in neutrino-quark sub-processes.

q_{Aq} (Z couplings)	L	R
u, c, t	$\frac{1}{2} - \frac{2}{3}s_W^2$	$-\frac{2}{3}s_W^2$
d, s, b	$-\frac{1}{2} + \frac{1}{3}s_W^2$	$\frac{1}{3}s_W^2$

Then, in the low-energy limit, the differential cross sections for neutrino-quark interactions become [186]

$$\begin{aligned}
\frac{d\hat{\sigma}}{dy}(\bar{\nu}_\ell\bar{d} \to \bar{\ell}\bar{u}) = \frac{d\hat{\sigma}}{dy}(\nu_\ell d \to \ell u) &\simeq \frac{G_F^2\hat{s}}{\pi} \\
\frac{d\hat{\sigma}}{dy}(\bar{\nu}_\ell u \to \bar{\ell}d) = \frac{d\hat{\sigma}}{dy}(\nu_\ell\bar{u} \to \ell\bar{d}) &\simeq \frac{G_F^2\hat{s}}{\pi}(1-y)^2
\end{aligned} \tag{3.25}$$

for CC interactions and

$$\frac{d\hat{\sigma}}{dy}(\bar{\nu}\bar{q} \to \bar{\nu}\bar{q}') = \frac{d\hat{\sigma}}{dy}(\nu q \to \nu q') \simeq \frac{G_F^2 \hat{s}}{\pi}\left[g_{Lq}^2 + g_{Rq}^2(1-y)^2\right]$$
$$\frac{d\hat{\sigma}}{dy}(\nu\bar{q} \to \nu\bar{q}') = \frac{d\hat{\sigma}}{dy}(\bar{\nu} q \to \bar{\nu} q') \simeq \frac{G_F^2 \hat{s}}{\pi}\left[g_{Rq}^2 + g_{Lq}^2(1-y)^2\right] \qquad (3.26)$$

for NC interactions. These results are applicable for the neutrino energies in the range, $m_p \ll E_\nu \ll M_Z^2/m_p$ or GeV $\ll E_\nu \ll$ 10 TeV. Here, $y = 1 - E'/E_\nu$ and has the kinematic range $0 \leq y \leq 1$, where E' is the energy of the scattered lepton. In addition, $\sqrt{\hat{s}}$ is the center of mass energy of the neutrino-quark system, which is given by $\hat{s} = sx$, where x is the fraction of the total nucleon momentum carried by the quark. The momentum distribution functions, $q(x)$, describe the probability density for encountering a quark in a nucleon with a specific value of the fractional momentum x. Then, the quantities $p_q = \int_0^1 dx\, x\, q(x)$ give the fraction of the total nucleon momentum carried by the quark q. Integrating over the variable y, one can also obtain the total neutrino-quark CC and NC cross sections.

The nucleons contain valance quarks, virtual $q\bar{q}$ pairs and gluons. The neutrino-nucleon cross sections are found summing over all contributions using the integrals over the momentum distributions. The momentum distribution of the neutron is approximately the same as the proton with up and down-type quarks exchanged. After integrating over the quark distributions the differential cross sections take the approximate form

$$\frac{d\sigma}{dy} = \frac{G_F^2 s}{\pi}\left(a + b(1-y)^2\right) \qquad (3.27)$$

where a and b are numerical constants and a further integration over y yields the total cross sections in the form

$$\sigma = \frac{G_F^2 s}{\pi}\left(a + \frac{1}{3}b\right) \ . \qquad (3.28)$$

To be more precise, the total CC cross sections at $s \simeq 2E_\nu m_p$ are

$$\sigma(\nu_\ell p \to \ell X) = \frac{G_F^2 s}{\pi}\left(0.15 + \frac{1}{3}0.04\right), \quad \sigma(\bar{\nu}_\ell n \to \bar{\ell} X) = \frac{G_F^2 s}{\pi}\left(\frac{1}{3}0.15 + 0.04\right) \tag{3.29}$$

and

$$\sigma(\nu_\ell n \to \ell X) = \frac{G_F^2 s}{\pi}\left(0.25 + \frac{1}{3}0.06\right), \quad \sigma(\bar{\nu}_\ell p \to \bar{\ell} X) = \frac{G_F^2 s}{\pi}\left(\frac{1}{3}0.25 + 0.06\right). \tag{3.30}$$

Similar results can also be obtained for NC interactions. The differential cross sections are again in the form Eq. (3.27). It is shown in Ref. [15] that

$$\sigma(\nu p \to \nu' X) = \frac{G_F^2 s}{\pi}\left(0.058 + \frac{1}{3}0.022\right), \quad \sigma(\bar{\nu} p \to \bar{\nu}' X) = \frac{G_F^2 s}{\pi}\left(\frac{1}{3}0.058 + 0.0022\right) \tag{3.31}$$

and

$$\sigma(\nu n \to \nu' X) = \frac{G_F^2 s}{\pi}\left(0.064 + \frac{1}{3}0.019\right), \quad \sigma(\bar{\nu} n \to \bar{\nu}' X) = \frac{G_F^2 s}{\pi}\left(\frac{1}{3}0.064 + 0.019\right) \tag{3.32}$$

for NC interactions.

For practical purposes, differential cross sections given in Eq. (3.27) can be re-written as

$$\frac{d\sigma}{dE'} = \frac{2G_F^2 m_p}{\pi}\left[a + b\left(\frac{E'}{E_\nu}\right)^2\right] \tag{3.33}$$

with the help of

$$\frac{d\sigma}{dE'} \equiv \frac{1}{E_\nu}\frac{d\sigma}{dy}. \tag{3.34}$$

Numerically, apart from the corrections due to the type of nucleon (p or n) and neutrino (ν or $\bar{\nu}$) taking part in the interactions or the type of the interaction (CC or NC), the overall normalization of the neutrino-nucleon cross sections is given as

$$\frac{2G_F^2 E_\nu m_p}{\pi} \simeq 3.1 \times 10^{-38}\left(\frac{E_\nu}{\mathrm{GeV}}\right)\mathrm{cm}^2 \tag{3.35}$$

and we also note that Eqs. (3.29), (3.30), (3.31) and (3.32) indicate

$$\sigma_{\rm CC}/\sigma_{\rm NC} \simeq 3\ . \tag{3.36}$$

3.2.1 Interaction Length of Neutrinos in Medium

Having discussed the neutrino-nucleon cross sections, we can now estimate the interaction length of neutrinos in a given medium. As the neutrinos propagate in a medium, they interact with the nuclei in the medium. For the neutrino energies, GeV $\ll E_\nu \ll$ 10 TeV the CC and NC cross sections are given by Eqs. (3.29), (3.30), (3.31) and (3.32). The interaction length can be defined as the distance between two successive interactions which is then inversely related to the cross section and the density of the medium. Consequently, the neutrino-nucleon interaction length is given by

$$L_{int} = \frac{1}{\sigma_{\nu N}(E_\nu) N_A \rho} \tag{3.37}$$

where the nucleon number density in the medium with density ρ (in g/cm^3) is approximated to be $N_A\rho$ and $N_A = 6.022 \times 10^{23}{\rm g}^{-1}$ is Avogadro's number.

The density profile of the Earth has been determined in the Preliminary Earth Model [187] and can be represented by the following density profile,

$$\rho(r) = \begin{cases} 13.0885 - 8.8381x^2, & r < 1221.5 \\ 12.5815 - 1.2638x - 3.6426x^2 - 5.5281x^3, & 1221.5 < r < 3480 \\ 7.9565 - 6.4761x + 5.5283x^2 - 3.0807x^3, & 3480 < r < 5701 \\ 5.3197 - 1.4836x, & 5701 < r < 5771 \\ 11.2494 - 8.0298x, & 5771 < r < 5971 \\ 7.1089 - 3.8045x, & 5971 < r < 6151 \\ 2.691 + 0.6924x, & 6151 < r < 6346.6 \\ 2.9, & 6346.6 < r < 6356 \\ 2.6, & 6356 < r < 6368 \\ 1.02, & 6368 \leq r \leq R_\oplus. \end{cases} \tag{3.38}$$

The distance r is measured in km from the center of the Earth, and x represents the scaled radial variable $x = r/R_\oplus$ and the radius of the Earth is $R_\oplus = 6371$km. Taking the core density of the Earth, $\rho = 13\text{g/cm}^3$ and the neutrino-nucleon cross section, $\sigma_{\text{CC}} \simeq 10^{-38}(E_\nu/\text{GeV})\ \text{cm}^2$, one can simply show that the diameter of the Earth exceeds the neutrino CC interaction length for neutrinos with energy $E_\nu \leq 1 \times 10^4$ GeV. This bound can be lifted up when the density variations are taken into account. Thus, for neutrinos with energies, $E_\nu < 10$ TeV in transit through the Earth, the attenuation of the neutrino flux due to CC interactions is not significant.

However, in the Sun where the core density can reach values as high as one order of magnitude higher than the core density of the Earth, the neutrino-nucleon CC interactions play a significant role in the attenuation of the neutrino flux as the neutrinos propagate in the Sun. To first approximation, attenuation can be described with an exponential decrease in the flux over a distance δr. If the composition of the Sun is assumed to compose mostly of elemental hydrogen which has mass $m_H = 0.931$ GeV, the neutrino flux $d\phi/dE_\nu$ at a distance $r' = r + \delta r$ from the center of the Sun is related to the one at a distance r as

$$\frac{d\phi_\nu}{dE_\nu}(r + \delta r) = exp(-\rho(r)\sigma_{CC}\delta r/m_H)\frac{d\phi_\nu}{dE_\nu}(r) \tag{3.39}$$

where the Sun density profile is given by [188, 189]

$$\rho(r) = 236.93\,\text{g/cm}^3 \times \exp(-10.098\frac{r}{R_S}) \tag{3.40}$$

and $R_S = 6.955 \times 10^5$km is the radius of the Sun.

3.3 Neutrino Spectra from Standard Model Particle decay

In addition to neutrino-nucleon interactions, the signals in the neutrino telescopes depend strongly on the initial neutrino spectra as well, i.e., at the production point. Therefore, calculation of neutrino signals from the annihilation/decay of the DM particles requires information on the initial neutrino spectra. DM particles which are non-relativistic have energies close to their rest energy ($E_\chi \simeq m_\chi$). The neutrinos

with energy E_ν can be produced from the annihilation/decay of the DM or from the decay of quarks, charged leptons and gauge bosons which are produced by the annihilation/decay of the DM. The standard unpolarized decay distributions, in general, take one of the following forms

$$\frac{dN}{dx} = 2B_f(3x^2 - 2x^3) \tag{3.41}$$

$$\frac{dN}{dx} = 12B_f(x^2 - x^3) \tag{3.42}$$

$$\frac{dN}{dx} = B_f\delta(x-1) \tag{3.43}$$

in the rest frame of the decaying particle where $x = 2E_\nu/m_d$, m_d is the mass of the decaying particle and B_f is the decay branching fraction for a given decay channel. Once the distribution in the rest frame is known, the neutrino energy spectrum from a decaying particle with velocity β_d and energy $E_d = \gamma_d m_d$ is given by [55]

$$\left(\frac{dN_\nu}{dE_\nu}\right) = \frac{1}{2}\int_{E_-}^{E_+}\frac{d\epsilon}{\epsilon}\frac{1}{\gamma_d\beta_d}\left(\frac{dN}{d\epsilon}\right)^{\text{rest}} , \tag{3.44}$$

where $E_\mp = E_\nu\gamma_d^{-1}(1 \pm \beta_d)^{-1}$.

3.3.1 Neutrino spectrum from $\psi_{3/2} \to Z\nu$ decay channel

For the channel $\psi_{3/2} \to Z\nu$, the Breit-Wigner distribution is mainly used and is given as [59]

$$\frac{dN_\nu}{dE_\nu} = \frac{1}{(E_\nu^2 - E_{\nu Z}^2)^2 + E_{\nu Z}^2\Gamma_{\nu Z}^2}\left(\int_0^\infty \frac{dE}{(E^2 - E_{\nu Z}^2)^2 + E_{\nu Z}^2\Gamma_{\nu Z}^2}\right)^{-1} , \tag{3.45}$$

where the distribution peaks at

$$E_{\nu Z} = \frac{m_\chi}{2}\left(1 - \frac{m_Z^2}{m_\chi^2}\right) , \tag{3.46}$$

and

$$\Gamma_{\nu Z} = \frac{m_Z}{m_\chi}\Gamma_Z. \tag{3.47}$$

We take $\Gamma_Z = 2.5$ GeV.

3.3.2 Neutrino spectrum from $\tau^{\mp}$, $\mu^{\mp}$ decay channels

In this section, we present the ν_μ spectrum from μ and τ decays. The spectra for other neutrino flavors can be deduced from these results. For example, the ν_e spectrum from μ decay is identical to the ν_μ spectrum from τ decay and the ν_τ spectrum from τ decay to that of ν_μ from μ decay. For these three-body decays, the ν_μ spectrum from τ decay is given by Eq. (3.42) and from μ decay by Eq. (3.41) in the frame where the decaying particle is at rest. Then, after boosting these results by using Eq. (3.44) for charged leptons produced via the DM annihilation or decay, one can obtain

$$\frac{dN_{\nu_\mu}}{dE_{\nu_\mu}} = \begin{cases} \frac{B_f}{E_l}(\frac{5}{3} - 3x^2 + \frac{4}{3}x^3) & , \quad \mu \to \nu_\mu e \nu_e \\ \frac{2B_f}{E_l}(1 - 3x^2 + 2x^3) & , \quad \tau \to \nu_\tau \mu \nu_\mu \ , \end{cases} \tag{3.48}$$

where $x = \frac{E_{\nu_\mu}}{E_l} \leq 1$ and $E_l = m_\chi$ for the case of annihilation or $E_l = m_\chi/2$ for the case of decay. The decay branching fraction, $B_f = 0.18(1)$ for $\tau(\mu)$ decay. In addition to the three-body decays, τ can also decay into ν_τ via $\tau \to \nu_\tau M$ or $\tau \to \nu_\tau X$ where $M = \pi, \rho, a_1$ mesons and X indicates hadrons. The neutrino spectra from these channels are given as [190]

$$\frac{dN_{\nu_\tau}}{dE_{\nu_\tau}} = \begin{cases} \frac{B_f}{E_\tau}\frac{1}{r_M} \ \text{ when } \ \frac{E_\nu}{E_\tau} < r_M & \text{for mesons} \\ \frac{0.13}{0.3E_\tau} \ \text{ when } \ \frac{E_\nu}{E_\tau} < 0.3 & \text{for hadrons} \ , \end{cases} \tag{3.49}$$

where $r_M = 1 - m_M^2/m_\tau^2$ with m_M and m_τ being the mass of the meson M and the τ lepton, respectively. Here, $B_f = 0.12, 0.26, 0.13$ and $r_M = 0.99, 0.81, 0.52$ for $M = \pi, \rho, a_1$ respectively.

3.3.3 Neutrino spectrum from $b(\overline{b})$ and $c(\overline{c})$ decay channels

The b and c quarks hadronize before they decay into neutrinos. The hadronization effect is taken into account by scaling the initial quark energy, E_{in}, in the form $E_f = z_f E_{in}$, where $f = b, c$, $z_f = 0.73(0.58)$ for b (c) quarks [55, 58] and $E_{in} = m_\chi$ for an annihilating DM particle or $E_{in} = m_\chi/2$ for a decaying DM particle with mass m_χ.

The neutrino spectrum from the decay of f= b, $\overline{b}$, c or $\overline{c}$ from $\chi\chi \rightarrow f\bar{f}$ can also be approximated by the second equation in Eq. (3.48) (see also [55, 191]), i.e,

$$\begin{aligned} \frac{dN_\nu}{dE_\nu} &= \frac{2B_f}{E_f}(1-3x^2+2x^3) \text{ for } x \leq 1 \\ &= 0 \text{ otherwise }, \end{aligned} \tag{3.50}$$

where $x = \frac{E_\nu}{E_f}$ and

$$(E_f\ ,\ B_f) = \begin{cases} (0.73E_{in}\ ,\ 0.103) & b \text{ channel} \\ (0.58E_{in}\ ,\ 0.13) & c \text{ channel.} \end{cases} \tag{3.51}$$

3.3.4 Neutrino Spectrum from $W^\mp$ and Z decay channels

In the $W^\mp$ and Z decay channels, the neutrino spectrum from the decaying particle with velocity, β_B, and energy, E_B, can be obtained by using Eqs. (3.43) and (3.44), i.e,

$$\begin{aligned} \frac{dN_\nu}{dE_\nu} &= \frac{n_f B_f}{E_B\beta_B} \text{ for } \frac{E_B}{2}(1-\beta_B) < E_\nu < \frac{E_B}{2}(1+\beta_B) \\ &= 0 \text{ otherwise }, \end{aligned} \tag{3.52}$$

where

$$(n_f\ ,\ B_f) = \begin{cases} (1\ ,\ 0.105) & W \text{ channel,} \\ (2\ ,\ 0.067) & Z \text{ channel.} \end{cases} \tag{3.53}$$

3.3.5 Neutrino spectrum from $t(\overline{t})$ decay channel

The top quark decays into a W boson and a b quark ($t \rightarrow Wb$) with a branching fraction close to unity. Thus, the sum of neutrino spectra of W and b channels gives the required spectrum, i.e,

$$\left(\frac{dN_\nu}{dE_\nu}\right)^{rest}_{t\overline{t}} = \left(\frac{dN_\nu}{dE_\nu}\right)_{W^+W^-} + \left(\frac{dN_\nu}{dE_\nu}\right)_{b\overline{b}}. \tag{3.54}$$

Then, boosting this expression yields the neutrino spectrum from top quarks moving with velocity β_t and energy $E_t = \gamma_t m_t$ [58],

$$\frac{dN_\nu}{dE_\nu} = \left(\frac{dN_\nu}{dE_\nu}\right)_W + \left(\frac{dN_\nu}{dE_\nu}\right)_b , \tag{3.55}$$

where

$$\begin{aligned}\left(\frac{dN_\nu}{dE_\nu}\right)_W &= \frac{B_W}{2\gamma_t\beta_t E_W \beta_W} ln \frac{\min(E_+, \epsilon_+)}{\max(E_-, \epsilon_-)} \\ &\quad \text{if } \gamma_t(1-\beta_t)\epsilon_- < E_\nu < \gamma_t(1+\beta_t)\epsilon_+ \\ &= 0 \text{ otherwise} ,\end{aligned} \tag{3.56}$$

and

$$\begin{aligned}\left(\frac{dN_\nu}{dE_\nu}\right)_b &= \frac{B_b}{2\gamma_t\beta_t E_d} D_b[E_-/E_d, \min(1, E_+/E_d)] \\ &\quad \text{if } E_\nu < \gamma_t(1+\beta_t)E_d \\ &= 0 \text{ otherwise} ,\end{aligned} \tag{3.57}$$

where $B_W = 0.105$,$B_b = 0.103$,$\epsilon\mp = E_W(1 \mp \beta_W)/2$, $E_\mp = E_\nu \gamma_t^{-1}(1 \pm \beta_t)^{-1}$ and $E_d = 0.73E_b$ with E_W, β_W and E_b being equal to their values in the top-quark rest frame, i.e,

$$\begin{aligned}E_b &= \frac{m_t^2 - m_W^2}{2m_t} \\ E_W &= \frac{m_t^2 + m_W^2}{2m_t} \\ \beta_W &= \frac{E_b}{E_W}.\end{aligned} \tag{3.58}$$

The function D_b is given by

$$D_b[m, n] = \frac{1}{3}\left[9(m^2 - n^2) - 4(m^3 - n^3) + 6ln\left(\frac{n}{m}\right)\right]. \tag{3.59}$$

3.3.6 Neutrino spectrum from $\psi_{3/2} \to l^+ l^- \nu$ decay channel

In the zero mass limit, the primary lepton (l^+ or l^- or ν) spectrum from the decay channel, $\psi_{3/2} \to l^+ l^- \nu$, can be approximated to be

$$\frac{dN_{l(\nu)}}{dE_{l(\nu)}} = \frac{60}{m_{\psi_{3/2}}} x^4 (1-x) \;\; \text{where} \;\; x = \frac{2E}{m_{\psi_{3/2}}} \leq 1 \; , \tag{3.60}$$

by using the results in [192]. In order to obtain the spectrum for the secondary neutrinos produced from the primary charged lepton decays, one can use

$$\frac{dN_\nu}{dE_\nu} = \int_{E_\nu}^{m_{\psi_{3/2}}/2} dE_l \left(\frac{1}{N_l} \frac{dN_l}{dE_l} \right) \left(\frac{dN_\nu}{dE_\nu} \right)_{l \to \nu} . \tag{3.61}$$

Here, $\frac{dN_l}{dE_l}$ is the primary charged lepton spectrum given by Eq. (3.60) and the spectra, $\left(\frac{dN_\nu}{dE_\nu}\right)_{l\to\nu}$ are given by Eqs. (3.48) and (3.49). Then, the secondary ν_μ spectrum is derived to be

$$\left(\frac{dN_{\nu_\mu}}{dE_{\nu_\mu}} \right) = \frac{5 B_f}{m_{\psi_{3/2}}} (1 - 6x^2 + 8x^3 - 3x^4) \; , \tag{3.62}$$

from the primary μ decays and

$$\left(\frac{dN_{\nu_\mu}}{dE_{\nu_\mu}} \right) = \frac{6 B_f}{m_{\psi_{3/2}}} (1 - 10x^2 + 20x^3 - 15x^4 + 4x^5) \; , \tag{3.63}$$

from the primary τ decays, requiring that $x \leq 1$ in each case where $x = 2E_\nu / m_{\psi_{3/2}}$. Finally, for the ν_τ spectrum from the primary τ decays accompanied with the meson/hadron production, we find

$$\left(\frac{dN_{\nu_\tau}}{dE_{\nu_\tau}} \right) = \frac{3 B_f}{r_M m_{\psi_{3/2}}} \left(1 - \frac{5}{r_M^4} x^4 + \frac{4}{r_M^5} x^5 \right) \; , \tag{3.64}$$

with the requirement $r_M > x$.

CHAPTER 4

DETECTING DARK MATTER VIA NEUTRINOS

In this chapter, with an aim to detect DM with neutrino telescopes, the required theoretical tools to calculate the muon and shower fluxes, as well as the corresponding event rates in the neutrino telescopes are presented.

The main difficulty in detecting a neutrino signal with DM origin is to overcome the atmospheric neutrino and muon signals which originate from the interaction of high energy cosmic rays with the nuclei in the atmosphere. It may often be impossible to eliminate these background signals, however, statistically promising signal detection significances can be achieved with the analysis of different signal topologies in the detector (upward muon, contained muon, shower events). Depending on the detector design, relative locations of the detector and the source, and on the nature of DM, some topologies may provide better statistics than the others.

We start this chapter with the introduction of the atmospheric muon neutrinos, the current data and parametrizations. In the following sections, we present the theoretical framework for calculating the final muon and shower fluxes due to DM annihilation/decay in the Galaxy/astrophysical objects.

4.1 Atmospheric Neutrino Background

In the upper atmosphere, shower of hadrons (e.g. pion or kaon showers) are produced in the interactions of primary cosmic rays (mostly protons) with the air nuclei. The decay of pions and kaons produce muons and muon neutrinos and the subsequent decay of muons produce electrons, electron neutrinos and additional muon neutrinos. According to this simple kinematic chain, one expects to observe a flux ratio of 2-to-1 muon neutrinos to electron neutrinos. However, at high energies (i.e $E_\mu > 10$ GeV) the muons are stopped before they decay and this reduces the flux of electron

Table 4.1: Parameters for the atmospheric ν_μ and $\bar{\nu}_\mu$ flux, in units of $\mathrm{GeV}^{-1}\mathrm{km}^{-2}\mathrm{yr}^{-1}\mathrm{sr}^{-1}$.

γ	1.74
a	0.018
b	0.024 GeV^{-1}
c	0.0069
e	0.00139 GeV^{-1}
N_0	1.95×10^{17} for ν 1.35×10^{17} for $\overline{\nu}$.

neutrinos. The pion decay becomes more efficient as the propagation length increases in the atmosphere. Thus, the atmospheric neutrino flux has a directional dependence and increases with the zenith angle, θ. The parametric form for the atmospheric muon neutrino flux is given in Ref. [193] as

$$\left(\frac{d\phi_\nu}{dE_\nu d\Omega}\right)_{\mathrm{ATM}} = N_0 {E_\nu}^{-\gamma-1}\left(\frac{a}{1+bE_\nu cos\theta}+\frac{c}{1+eE_\nu cos\theta}\right) \tag{4.1}$$

in units of $\mathrm{GeV}^{-1}\mathrm{km}^{-2}\mathrm{yr}^{-1}\mathrm{sr}^{-1}$ and E_ν is given in GeV. This formula does not account for the prompt neutrino flux [194], however, for the energy range of interest, the prompt atmospheric neutrino flux is negligible. The values of the parameters N_0, γ, a, b, c and e, given in Table 4.1, were determined by fitting angle-dependent atmospheric neutrino data from Ref. [195].

Using Eq. (4.1), one can also obtain the angle-averaged atmospheric muon neutrino flux (which is a good approximation and will be used later in this study) as

$$\left(\frac{d\phi_\nu}{dE_\nu d\Omega}\right)_{\mathrm{ATM,avg}} = N_0 {E_\nu}^{-\gamma-1}\left(\frac{a}{bE_\nu}\ln(1+bE_\nu)+\frac{c}{eE_\nu}\ln(1+eE_\nu)\right). \tag{4.2}$$

In Fig. 4.1, we show the angle-averaged flux from Eq. (4.2) and the flux from Eq. (4.1) with $\theta = 60^\circ$ and the integrated flux measured by the AMANDA-II detector from Ref. [73]. The angle-averaged flux is a bit larger than the flux at 60°, so for θ

less than 60°, using the angle-averaged atmospheric flux gives a small overestimate of the atmospheric background.

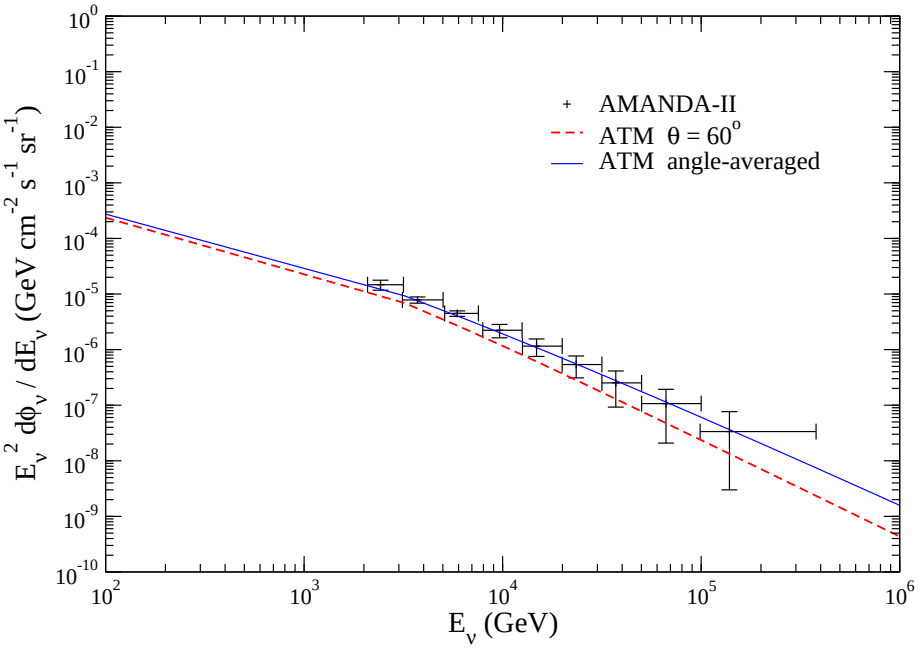

Figure 4.1: Angle-averaged atmospheric muon neutrino ($\nu_\mu + \overline{\nu}_\mu$) flux (solid line) and the atmospheric flux for fixed $\theta = 60°$ (dashed line) compared with the angle-averaged ($\nu_\mu + \overline{\nu}_\mu$) flux from AMANDA-II muon neutrino flux measurements [73].

4.2 Neutrino Signals from Dark Matter

4.2.1 Dark Matter Annihilation/Decay in the Galactic center (GC)

All three flavors of neutrinos can be generated in the GC due to the annihilation or decay of DM particles with mass m_χ. Then, the neutrino flux at the Earth for a given neutrino flavor is

$$\frac{d\phi_\nu}{dE_\nu} = R \times \left(\sum_F B_F \frac{dN_\nu^F}{dE_\nu} \right) \tag{4.3}$$

where R (annihilation/decay rate) is given by:

$$R \equiv R_{ann} = B\frac{\langle\sigma v\rangle}{8\pi m_\chi^2}\int d\Omega \int_{l.o.s} dl(\theta)\rho^2(l), \tag{4.4}$$

for the case of annihilation, and

$$R \equiv R_{dec} = \frac{1}{4\pi m_\chi \tau}\int d\Omega \int_{l.o.s} dl(\theta)\rho(l), \tag{4.5}$$

for the case of decay where dN_ν^F/dE_ν is the initial neutrino spectrum for a given annihilation or decay channel F with branching fraction B_F, B is the boost factor (enhancement of the annihilation cross section), τ is the decay time, $\rho(l)$ is the DM density, integral is over the line of sight (l.o.s) within a solid angle $\Delta\Omega = 2\pi(1 - cos\theta_{\max})$, centered in the GC. In literature, for practical reasons the dimensionless quantity $\langle J_n\rangle_\Omega$ is defined [61, 63];

$$\langle J_n\rangle_\Omega = \int \frac{d\Omega}{\Delta\Omega}\int_{l.o.s}\frac{dl(\theta)}{R_\circ}\left(\frac{\rho(l)}{\rho_\circ}\right)^n \tag{4.6}$$

where $l(\theta)$ is the distance from us in the direction of θ which is the cone half angle from the GC, $R_\circ$ is the distance of the solar system from the GC and $\rho_\circ$ is the local density near the solar system, which are taken to be $R_\circ = 8.5$ kpc and $\rho_\circ = 0.3$ GeVcm^{-3} [196]. With these definitions, the neutrino flux can be re-written as

$$\frac{d\phi_\nu}{dE_\nu} = R_\circ\rho_\circ^2 B\frac{\langle\sigma v\rangle}{8\pi m_\chi^2}\left(\sum_F B_F\frac{dN_\nu^F}{dE_\nu}\right)\langle J_2\rangle_\Omega\Delta\Omega \tag{4.7}$$

for the case of annihilation, and

$$\frac{d\phi_\nu}{dE_\nu} = R_\circ\rho_\circ\frac{1}{4\pi m_\chi\tau}\left(\sum_F B_F\frac{dN_\nu^F}{dE_\nu}\right)\langle J_1\rangle_\Omega\Delta\Omega \tag{4.8}$$

for the case of decay. The neutrino energy distribution, dN_ν^F/dE_ν for different channels can be found in the last section of this chapter. In our calculations, we take DM annihilation cross section to have the typical thermal relic value $\langle\sigma v\rangle = 3\times10^{-26}$ cm^{3}s^{-1} (see Appendix A) and we consider the Navarro-Frenk-White (NFW) profile [92]

$$\rho(r) = \frac{\rho_s}{(r/R_s)(1+r/R_s)^2} \quad , \tag{4.9}$$

or the cored isothermal profile

$$\rho(r) = \frac{\rho_s}{(1+(r/R_s)^2} \quad , \tag{4.10}$$

where ρ_s and R_s are the parameters which vary from halo to halo and r is the distance from the GC. In our calculations, for the NFW (isothermal) profile we set $\rho_s = 0.2589(3.0647)$ GeV/cm^3 and $R_s = 20(2.8)$ kpc so that the DM density in the vicinity of the solar system ($r = R_o = 8.5$ kpc) takes the typical value $\rho(R_o) = 0.3$ GeV/cm^3 as mentioned above. Using these definitions, we can write $r = \sqrt{R_o^2 + l^2 - 2R_o l\cos\theta}$ and the upper limit for the l integral in Eq. (4.6) can be obtained as $l_{\rm max} = R_o\cos\theta + \sqrt{R_s^2 - R_o^2\sin^2\theta}$ for a given θ. For the NFW profile, some values for $\langle J_2\rangle_\Omega\Delta\Omega$ and $\langle J_1\rangle_\Omega\Delta\Omega$ are summarized in Table 4.2.

Table 4.2: The values of J factors for NFW profile for $\theta_{\rm max} = 0.1^\circ, 1^\circ, 5^\circ, 25^\circ, 50^\circ, 70^\circ, 90^\circ$.

	0.1°	1°	5°	25°	50°	70°	90°
$\langle J_2\rangle_\Omega\Delta\Omega$	0.14	1.35	5.94	19.68	27.75	31.73	33.42
$\langle J_1\rangle_\Omega\Delta\Omega$	0.00027	0.018	0.30	3.69	8.79	12.24	14.90

The main differences between the signals from the decay and the annihilation processes appear in

(i) the maximum possible neutrino energy: $E_m = m_\chi$ for the case of annihilation and $E_m = m_\chi/2$ for the case of decay,

(ii) the overall normalizations which we denote as R_{ann} and R_{dec} following Eqs. (4.4) and (4.5) for annihilation and decay, respectively: The ratio of the rates for neutrino signals from annihilation and decay of DM can be obtained as

$$\frac{R_{ann}}{R_{dec}} = \frac{B\langle\sigma v\rangle\rho_\circ\tau}{2m_\chi}\frac{\langle J_2\rangle}{\langle J_1\rangle} \tag{4.11}$$

by using Eqs. (4.4) and (4.5). Thus, for a given decay channel, F, the shape of the final muon flux from the decay of a DM particle with mass m_χ is the same as that from the annihilation of a DM particle with mass $m_\chi/2$, and the ratio of the overall normalizations can be determined from Eq. (4.11). Thus, for simplicity, in the next chapter we will present our model-independent results only for the annihilating DM particle. For a decaying DM particle, muon fluxes can be obtained by re-scaling our results with the help of Eq. (4.11), and

(iii) the cone size dependence of the J factors which is quite different for the case of annihilating DM than for decaying DM (see Table 4.2). The difference between DM density contributions to DM annihilation and decay can also be seen in Fig. 4.2, where we present $\langle J_n \rangle_\Omega \Delta\Omega$ factors for DM annihilation ($n = 2$) and DM decay ($n = 1$) evaluated for a cone wedge between $\theta_{\rm max} - 1^\circ$ and $\theta_{\rm max}$ around the GC. We note that moving the wedge away from the GC leads to a significant reduction of the signal from annihilating DM due to the dependence of $\langle J_2 \rangle_\Omega \Delta\Omega$ on square of the density (see Eq. (4.6)). We find that the signal is reduced by a factor of 17 when the wedge is moved from 1° to 90° off the GC. On the other hand, in a wedge between 50° and 90° around the GC, the value of $\langle J_2 \rangle_\Omega \Delta\Omega$ is about 5.6, a value close to what one obtains for a cone centered at the GC with $\theta_{\rm max} = 5^\circ$.

In contrast, for a decaying DM, the signal from a wedge between $\theta_{\rm max} - 1^\circ$ and $\theta_{\rm max}$ around the GC increases with $\theta_{\rm max}$ for $\theta_{\rm max} < 30^\circ$ and decreases slowly for higher $\theta_{\rm max}$. For example, $\langle J_1(1^\circ) \rangle_\Omega \Delta\Omega = 0.018$ whereas $\langle J_1(30^\circ) - J_1(29^\circ) \rangle_\Omega \Delta\Omega = 0.2$ which is only a factor of 2 higher than $\langle J_1(90^\circ) - J_1(89^\circ) \rangle_\Omega \Delta\Omega = 0.1$. This is a consequence of the dependence of the signal for a decaying DM particle on density which is one power less when compared to an annihilating DM particle. An increase in the size of the wedge (i.e., the volume of the source region) can result in an enhancement in the signal even if the chosen wedge is away from the GC.

4.2.2 Dark Matter Annihilation in the Earth and in the Sun

The DM particles can be captured in the core of the Sun or the Earth by interacting with the nuclei in the medium (see Appendix B). This results in a DM density

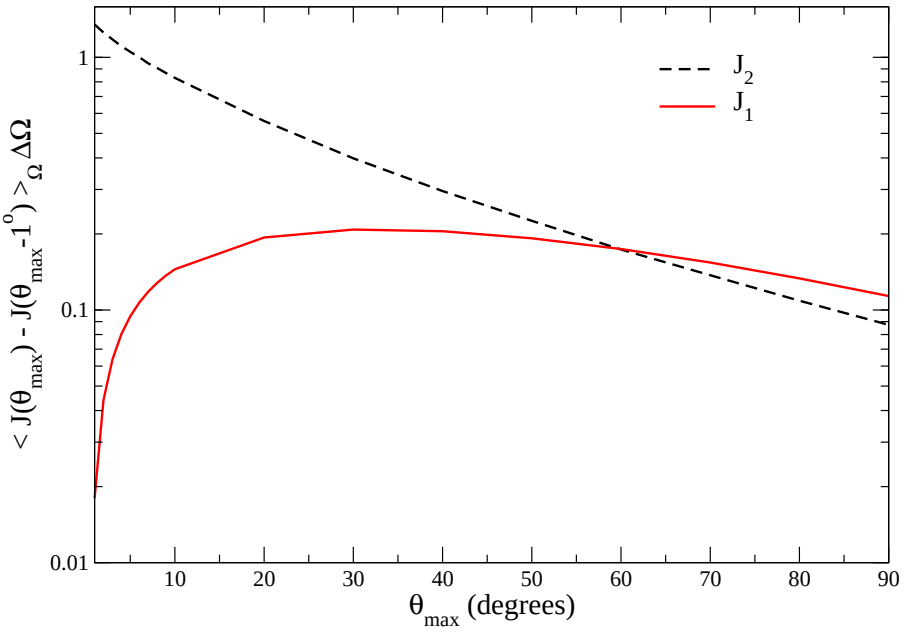

Figure 4.2: J factor values both for annihilating (dashed line) and decaying (solid line) DM models for a wedge between $\theta_{\max} - 1^\circ$ and $\theta_{\max}$ about the Galactic center as a function of $\theta_{\max}$.

in the core that is considerably higher than in the Galactic halo. The capture rate (C) depends on the composition of the medium, the DM-nucleus interaction cross sections (σ_0^i), the DM mass (m_χ), the local DM density ($\rho_\circ$) and velocity ($\overline{v}$) distribution of DM in the halo. After being accumulated in the core of these dense objects, the DM annihilates with rate Γ_A into SM particles which may further decay into neutrinos. These neutrinos can reach Earth-based detectors and create fluxes of charged leptons as a consequence of neutrino CC interactions.

The resulting fluxes depend on how the capture and annihilation processes have occurred initially, however, in equilibrium these two processes are related: for every two DM particles captured, one annihilation takes place so

$$\Gamma_A = \frac{C}{2} \,. \tag{4.12}$$

This equilibrium condition leads to a maximal flux which depends on the capture rate given by [58, 90, 91, 197, 198],

$$\begin{aligned} C &= c\frac{\rho_{0.3}}{(m_\chi/\mathrm{GeV})\overline{v}_{270}}\sum_i F_i(m_\chi)\, f_i\, \phi_i\, S(m_\chi/m_{N_i}) \\ &\quad \times\frac{\sigma_0^i}{10^{-8}\ \mathrm{pb}}\frac{1\ \mathrm{GeV}}{m_{N_i}}, \end{aligned} \tag{4.13}$$

where

$$\rho_{0.3} = \frac{\rho_\circ}{0.3\ \mathrm{GeV/cm}^3}\,, \qquad \overline{v}_{270} = \frac{\overline{v}}{270\mathrm{km/s}} \tag{4.14}$$

and

$$c = \begin{cases} 4.8\times 10^{11}\mathrm{s}^{-1} & \text{Earth,} \\ 4.8\times 10^{20}\mathrm{s}^{-1} & \text{Sun.} \end{cases} \tag{4.15}$$

The summation in Eq. (4.13) is over all species of nuclei in the astrophysical object, m_{N_i} is the mass of the ith nuclear species with mass fraction f_i relative to the Sun (or the Earth). The kinematic suppression factor, denoted by $S(m_\chi/m_{N_i})$, for a capture of DM particle with mass m_χ by a nucleus with mass m_{N_i} is given by [58, 90, 91, 197, 198]

$$S(x) = \left(\frac{B^{1.5}}{1+B^{1.5}}\right)^{\frac{2}{3}} \tag{4.16}$$

where

$$B(x) = \frac{3}{2}\frac{x}{(x-1)^2}\left(\frac{<v_{\mathrm{esc}}>}{\overline{v}}\right)^2. \tag{4.17}$$

For the Sun, $<v_{\mathrm{esc}}>= 1156$ km/s and for the Earth, $<v_{esc}>= 13.2$ km/s. We also note that $S(x)\to 1$ for $x\to 1$, which means that the capture process is kinematically suppressed if m_χ differs from m_{N_i}, and there is no suppression if these masses are the same.

The other quantities in the capture rate expression are the form factor suppression $F_i(m_\chi)$ and the velocity distribution function ϕ_i of the ith element. The former one is due to the finite size of the nucleus which disrupts the coherence in the scattering process, thus, it is a negligible effect for the capture by hydrogen and helium nuclei whereas it becomes significant for larger nuclei (see Appendix B for details). The velocity distribution function ϕ_i depends on the velocity distribution squared

of the element averaged over the volume of the astrophysical object ($< v_i^2 >$) and is given as [58, 90, 91, 197, 198]

$$\phi_i = \frac{< v_i^2 >}{< v_{\rm esc}^2 >}. \tag{4.18}$$

If the massive astrophysical object is far from equilibrium, which is most likely the case for the Earth, the annihilation rate is not only dependent on the capture rate but also on the annihilation cross section ($\langle \sigma v \rangle$). The number of DM particles changes due to the interplay between the capture and the annihilation according to the relation

$$\frac{dN}{dt} = C - C_A N^2 \tag{4.19}$$

which leads to

$$N(t) = \sqrt{\frac{C}{C_A}} tanh(t\sqrt{CC_A}) \ , \tag{4.20}$$

where

$$C_A \ = \ \frac{\langle \sigma v \rangle}{V_{\rm e}} \tag{4.21}$$

and $V_{\rm e}$ is the effective volume of the core of the Earth or the Sun with a radius defined as the location where the gravitational potential of the DM becomes comparable to the core temperature. For the Sun, it is found that $V_{\rm e} = 2 \times 10^{29} (m_\chi^{10})^{-3/2}$ cm^3 [199] and for the Earth, $V_{\rm e} = 6 \times 10^{25} (m_\chi^{10})^{-3/2}$ cm^3 [90] where m_χ^{10} is the DM mass in units of 10 GeV. Then, using

$$\Gamma_A = \frac{1}{2} C_A N^2 \tag{4.22}$$

we find

$$\Gamma_A \ = \ \frac{C}{2} \tanh^2(t\sqrt{CC_A}) \ . \tag{4.23}$$

It is clear from this relation that the equilibrium condition (see Eq. (4.12)) holds only when $t\sqrt{CC_A} \gg 1$.

The flux of neutrinos of flavor i from DM annihilation into SM particles can be written as

$$\left(\frac{d\phi_\nu}{dE_\nu}\right)_i = \frac{\Gamma_A}{4\pi D_\circ^2} \sum_F B_F \left(\frac{dN_\nu}{dE_\nu}\right)_{F,i}, \tag{4.24}$$

where $(dN_\nu/dE_\nu)_{F,i}$ is the differential energy spectrum of neutrino flavor i from production of particles in channel F. In general, this energy spectrum is a function of the neutrino energy E_ν and the energy of the produced particle, E_{in}. The quantity $D_\circ$ is the Sun-Earth distance for neutrinos produced in the core of the Sun, or the radius of the Earth ($R_\oplus$) for the neutrinos created in the core of the Earth. The sum in Eq. (4.24) is over all annihilation channels F weighted with corresponding branching fractions B_F.

One can also compare the overall normalizations (i.e the pre-factors of $\sum_F B_F(dN_\nu/dE_\nu)_F$) of the neutrino fluxes due to DM annihilation in the GC (Eq. (4.7)) and in the cores of the astrophysical objects (Eq. (4.24)). The results (in units of km^{-2} yr^{-1}) for different DM masses ranging from 200 GeV to 1 TeV are presented in Table 4.3. For illustration, the boost factor of $B = 100$ and the cone half angle of $\theta_{\rm max} = 1^\circ$ are chosen for the signal from the GC and NFW DM density profile is assumed. Clearly, these results can be re-scaled for different values of boost factor, cone half angle and for different DM density profiles.

4.3 Dark Matter Signals in Neutrino Telescopes

The neutrinos produced via the annihilation or decay of the DM particles in the GC or those produced from subsequent annihilation of DM particles after being captured in the astrophysical objects can be detected in the Earth-based neutrino telescopes. The muon neutrino (ν_μ) interacting with the matter via CC interactions inside the detector may result in the muon leaving a track in the detector (contained muon events). A similar type of interaction may also occur outside the detector (usually below the detector) and the produced muons arrive at the detector after loosing some fraction of their initial energies (upward muon events). In addition to the contained and upward muon events, all three flavors of neutrinos may interact

Table 4.3: Overall normalizations for the neutrino fluxes from dark matter annihilation in the Galactic center, in the Sun and in the Earth. For the signals from Galactic center, the value of the boost factor is set to be 100 and the cone half angle to be 1°. The attenuation of the neutrino flux in the solar medium is not taken into account.

m_χ (GeV)	GC (km^{-2} yr^{-1})	Sun (km^{-2} yr^{-1})	Earth (km^{-2} yr^{-1})
200	93	611	240
300	41	425	136
400	23	272	72
500	15	195	41
600	10	144	32
700	8	110	23
800	6	93	18
900	5	76	14
1000	4	59	9

with the matter inside the detector through NC interactions and produce showers (shower events or cascade events). Furthermore, through CC interactions electrons (e) and taus (τ) can also be created from ν_e's and ν_τ's. However, they don't result in any track-like events as the muons (μ) do since electrons experience too many scatterings due to their low mass and the taus decay so fast. Thus, these events are also considered as shower events. In this study, we make a clear distinction between contained, upward muon and shower events. The most straightforward evaluation is for contained muon events, so we start with this case.

4.3.1 Contained and Upward Muon Events

For a given muon neutrino spectrum, $\frac{d\phi_\nu}{dE_\nu}$, at Earth the contained muon flux in the detector can be calculated as

$$\begin{aligned} \frac{d\phi_\mu}{dE_\mu} &= \int_{E_\mu}^{E_m} dE_\nu \left(\frac{d\phi_\nu}{dE_\nu}\right) \frac{dP_{CC}}{dE_\mu} \\ &+ (\nu \to \bar{\nu}) \,, \end{aligned} \tag{4.25}$$

where E_m is the maximum neutrino energy. The quantity dP_{CC} is the probability for a neutrino with energy E_ν to be converted into a muon within the energy interval of dE_μ, i.e.,

$$dP_{CC} = dE_\mu \frac{N_A \rho}{2} \left(\frac{d\sigma_\nu^p(E_\nu, E_\mu)}{dE_\mu} + (p \to n) \right) , \tag{4.26}$$

where $N_A = 6.022 \times 10^{23}$ is Avogadro's number and $N_A\rho/2$ is assumed to be the number density of both protons and neutrons in the medium. The differential cross sections $d\sigma_\nu^{p,n}/dE_\mu$ are the weak scattering cross sections of (anti-)neutrinos on the nucleons, which can be approximated by [186]

$$\frac{d\sigma_{\nu,\overline{\nu}}^{p,n}}{dE_\mu} = \frac{2m_p G_F^2}{\pi} \left(a_{\nu,\overline{\nu}}^{p,n} + b_{\nu,\overline{\nu}}^{p,n} \left(\frac{E_\mu}{E_{\nu,\overline{\nu}}} \right)^2 \right) . \tag{4.27}$$

The parameters a and b for CC and NC scatterings are shown in Table 4.4 and in Table 4.5, respectively (see also Section 3.2).

Table 4.4: Parameters for the CC neutrino-nucleon differential cross section, as noted in Ref. [186].

a_ν^p	0.15	b_ν^p	0.04
$a_{\overline{\nu}}^p$	0.04	$b_{\overline{\nu}}^p$	0.15
a_ν^n	0.25	b_ν^n	0.06
$a_{\overline{\nu}}^n$	0.06	$b_{\overline{\nu}}^n$	0.25

Table 4.5: Parameters for the NC neutrino-nucleon differential cross section, as noted in Ref. [186].

a_ν^p	0.058	b_ν^p	0.022
$a_{\overline{\nu}}^p$	0.019	$b_{\overline{\nu}}^p$	0.064
a_ν^n	0.064	b_ν^n	0.019
$a_{\overline{\nu}}^n$	0.022	$b_{\overline{\nu}}^n$	0.058

In addition to the contained muon events, the muons can also be produced in the rock near the detector. These high energy muons produced in neutrino CC

interactions lose energy before they reach the detector as they travel through the rock or ice (upward muon events). The average energy loss of the muons with energy E over a distance dz during their passage through a medium with density ρ is given by

$$\langle \frac{dE}{dz} \rangle = -(\alpha + \beta E)\rho \ , \tag{4.28}$$

where α accounts for the ionization energy loss [200] and is relatively insensitive to the composition of the medium. The radiative energy loss due to bremsstrahlung, pair production and photonuclear scattering is characterized by β which increases with energy from about $\simeq 3\times 10^{-6}$ cm^2/g for $E_\mu \sim 10^2$ GeV to about $\simeq 5-6\times 10^{-6}$ cm^2/g for $E_\mu \sim 10^9$ GeV for muons in the standard rock [201, 202, 203]. For rock, the values $\alpha \simeq 2\times 10^{-3}$ GeV cm^2/g and $\beta \simeq 3\times 10^{-6}$ cm^2/g, are typical for muons with initial energy $\sim 10^2 - 10^3$ GeV. In finding the average range of the muons in the rock, generally the Eq. (4.28) is not strictly applicable because of stochastic energy losses [202, 204]. However, for our purposes, using a constant β and approximating

$$\frac{dE}{dz} \simeq \langle \frac{dE}{dz} \rangle \tag{4.29}$$

is sufficient. With this assumption the initial energy at $z = 0$, E_μ^i, is related to the final energy E_μ^f after traveling a distance z by

$$E_\mu^i(z) = e^{\beta\rho z} E_\mu^f + (e^{\beta\rho z} - 1)\frac{\alpha}{\beta} \ . \tag{4.30}$$

At low energies, for $E_\mu \leq 200$ GeV, the contribution from β term is small (about $10 - 20\%$) and in this energy range,

$$E_\mu^i(z) \simeq E_\mu^f + \alpha\rho z \ . \tag{4.31}$$

Muons with energies of a few 100 GeV are stopped in the rock ($\rho \simeq 2.6$g/cm^3) before they decay. As an example, the stopping distance for 500 GeV muons is roughly 1 km whereas the decay length, $\gamma c\tau$, for these muons turns out to be about 3000 km. For 50 GeV muons, the decay length is about 300 km, compared to a stopping distance of 100 m. The decay length information can still be included in the calculation by

introducing the survival probability as the solution to the equation,

$$\frac{dP_{\rm surv}}{dE_\mu} = \frac{P_{\rm surv}}{\gamma c\tau\rho(\alpha+\beta E_\mu)} \ . \tag{4.32}$$

This leads us to the survival probability for a muon with initial energy E_μ^i and final energy E_μ^f,

$$P_{\rm surv}(E_\mu^i, E_\mu^f) = \left(\frac{E_\mu^f}{E_\mu^i}\right)^\Gamma \left(\frac{\alpha+\beta E_\mu^i}{\alpha+\beta E_\mu^f}\right)^\Gamma \tag{4.33}$$

where $\Gamma \equiv m_\mu/(c\tau\alpha\rho)$.

With a distinction made between the energy of the muon when it is produced and the energy of the muon when it arrives at the detector, the formula for the upward muon flux becomes

$$\begin{aligned} \frac{d\phi_\mu}{dE_\mu} &= \int_0^{R_\mu} dz \int_{E_\mu^i}^{E_m} dE_\nu \frac{dP_{CC}}{dz\, dE_\mu^i} \frac{d\phi_\nu}{dE_\nu} P_{\rm surv}(E_\mu^i, E_\mu) \frac{dE_\mu^i}{dE_\mu} \\ &+ (\nu \to \bar{\nu}) \end{aligned} \tag{4.34}$$

where $E_\mu \equiv E_\mu^f$. However, only muons produced near the detector ($\sim$ a few kilometers away from the detector) will have sufficient energies to make it to the detector with an energy above the detector threshold energy E_{th}, i.e., $E_\mu \geq E_{th}$. Here, dP_{CC} is the probability for a neutrino with energy E_ν to be converted into a muon within the energy interval of dE_μ^i and over a distance dz in the rock, i.e

$$dP_{CC} = dz dE_\mu^i \frac{N_A\rho}{2} \left(\frac{d\sigma_\nu^p(E_\nu, E_\mu^i)}{dE_\mu^i} + (p \to n)\right). \tag{4.35}$$

The muon range is

$$R_\mu(E_\mu^i, E_\mu) = \frac{1}{\beta\rho} \ln\left(\frac{\alpha+\beta E_\mu^i}{\alpha+\beta E_\mu}\right) \tag{4.36}$$

following from Eq. (4.30). In Fig. 4.3, the muon range in the rock as a function of the initial muon energy is presented for different choices of final muon energies. We observe that for an initial muon energy of 1 TeV, the muon range is about 1 km.

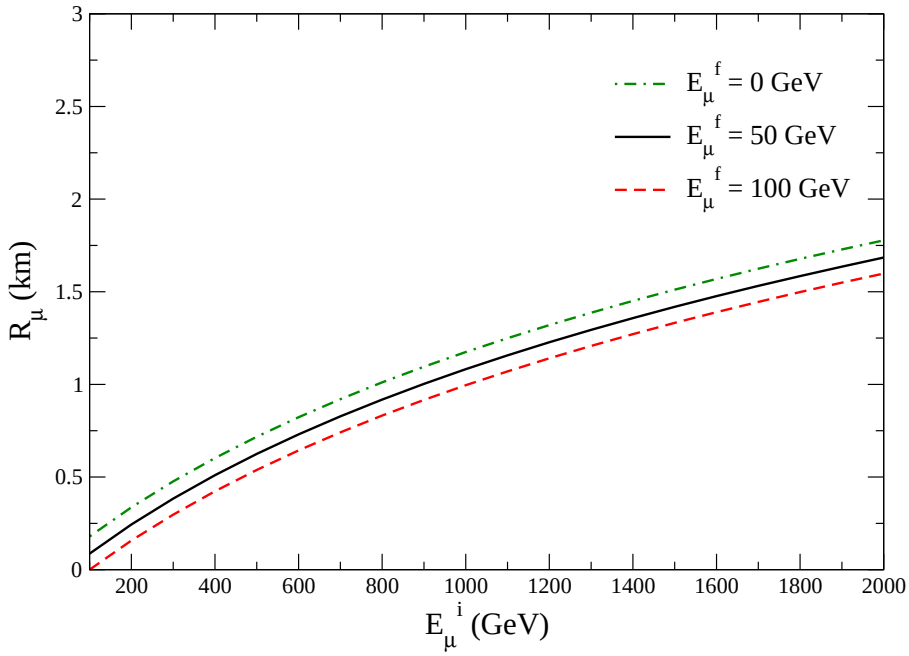

Figure 4.3: Muon Range as a function of the initial muon energy, E_μ^i for a given final muon energy of $E_\mu^f = 0$ GeV (dot-dashed line), 50 GeV (solid line), 100 GeV (dashed line).

4.3.2 Shower Events

In addition to muons, the showers produced in neutrino CC and NC interactions could be used as signals of DM. The shower flux is given by [190]

$$\begin{aligned} \frac{d\phi_{sh}}{dE_{sh}} &= \int_{E_{sh}}^{E_m} dE_\nu \left(\frac{d\phi_\nu}{dE_\nu}\right) \frac{N_A \rho}{2} \left(\frac{d\sigma_\nu^p(E_\nu, E_\nu - E_{sh})}{dE_{sh}} + (p \to n)\right) \\ &+ (\nu \to \bar{\nu}). \end{aligned} \tag{4.37}$$

4.3.3 Event Rates and Experimental Detection

The contained muon event rate, N_μ^{ct}, is obtained by integrating muon flux folded with the effective volume of the detector, V_{eff}, i.e.

$$N_\mu^{ct} = \int_{E_\mu^{th}}^{E_m} \frac{d\phi_\mu^{ct}}{dE_\mu} V_{\text{eff}}(E_\mu) dE_\mu \ , \tag{4.38}$$

where $d\phi_\mu^{ct}/dE_\mu$ is given in Eq. (4.25) and E_μ^{th} is the muon detector threshold, typically 10-100 GeV for deep ice or water detectors [67]. In most of the applications, we consider an energy independent IceCube+DeepCore effective volume, $V_{\rm eff} = 0.04$ km^3, for the contained muon events [62, 88].

Similarly, the upward muon event rate, is obtained by

$$N_\mu^{up} = \int_{E_\mu^{th}}^{E_{max}} \frac{d\phi_\mu^{up}}{dE_\mu} A_{\rm eff}(E_\mu) dE_\mu \ , \tag{4.39}$$

where $d\phi_\mu^{up}/dE_\mu$ is given by Eq. (4.34), $\langle A_{\rm eff}\rangle$ is the angle-averaged muon effective area. The Monte Carlo simulations show that the effective area of the IceCube detector increases with the final muon energy with which the muon reaches the detector [205, 206]. From the simulations, the angle-averaged energy dependent muon effective area, $\langle A_{\rm eff}\rangle$ is parametrized by $\langle A_{\rm eff}\rangle = 1.14 A_0(E_\mu)$ [205] where

$$\begin{aligned} A_0(E_\mu) &= 0 \quad \text{if} \ \ E_\mu \le E_1 = 10^{1.6} \text{ GeV} \\ A_0(E_\mu) &= 0.748(\log_{10}(E_\mu/\text{GeV}) - 1.6) \text{ km}^2 \\ &\quad \text{if} \ \ E_1 \le E_\mu \le E_2 = 10^{2.8} \text{ GeV} \\ A_0(E_\mu) &= 0.9 + 0.54(\log_{10}(E_\mu/\text{GeV}) - 2.8) \text{ km}^2 \\ &\quad \text{if} \ \ E_\mu > E_2 \ , \end{aligned} \tag{4.40}$$

for the IceCube detector.

The shower rates can also be evaluated by integrating Eq. (4.37) over the shower energies

$$N_{sh} = \int_{E_{sh}^{th}}^{E_m} \frac{d\phi_{sh}}{dE_{sh}} V_{\rm eff} dE_{sh}, \tag{4.41}$$

where $V_{\rm eff}$ is the effective volume of the detector for measuring showers. In most of the applications, for the detector volume, $V_{\rm eff}$, we use an energy independent IceCube+DeepCore volume whose value is $V_{\rm eff} = 0.02$ km^3 for the showers [62, 88, 149].

For each type of signal topologies in the detector, the total number of events (N_s) can be evaluated by multiplying the event rates with the observation time. The number of events due to atmospheric neutrinos (N_b) can also be calculated in a

similar way. Even if there is a significant signal to background ratio, low statistics may yield difficulties in confirming the presence of a DM signal. Thus, we make use of the statistical factor

$$S = \frac{N_s}{\sqrt{(N_s + N_b)}} \, , \tag{4.42}$$

defined as the detection significance. As an example, by 2σ detection significance we mean

$$\frac{N_s}{\sqrt{(N_s + N_b)}} = 2 \, . \tag{4.43}$$

CHAPTER 5

CHARACTERISTICS OF DARK MATTER SIGNALS

In this chapter, we present our results for energy distributions and total counts of final muon and shower fluxes to be observed in the neutrino detectors due to DM annihilation in the Galaxy. We consider different annihilation channels of DM and also different signal topologies (upward muon events, contained muon events and shower events) and we study the potential discovery of DM in IceCube+DeepCore detector. We begin with presenting our results for the signals from DM annihilation in the GC.

5.1 Dark matter signal from the GC

As described in Chapter 2, independent of the DM density profile in the Galaxy, DM density is expected to be high in the GC. Since the neutrino signals from DM increase with DM density, the very first place to be searched for a potential discovery of DM is the GC. The direct production channel, $\chi\chi \rightarrow \nu_\mu \overline{\nu}_\mu$, where χ is the DM, is the most promising channel for the detection of DM annihilation in GC, assuming an adequate annihilation cross section. A typical example of a DM particle candidate which annihilates into a neutrino pair is the lightest Kaluza-Klein particle. However, some particle candidates, for example neutralinos and leptophilic DM, produce neutrinos only as secondary particles, via the decay of the particles into which the DM particles annihilate, such as $\mu^+\mu^-$, $\tau^+\tau^-$, $b\bar{b}$, W^+W^-, etc.

In the first two figures, we present our results for the upward muon flux due to the annihilation of a DM particle via the direct production ($\chi\chi \rightarrow \nu_\mu \overline{\nu}_\mu$) channel. To illustrate various contributions, we choose the DM particle mass m_χ =500 GeV, in Fig. 5.1, the NFW DM density profile [92] and the boost factor B =200 which is in the range of the boost factor values that explain the PAMELA data [47, 130]. In

Fig. 5.2, the DM density profile is the cored isothermal profile and we use a boost factor $B = 800$ to match the normalization of the NFW density profile. We show our results for two different choices of the cone half angle (5° and 10°) and compare them with the angle-averaged background due to the atmospheric neutrinos.

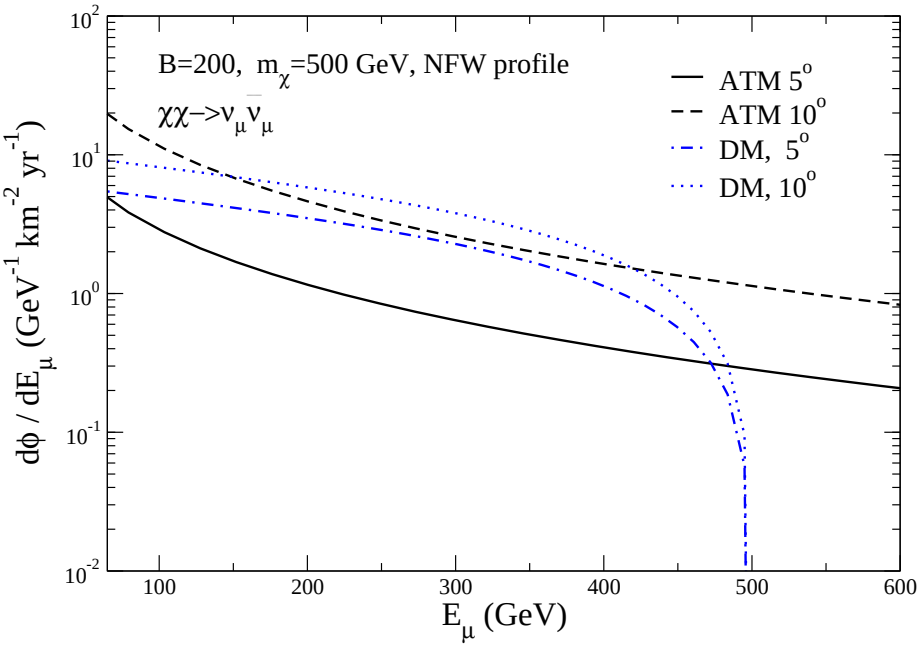

Figure 5.1: Upward muon flux obtained from DM annihilation into neutrinos in the Galactic Center, for a cone half angle (θ) of 5° (dot-dashed) and 10° (dotted). The background upward muon fluxes due to (angle-averaged) atmospheric neutrinos are shown with the solid (for $\theta = 5°$) and the dashed (for $\theta = 10°$) curves. The NFW DM profile is used, along with a boost factor $B = 200$ and $m_\chi = 500$ GeV.

For a 10° cone half angle, the signal dominates over the background in the range 180 GeV$< E_\mu <$420 GeV for the NFW profile. We note that the background signal is suppressed more than the DM signal with the decrease in the cone half angle. As a comparison, for a 5° cone half angle the signal exceeds the background in a wider range of energies, 60 GeV$< E_\mu <$480 GeV.

From Fig. 5.2, we note that in case of the isothermal profile for the DM in which

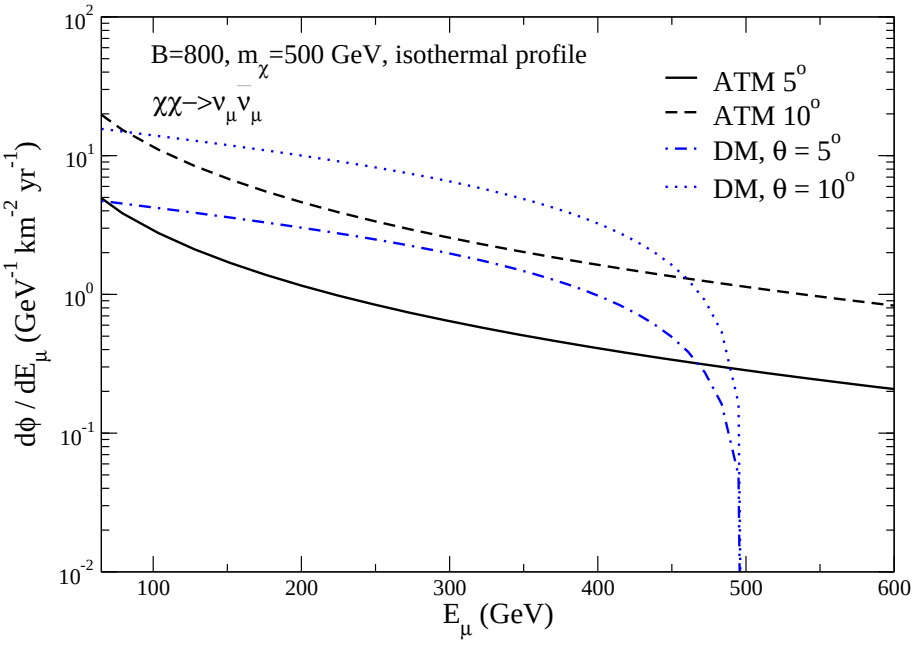

Figure 5.2: Same as Fig. 1 but for the cored isothermal dark matter density profile and a boost factor $B = 800$.

there is a relatively less dense core region, by increasing the cone half angle from 5° to 10°, there is an almost equal enhancement of the upward muon fluxes from the atmospheric neutrino background and from the DM annihilation in the center of the Galaxy. For the set of the parameters that we choose here, the DM signal becomes larger than the background in the energy ranges of 100 GeV$< E_\mu <$470 GeV and 70 GeV$< E_\mu <$480 GeV for the cone half angles 10° and 5°, respectively.

Fig. 5.3 shows the dependence of the muon fluxes from DM annihilation via the direct production channel for $m_\chi = 200,\ 500$ and 800 GeV. We consider the NFW profile, a fixed boost factor ($B = 200$) and a fixed cone half angle ($\theta_{\rm max} = 5°$). The figure shows the upward muon flux as well as the contained muon flux assuming a detector size $D = 1$ km [1]. We find that regardless of the mass dependence, the

[1]We calculate the contained muon fluxes by multiplying Eq. (4.25) with a detector size of D =1 km, in order to be able to compare the signal levels with those from upward muon fluxes which

upward muon event flux is a decreasing function of the muon energy whereas the corresponding flux of the contained muon events increases with the muon energy up to the cut-off set by the initial neutrino energy. In our calculations, we assume that the DM particles annihilate at rest and thus the neutrino energy for this decay mode can be set to the rest mass of the DM particle, $E_\mu = m_\chi$.

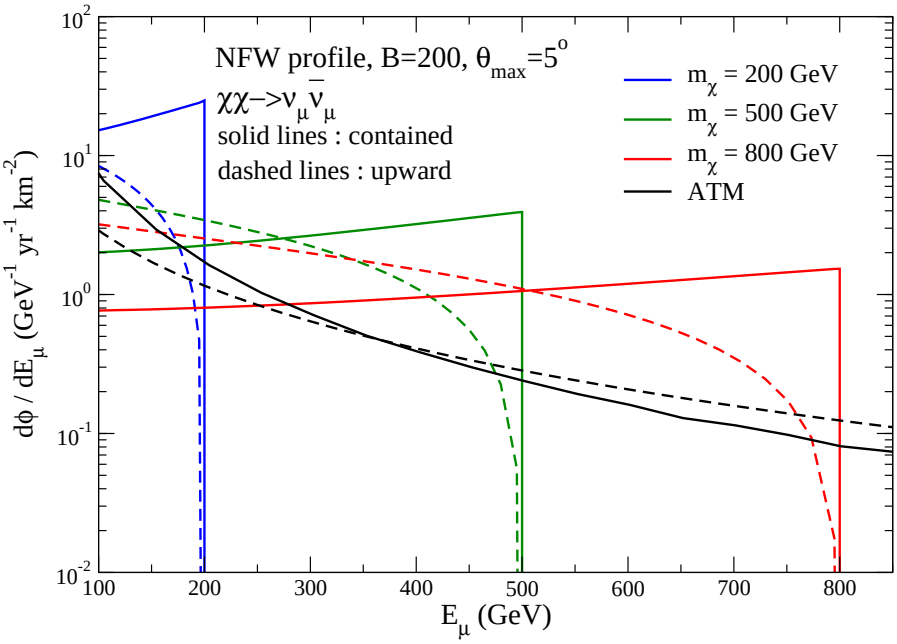

Figure 5.3: Muon flux due to the dark matter annihilation into neutrinos in the Galactic center for different dark matter masses, curves correspond to the dark matter masses of 200 GeV, 500 GeV and 800 GeV, respectively. The corresponding backgrounds are also shown. All the solid lines correspond to the contained muon events with $D = 1$ km, whereas the dashed ones to upward muon events.

The signal for the muon flux from the contained muon events has a stronger suppression with the increase in the DM mass than for the upward muon events. This is due to the m_χ^{-2} dependence in Eq. (4.4). The mass dependence for upward events is more complex because of the mass dependence in the upper limit of the z

are given per area.

integration in Eq. (4.34). A large mass m_χ (and therefore higher E_ν) produces a higher energy muon which has a longer range in the rock below the detector. For example, for $E_\mu > 380$ GeV, the upward muon signal from the annihilation of the DM particle with mass $m_\chi = 800$ GeV dominates over the one from that of the DM particle with mass $m_\chi = 500$ GeV.

For a wide range of muon energies, the DM signal is above the atmospheric background both for contained and upward muon events in the $\chi\chi \to \nu_\mu \overline{\nu}_\mu$ channel with the boost factor used here. We find that for a given DM mass the contained muon events exceed the upward ones in the range $E_\mu \geq 0.6 m_\chi$.

In Fig. 5.4, we present our results for the muon flux due to $\chi\chi \to \tau^+\tau^-$ channel. This channel is characteristic of all three-body decays into neutrinos (secondary neutrinos). Again shown are the upward and contained muon signals from $m_\chi = 200,\ 500$ and 800 GeV with the NFW profile and $B = 200$.

Note that in the case of secondary neutrinos, the signal for both upward and contained muon events decrease as the muon energy increases, and for a fixed m_χ, the contained muon events, in general, dominate over the upward muon events for muon energies $100\text{GeV} \leq E_\mu \leq m_\chi$. This is a consequence of considering a detector size of $D = 1$ km, a size larger than the range of a muon with an energy of less than 1 TeV. The figure shows that even for a half angle of 5°, in case of NFW profile one would need a boost factor on the order of about 2000 for the DM signals from the secondary neutrinos to be above the atmospheric background.

Measurements of the muon flux can also be used to distinguish different DM models, as seen in Fig. 5.5 where we compare signals from different annihilation channels: $\chi\chi \to W^+W^-$, $\chi\chi \to \tau^+\tau^-$ and $\chi\chi \to b\overline{b}$ for the NFW profile, with $B = 200$, the cone half angle equal 5° and $m_\chi = 500$ GeV. The signals from the b-quark and the tau decay modes differ only by an overall factor which is close to the ratio of the decay branching fractions of the corresponding modes. However, for the W decay, being a two-body decay, the shape of the muon flux is quite different than those of the b-quark and tau which are both three-body decay modes. This indicates that muon flux from the secondary neutrinos as a by-product of the DM

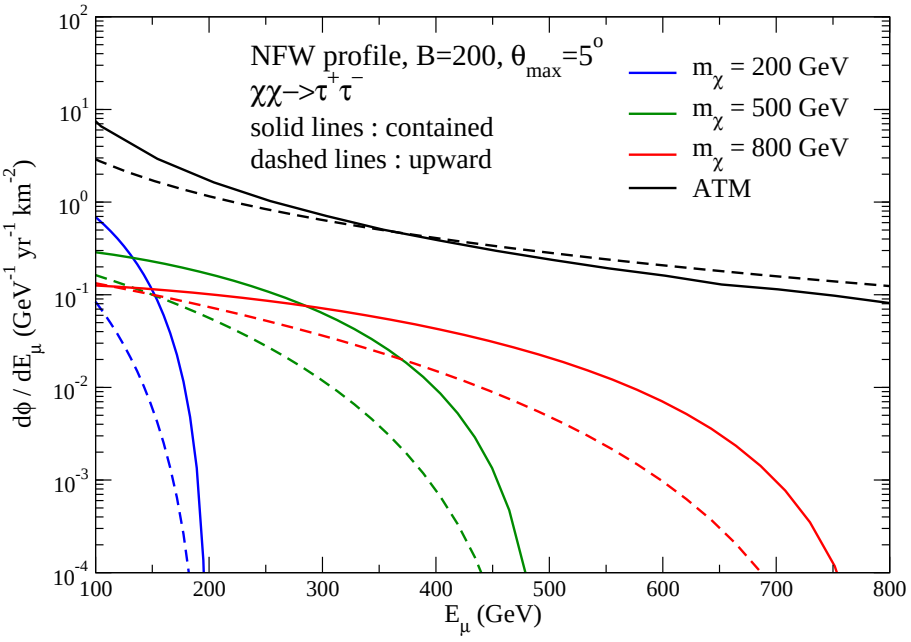

Figure 5.4: Muon fluxes due to the secondary neutrinos produced through the dark matter annihilation into tau particles in the Galactic center for different dark matter masses; $m_\chi = 200, 500$ and 800 GeV. The solid (dashed) curves correspond to contained (upward) muon events.

annihilation can also be useful in discriminating different DM models.

We now turn to the event rate per area of upward and contained muons produced by $\nu_\mu + \bar{\nu}_\mu$ from direct DM annihilation to neutrinos. Integrating the fluxes over the final muon energy, we obtain the muon rate from the annihilation of the DM as a function of the mass m_χ (Fig. 5.6) for the NFW profile with $B = 200$ and $\theta_{\rm max} = 5°$. Here, the threshold energy is taken to be $E_{th} = 80$ GeV. Due to the finite size of the detector ($D = 1$ km), and m_χ^{-2} dependence of the annihilation rate, the signal for the contained muon events decreases with increasing the DM mass. On the other hand for upward muon events, heavier DM particles yield more energetic neutrinos which makes a larger portion of muons in the rock below the detector to contribute to the final muon flux. This effect combined with the energy dependence of the

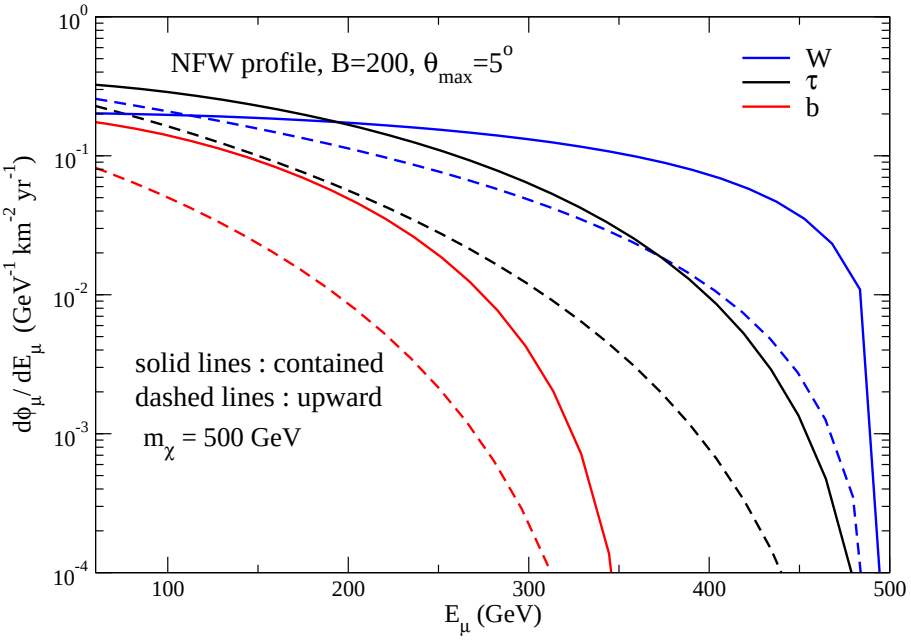

Figure 5.5: Muon fluxes due to the secondary neutrinos produced through the dark matter annihilation into W bosons, tau particles, and bottom quarks in the Galactic Center. The solid (dashed) lines for each channel correspond to contained (upward) events. The detector size is taken to be $D = 1$ km, and the cone half angle is $\theta = 5^\circ$ for the NFW profile with $B = 200$.

neutrino CC cross section, results in increasing muon rate up to $m_\chi = 650$ GeV, at which point the m_χ^{-2} dependence of the annihilation rate takes over resulting in slow decrease of the muon rate. A comparison of the contained and upward muon rates presented in Fig. 5.6 indicates that for $m_\chi \leq 500$ GeV the signal from the contained muon events still dominates over the signal from the upward muon events. Even though the signal depends weakly on the value of the threshold energy, the background is very sensitive to it due to the large contribution from the low energy atmospheric neutrinos. The signal to background ratio increases with increasing the muon energy threshold. We obtain the same results for the isothermal DM density halo profile if the boost factor is taken to be 800 for the same cone half angle of 5°.

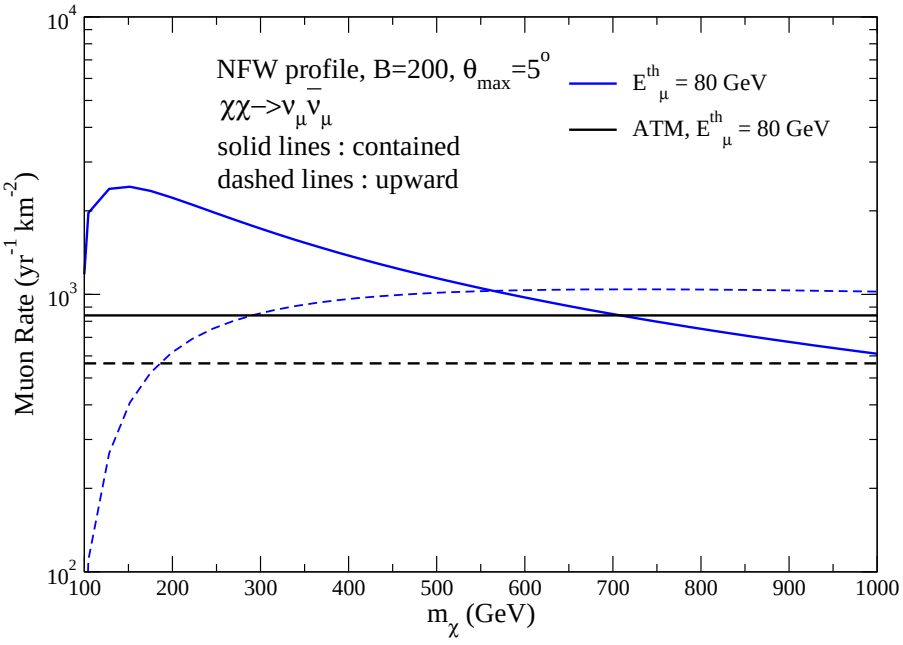

Figure 5.6: Muon rates due to the dark matter annihilation into neutrinos in the Galactic center. The solid (dashed) lines correspond to contained (upward) muon events. We take cone half angle, $\theta_{\rm max}$, to be 5°.

In Fig. 5.7 we also show our results for the 10° cone half angle. We note that in case of contained muon events the signal dominates over the background for 100 GeV $\leq m_\chi \leq$ 200 GeV, when the threshold energy is 80 GeV. For upward muon events, signal is below the background for all m_χ. The isothermal DM density halo profile gives larger signal than obtained with the NFW profile by about a factor of 2, due to its larger increase of $\langle J_2 \rangle_\Omega$ for 10° relative to 5°.

In Fig. 5.8 we show contour plots for upward muon events, $N_\mu = (0.5, 5, 50, 500, 850)$ km^{-2}yr^{-1}. The solid (dashed) lines correspond to the muon energy threshold of 50 (80) GeV. We also calculate that $N_\mu = 714(516)$ km^{-2}yr^{-1} for the upward muon events due to the atmospheric muon neutrinos for the muon energy threshold of 50 (80) GeV. We find that for a fixed cone half angle the annihilation cross section does not depend on m_χ for $m_\chi > 200$ GeV to produce a given

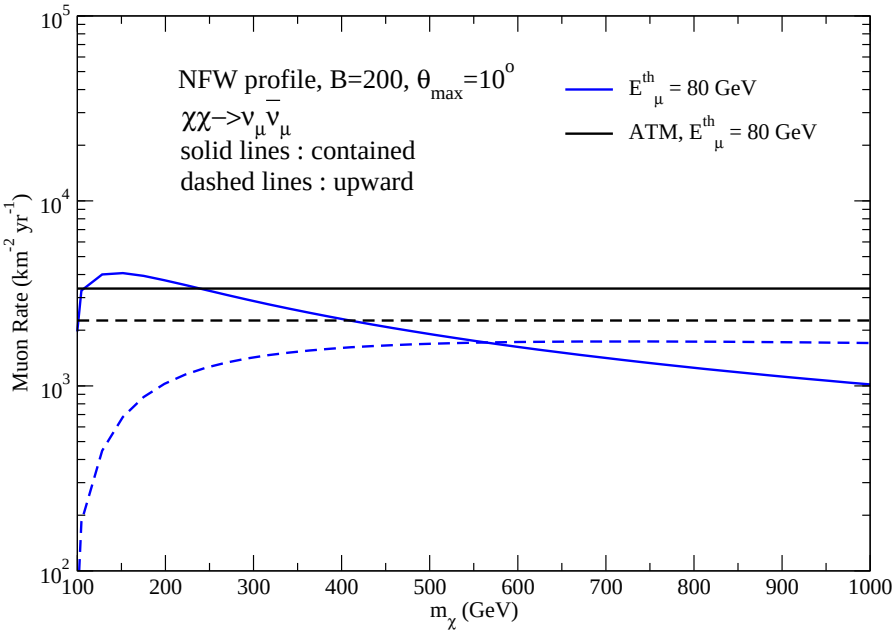

Figure 5.7: Same as Fig. 5.6 but for $\theta_{\rm max} = 10°$.

total muon flux since the decrease in the annihilation rate with m_χ is compensated with the increase in the muon range and neutrino cross section with m_χ. The dependence on the choice of the threshold is also negligible. However, for low mass DM particles, higher values of the annihilation cross sections are required in order to have the same total muon flux. This is due to the fact that the neutrinos originating from this low mass DM annihilation mostly contribute to the muon flux at energies less than the thresholds we choose. The parameter space above the dotted line is excluded at 90% C.L. by Super-Kamiokande observations toward the direction of the GC with a cone half angle of 5° [207].

The dominant atmospheric neutrino flavor at neutrino energies above 40 GeV is ν_μ which produces track-like events through CC interactions in the neutrino telescopes. Identifying track-like events could reduce the background substantially. Recently it has been argued that IceCube+DeepCore will be able to put constraints

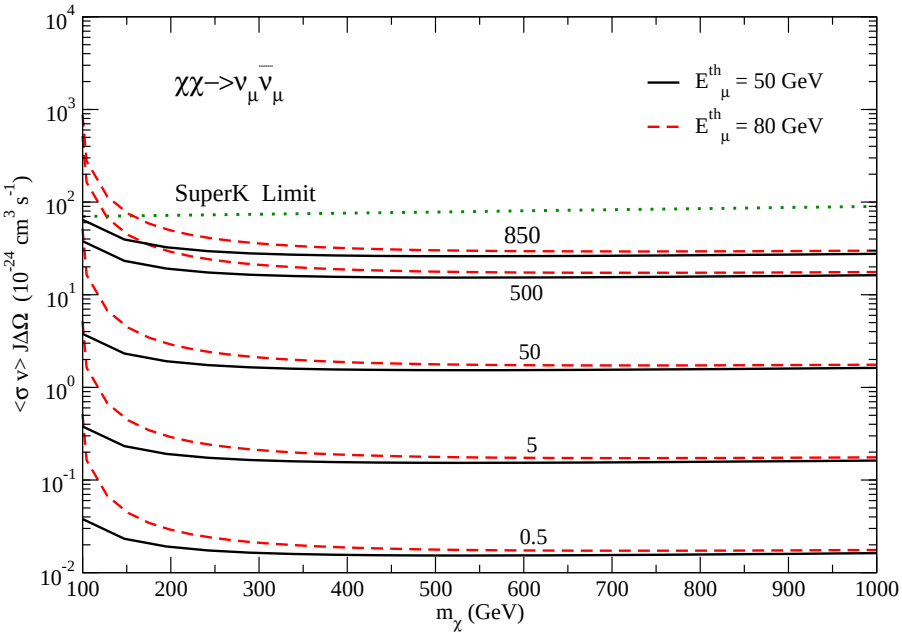

Figure 5.8: Upward muon events, contour plots which give $N_\mu = (0.5, 5, 50, 500, 850)\text{km}^{-2}\text{yr}^{-1}$, for a given $\langle\sigma v\rangle J\Delta\Omega$ versus m_χ. The energy threshold is set to be 50 GeV (solid lines) and 80 GeV (dashed lines) and the boost factor is set to be unity and the cone half angle to be 5°.

on DM properties in a more efficient way by just analyzing the cascade (i.e shower) events which are due to CC interactions of $\nu_{e,\tau}$ and the NC interactions of the all neutrino flavors [65]. Since the weak scattering cross sections are independent of the flavors, the signal to background ratio is enhanced in shower events since ν_μ can only contribute to the shower events through NC interactions where the cross section is about 1/3 of the CC cross section (Eq. 3.36).

In Fig. 5.9, we show hadronic shower rates as a function of m_χ from NC interaction of muon neutrinos and antineutrinos. These rates are the same for any other neutrino flavor with a democratic $\chi\chi \to \nu\bar{\nu}$ annihilation rate. Also shown is the hadronic shower rate due to the atmospheric muon neutrinos; $N_{sh}^{atm} = 168\ \text{km}^{-2}\text{yr}^{-1}$ for the NC interaction. The shower threshold is taken to be 100 GeV. We note that

the background due to the atmospheric electron and tau neutrinos is much smaller than for the muon neutrinos, so the signal to background would not change much here when the background signals from all neutrino flavors were included.

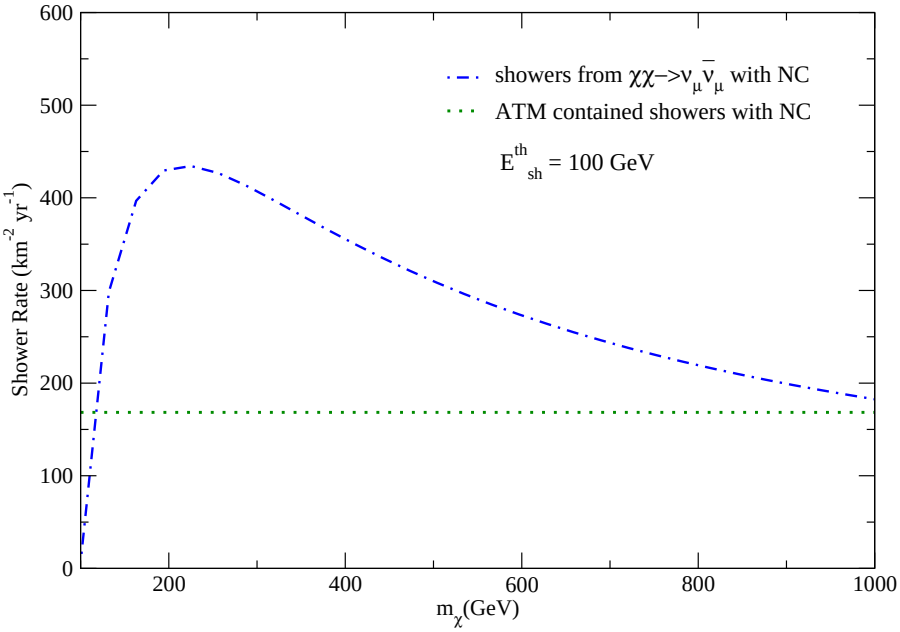

Figure 5.9: Hadronic shower rates for NC (dot-dashed) interactions of $\nu_\mu + \overline{\nu}_\mu$ when muon neutrinos are produced directly from the dark matter annihilation in the Galactic center. The NFW profile, with $B = 200$, $\theta = 5°$, $E_{sh}^{th} = 100$ GeV and $D = 1$ km are used.

We also evaluate the electromagnetic shower rate as a function of m_χ due to electrons produced by the CC interactions of ν_e, with an electromagnetic shower threshold set at 100 GeV. The atmospheric shower rate is evaluated using the atmospheric ν_e and $\overline{\nu}_e$ flux for an effective zenith angle $0.4 < \cos\theta_z < 0.5$, which roughly corresponds to the angle describing the position of the GC relative to the IceCube [71],

$$\left(\frac{d\phi}{dEd\Omega}\right)_{\nu_e} = \frac{500.0}{(\mathrm{GeV m^2 s\, sr})}\left(\frac{E}{\mathrm{GeV}}\right)^{-3.57}$$

$$\left(\frac{d\phi}{dEd\Omega}\right)_{\overline{\nu}_e} = \frac{382.6}{(\mathrm{GeV m^2 s\,sr})}\left(\frac{E}{\mathrm{GeV}}\right)^{-3.57}. \quad (5.1)$$

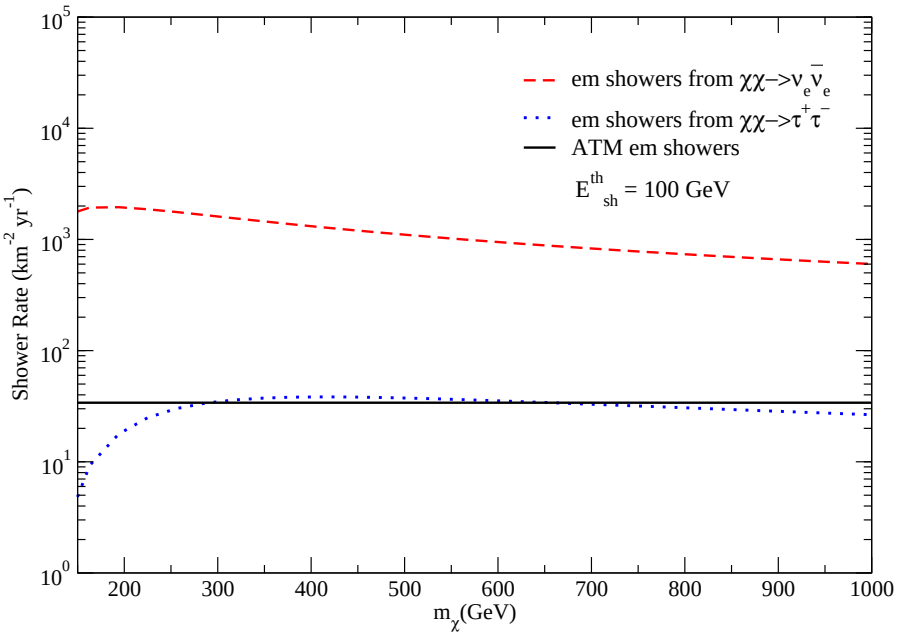

Figure 5.10: Electromagnetic shower rates as a function of m_χ for $\nu_e + \overline{\nu}_e$ CC interactions when electron neutrinos are produced directly in the annihilation of dark matter in the Galactic center. The NFW profile, with $B = 200$, $\theta = 5°$, $E^{th}_{sh} = 100$ GeV and $D = 1$ km are used.

In Fig. 5.10 we see that the signal to background ratio is increased for the electromagnetic showers relative to hadronic showers mainly due to a very small atmospheric electron neutrino flux which is about 34 $\mathrm{km^{-2}yr^{-1}}$. For secondary electron neutrinos from the decay of taus which are produced via $\chi\chi \to \tau^+\tau^-$, the signal becomes comparable to the background.

For the future neutrino detector which is positioned in the northern hemisphere, such as KM3Net, the relevant background would be coming from almost horizontal showers, which is about a factor of three to four times larger than the flux given by Eq. (5.1), giving approximately electromagnetic shower flux of 100 $\mathrm{km^{-2}yr^{-1}}$.

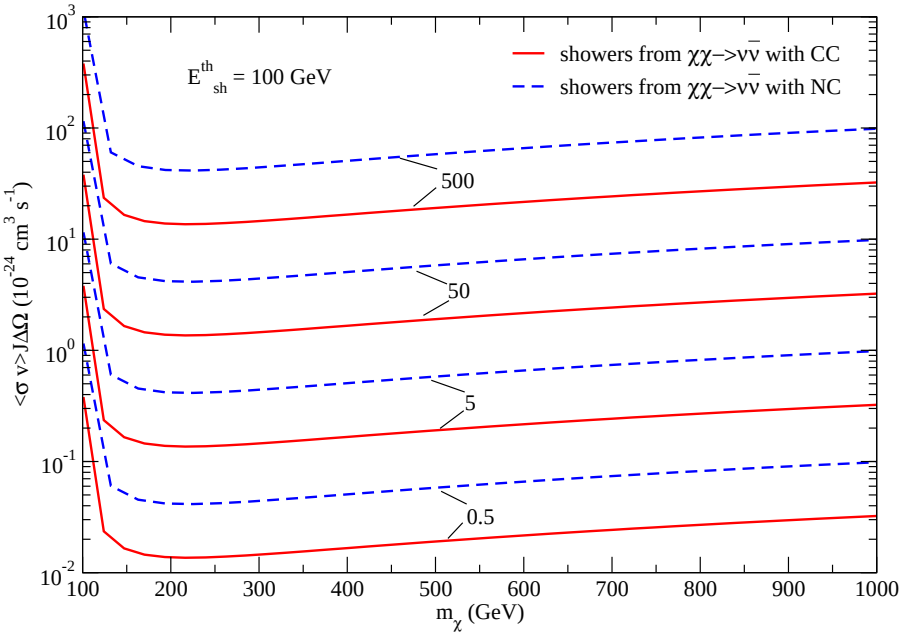

Figure 5.11: Hadronic shower event curves, $N_{sh}^{h} = (0.5, 5, 50, 500)\mathrm{km}^{-2}\mathrm{yr}^{-1}$, for the CC (solid) and NC (dashed) processes, for a NFW dark matter density profile, a 5° cone half angle, the boost factor set to be unity and $D = 1$ km.

In Figs. 5.11 and 5.12, we present the contour plots for showers with the energy threshold of 100 GeV. The main difference between the showers and the upward muons appears for $m_\chi > 200$ GeV where for a given total number of shower events higher annihilation cross sections is required with the increase in m_χ. This is due to the contained event nature of the shower events which are all produced inside the detector with finite size. Thus, in contrast to the case for the upward muon events that we discussed earlier, the strong suppression of the annihilation rate with m_χ can not be compensated because of the finite size of the detector. The CC showers actually require a smaller annihilation cross sections in order to produce the same number of total shower events that NC showers produce for a fixed m_χ due to the larger weak scattering cross sections.

The signal detection significance can be evaluated using Eq. (4.42). We obtain

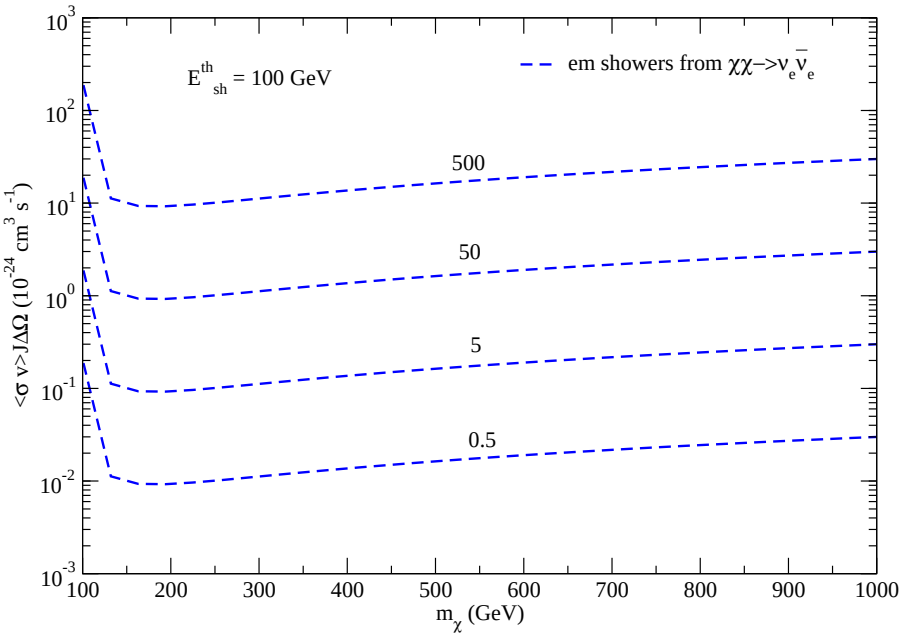

Figure 5.12: Same as Fig. 5.11 but for electromagnetic shower events.

the time it would take to observe a 5σ effect using our results for the contained muon events (Fig. 5.6), hadronic showers (Fig. 5.9) and electromagnetic showers (Fig. 5.10). In our calculations, we use the effective volume of IceCube+DeepCore for the track-like (shower) events, i.e $V_{\rm eff} = 0.04(0.02)$ km^3. In Fig. 5.13, we show the observation time (t) required for IceCube+DeepCore detector to detect or exclude the DM signal via the direct production channel at a 5σ level. Here, we again use fixed boost factor ($B = 200$) and cone half angle ($\theta_{\rm max} = 5^\circ$). Our results, when we take $B_F = 1$ for the direct production channel, suggest that in less than two years of observation IceCube+DeepCore will be able to reach a 5σ detection for the contained muon and electromagnetic shower events for a wide range of m_χ. Decreasing the branching fraction by an order of magnitude increases the observation time significantly in order to reach the same significance. For instance, $t \simeq 10 - 50$ years, for 150GeV $\leq m_\chi \leq$ 500GeV in the case of contained muon events, and

somewhat shorter for the electromagnetic showers.

In the case of secondary neutrino production, when neutrinos are produced from tau decays, and taus are products of DM annihilation, these neutrinos can interact inside the detector producing hadronic and electromagnetic showers, in addition to muon neutrinos producing muons via CC interactions. In Fig. 5.14, we show that IceCube+DeepCore detector could potentially detect a 2σ effect in 5 (8) years for $m_\chi = 300$ GeV (1TeV), in case of excluding muon-like events. To reach a 2σ detection for the electromagnetic showers due to the secondary electron neutrinos IceCube+DeepCore will need about $10 - 20$ years of observation for 250 GeV $\leq m_\chi \leq 1$ TeV. When muon-like events are included, the observation times for the hadronic showers become similar to those for the electromagnetic showers. The time needed for a 5σ effect for hadronic (electromagnetic) showers is almost an order of magnitude longer than for a 2σ effect.

Comparing the secondary and direct production (Figs. 5.13 and 5.14) one sees that it takes longer (by about one order of magnitude) to detect showers from secondary neutrinos that to detect showers from primary neutrinos. This is because of the different shape of the shower energy distributions: for direct neutrinos it increases with energy and for secondary neutrinos it decreases with energy.

Since the angular resolution for showers is expected to be much worse than for muons, for the angular resolution of 30°, the number of signal events will be larger by a factor of 6, while the background will increase by a factor of 35, which results in reducing the time it would take IceCube+DeepCore to see a 2σ effect to 3 years for hadronic showers. This is in qualitative agreement with the results presented in Ref. [62].

For DM models in which neutrinos are decay products of taus produced in the DM annihilation, looking for contained hadronic showers in IceCube+DeepCore seems promising to detect a signal at the 2 σ level, assuming the NFW DM density profile and a boost factor $B = 200$.

In Table (5.1) we give a summary of our results for the event rates for various DM masses. We consider the direct production of neutrinos ($\chi\chi \to \nu\overline{\nu}$) and the neutrinos

Table 5.1: Event rates per km^2 per yr for the contained (ct), upward (u) muons (μ) and for the showers (sh) produced via CC, NC and electromagnetic (em) interactions. Neutrinos from direct production ($\chi\chi \to \nu\overline{\nu}$) channel and secondary neutrinos from $\chi\chi \to \tau^+\tau^-$ channel are considered. We have set $B \cdot B_F = 200$ for each channel. The cone half angle is chosen to be 5° and 10°. The threshold energy for the muon (shower) events is set to be 80 (100) GeV. The backgrounds due to atmospheric neutrinos are also presented.

	m_χ (GeV)								
	200	300	400	500	600	700	800	900	1000
$\chi\chi \to \nu\overline{\nu}$									
$N^{\mu}_{ct}(5°)$	2240	1750	1385	1135	976	850	750	670	611
$N^{\mu}_{ct}(10°)$	3808	2975	2355	1930	1659	1445	1275	1139	1039
$N^{\mu}_{up}(5°)$	615	850	960	1010	1035	1042	1040	1033	1023
$N^{\mu}_{up}(10°)$	1046	1445	1632	1717	1760	1771	1768	1756	1739
$N^{NC}_{sh}(5°)$	430	400	355	310	274	240	220	200	182
$N^{NC}_{sh}(10°)$	731	680	604	527	466	408	374	340	309
$N^{CC}_{sh}(5°)$	1310	1230	1080	935	830	741	665	605	556
$N^{CC}_{sh}(10°)$	2227	2091	1836	1590	1411	1260	1131	1029	945
$N^{em}_{sh}(5°)$	1920	1600	1300	1100	950	820	730	660	600
$N^{em}_{sh}(10°)$	3264	2720	2210	1870	1615	1394	1241	1122	1020
$\chi\chi \to \tau^+\tau^-$									
$N^{NC}_{sh}(5°)$	17	28	33	33	32	31	28	27	24
$N^{NC}_{sh}(10°)$	29	48	56	56	54	53	48	46	41
$N^{CC}_{sh}(5°)$	39	66	73	72	70	66	61	58	55
$N^{CC}_{sh}(10°)$	66	112	124	122	119	112	104	99	94
$N^{em}_{sh}(5°)$	20	34	38	37	35	33	31	29	27
$N^{em}_{sh}(10°)$	34	58	65	63	60	56	53	49	46
ATM^{μ}_{ct}	839 (5°)					3356 (10°)			
ATM^{μ}_{up}	564 (5°)					2256 (10°)			
ATM^{NC}_{sh}	169 (5°)					676 (10°)			
ATM^{CC}_{sh}	523 (5°)					2092 (10°)			
ATM^{em}_{sh}	34 (5°)					136 (10°)			

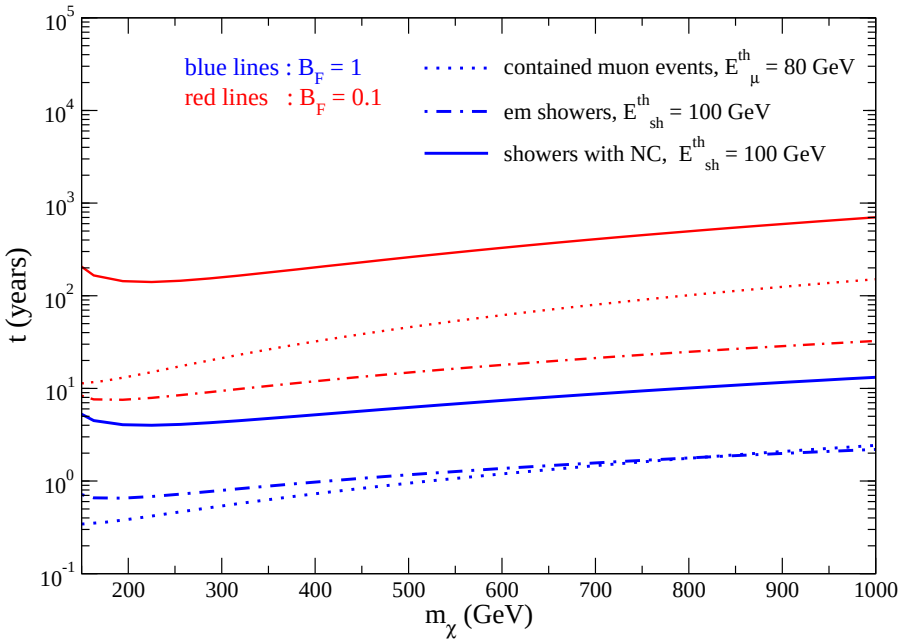

Figure 5.13: Time as a function of dark matter mass, m_χ, for the direct neutrino production channel ($\chi\chi \to \nu\bar{\nu}$) to reach a 5σ detection level for IceCube+DeepCore detector. The curves correspond to hadronic showers (solid lines), electromagnetic showers (dotted lines) and the contained muon events (dot-dashed lines). $B_F = 1(0.1)$ for the lower (upper) curves, the boost factor is taken to be 200 and the cone half angle is 5° for all curves.

from the tau decay ($\chi\chi \to \tau^+\tau^- \to l^+l^-\nu_\tau\bar{\nu}_\tau\nu_l\bar{\nu}_l$). We classify the event rates as contained (ct) and upward (up) for the track-like muon (μ) events, and depending on the type of the interaction involved CC, NC and electromagnetic (em) for the shower events. Two different cone half angles are chosen, $\theta = 5^\circ$ and $\theta = 10^\circ$, and the threshold energy for the track-like muon (shower) events are set to be 80 (100) GeV. We also show the atmospheric neutrino background for the track-like muon and for the shower events.

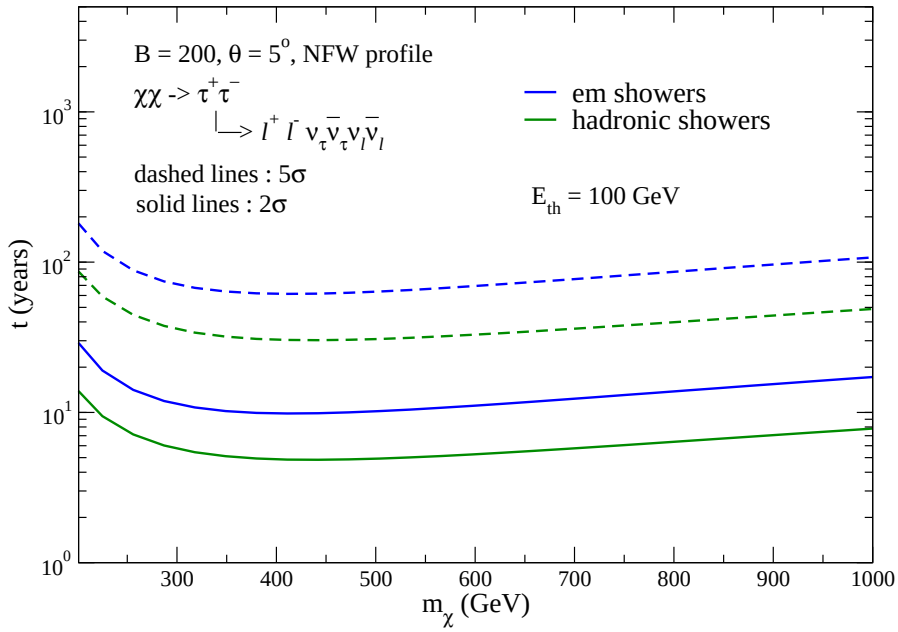

Figure 5.14: Time as a function of dark matter mass, m_χ, for the secondary neutrino production channel $\chi\chi \to \tau^+\tau^- \to l^+l^-\nu_\tau\bar{\nu}_\tau\nu_l\bar{\nu}_l$ to reach a 2σ (solid curves) or a 5σ (dashed curves) detection level when measuring electromagnetic showers (top curves) and hadronic showers (lower curves).

5.2 Dark Matter Signal from the Core of the Earth/Sun

To illustrate the muon flux's dependence on muon energy, we begin with DM annihilation in the Earth's core. In addition to making a choice for m_χ, one must also make some assumptions about the DM-nucleon cross section and main channel to produce neutrinos. For all of the figures for DM annihilation, we use $\sigma_0^i \simeq 10^{-8} N_i^4$ pb [53, 106] and the standard composition of the Earth as reviewed in Ref. [187].

The upper curves in Fig. 5.15 show our results for $\chi\chi \to \nu_\mu\bar{\nu}_\mu$ with $B_{\nu_\mu} = 1$, for upward events (dot-dashed line) and contained events (dashed line) for $m_\chi = 500$ GeV. The lower dot-dot-dashed and dot-dash-dashed lines in Fig. 5.15 come from $\chi\chi \to \tau^+\tau^-$ with $B_\tau = 1$, followed by $\tau \to \nu_\tau\mu\bar{\nu}_\mu$ according to the energy

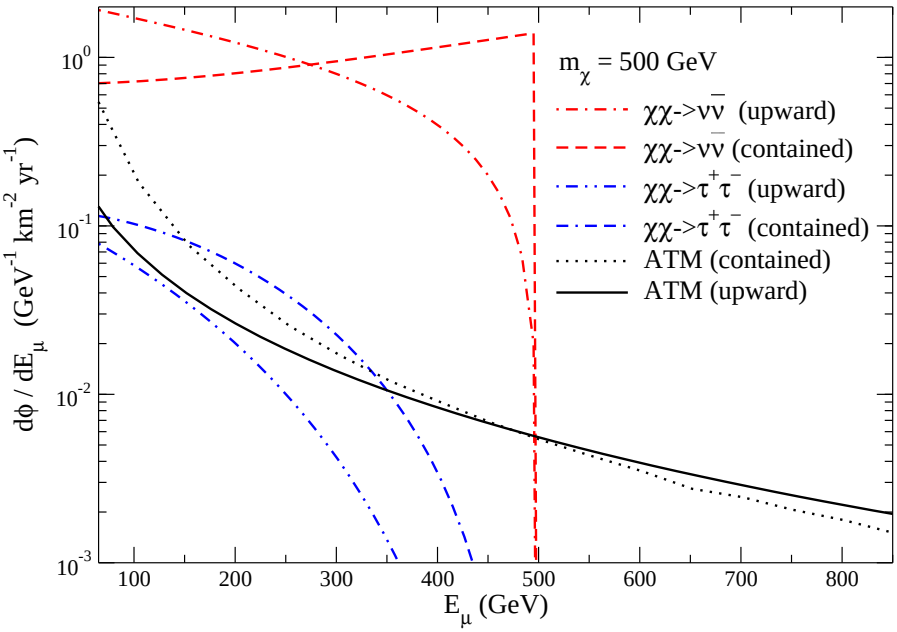

Figure 5.15: Muon flux obtained from dark matter annihilation into neutrinos in the core of the Earth, when muons are created in neutrino interactions with nucleons in the rock below the detector (dot-dashed and dot-dot-dashed curves), when muons are created in the detector, i.e. contained events (dashed and dot-dash-dashed curves). The upper curves are for the direct production of neutrinos, while the lower curves are for neutrinos from tau decays. The background from contained atmospheric neutrinos, evaluated for a cone half angle $\theta_{\rm max} = 1^\circ$ are shown with the dotted line and the upward muon flux from atmospheric neutrinos is shown by the solid line.

distribution given in Chapter 3. We choose the tau channel as representative of the three body decays.

As before, for direct production of neutrinos, $d\phi_\nu/dE_\nu \propto \delta(m_\chi - E_\nu)$. The cross section for neutrino production of muons smears the distribution. For contained events, one sees the smeared distribution directly in Fig. 5.15. Upward events have the additional energy redistribution from muon energy loss in transit that shifts the muon energy distribution to lower energies, enhancing the lower energy flux relative to the contained flux, despite the fact that the range is shorter than $\ell = 1$ km. In the cascade of $\tau \rightarrow \nu_\mu \rightarrow \mu$, shown with the lower curves, there is never a high energy peak and the upward events are always below the contained events for this value of m_χ. Only for m_χ sufficiently higher than 1 TeV could the upward events be enhanced relative to the contained events.

As an indication of the atmospheric neutrino background, we also show upward (solid line) and contained events (dotted line) from a solid angle defined by a cone half angle 1° around the upward vertical direction. The approximate angular resolution of the IceCube detector is $\theta = 1°$, however, DM annihilation can occur at angles larger than 1°. In particular, for a 500 GeV neutralino, it has been shown [57] that most of the annihilation occurs within an angle of $\theta \sim 2.7°$. With this larger nadir angle, the solid angle for the atmospheric background is increased by a factor of ~ 8. The shape of the background atmospheric flux is very different from the signal of contained events for direct annihilation of DM into neutrinos. With the atmospheric contained events in the figure multiplied by a factor of 8, the contained event rate would dominate the background only for the high energy peak. Our sample calculation is for $B_\nu \sigma_0^i = 10^{-8} N_i^4$ pb^{-1}, in which the capture and annihilation rates are in equilibrium (Eq. 4.12). For the secondary neutrino production, from τ decay, one needs $B_\tau \sigma_i^0 \sim 10^{-7} N_i^4$ pb^{-1} for this channel to be comparable to the background. Clearly measurements of the shape of the muon flux, both contained and upward, would be useful in searching for the DM signal.

These values of the cross section σ_0^i required for signals on the order of the atmospheric background are sufficient for the condition for the equilibrium between

capture and annihilation in the Earth's core to be satisfied. Even though only with significant enhancements of the capture rate (i.e. DM-nucleon cross section) or DM annihilation rate, the Earth might be a source of measurable rates for DM annihilation to neutrinos, it is a useful demonstration of the energy dependence of the muon flux.

The energy dependence of Fig. 5.15 is at odds with the muon energy dependence sometimes found in the literature [53]. There, the upward flux of muons is written as

$$\begin{aligned}\frac{d\phi_\mu}{dE_\mu} &= \frac{\Gamma_A}{4\pi R_E^2}\int_{E_\mu}^{m_\chi} dE_\nu \left(\frac{dN_\nu}{dE_\nu}\right)_{F,\mu} R_\mu(E_\mu, E_{th}) \\ &\quad \times \left\{\frac{d\sigma_\nu^p}{dE_\mu}\rho_p + (p \to n)\right\} + (\nu \to \overline{\nu}),\end{aligned} \tag{5.2}$$

where $E_{th} = 50$ GeV. This expression accounts for the fact that muons have a range with an energy dependence, however, it does not account for the fact that over the distance $R(E_\mu, E_{th})$, the muon has a final energy of E_{th}. Eq. (5.2) does not represent the energy dependent upward muon flux, however, the muon rate for the upward muon events with $E_\mu > E_{th}$ as a function of m_χ obtained using Eq. (5.2) and the results using Eqs. (4.34) and (4.24) have similar shapes (Fig. 5.16) with the overall normalizations differing by a factor of two. In Fig. 5.16, the sharp decrease of contained muon rates with an increase in m_χ is due to the inefficient capture rate for high mass DM particles in the core of the Earth (see Table 4.3). On the other hand, for the upward muon events, we observe a mild decrease for the muon rates due to the compensation of the muon range which increases with initial muon energy, or equivalently with the DM mass.

In Fig. 5.17, we show the upward muon fluxes from Eq. (5.2), for the direct neutrino production (dashed line) and from the τ decay (dot-dashed line). Comparing results from Figs. 5.15 and 5.17, we find that the upward muon flux of Eq. (5.2) for $\chi\chi \to \nu\bar{\nu}$ case follows more closely the contained muon flux at high energies presented in Fig. 5.15 (dashed line) than the upward flux, with an enhancement at high E_μ because the muon range increases with muon energy. Clearly, the upward

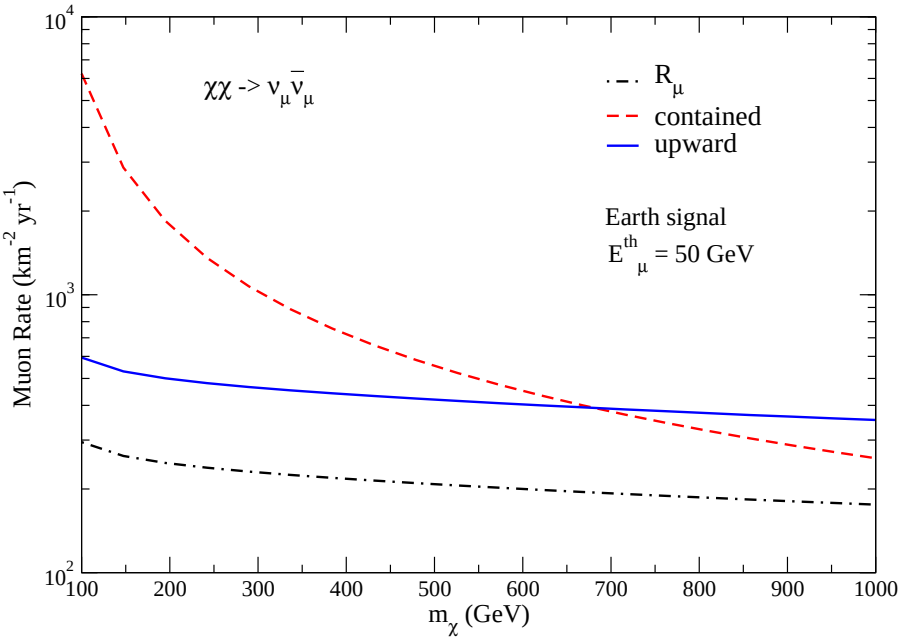

Figure 5.16: Muon rates for contained (dashed line) and upward (solid line) muon events due to dark matter annihilation in the core of the Earth; we consider $\chi\chi \to \nu_\mu \bar{\nu}_\mu$. We compare our results with those obtained by using Eq. (5.2) (dot-dashed line). In the figure, R_μ refers to Eq. (5.2), integrated over $E_\mu > E_{th}$.

muon flux in Fig. 5.17 (dashed line) does not accurately reflect the muon energy distribution of upward muon events from DM annihilation in the Earth. Similarly, a comparison of upward muon flux for $\chi\chi \to \tau^+\tau^-$, followed by $\tau \to \nu_\tau \mu \bar{\nu}_\mu$, obtained using Eq. (5.2) has a very different shape than the same flux obtained with Eq. (4.34). Comparable discrepancies are found between upward muon fluxes from Eq. (5.2) and our evaluation of upward muon events for DM annihilation in the Sun as well.

We also show with the solid line in Fig. 5.17 the results for upward muon flux from the $\chi\chi \to \tau^+\tau^-$ from Ref. [57]. In Ref. [57], the flux of muons comes from a PYTHIA simulation of the resultant muon neutrino flux and a simulation of muon electromagnetic energy loss. A DM distribution has been assumed in the Earth's

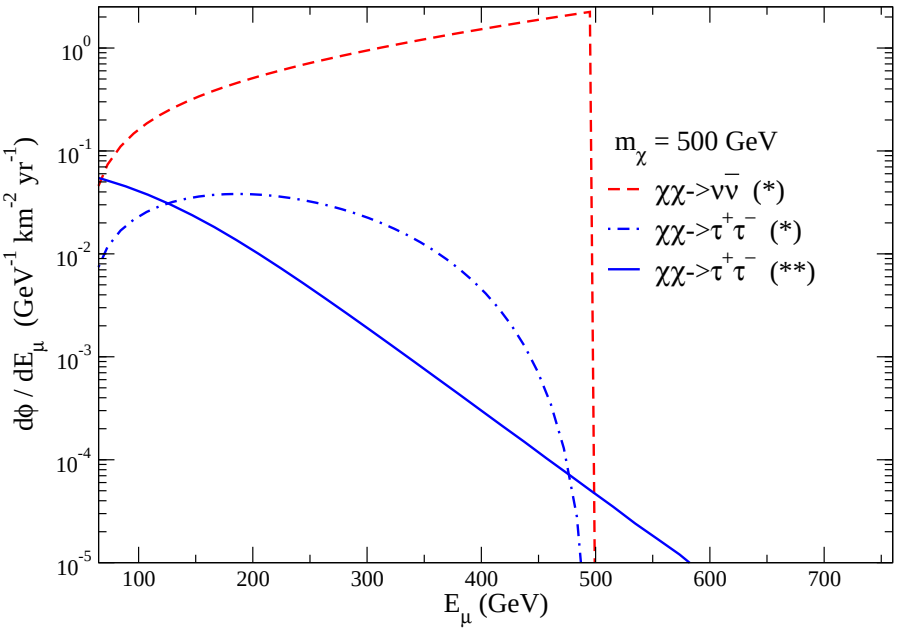

Figure 5.17: Upward muon fluxes obtained using Eq. (5.2) for $\chi\chi \to \nu_\mu \bar{\nu}_\mu$ (dashed line) and for $\chi\chi \to \tau^+\tau^-$, followed by $\tau \to \nu_\tau \mu \bar{\nu}_\mu$ (dot-dashed line), and the muon upward flux for $\chi\chi \to \tau^+\tau^-$ channel from Ref. [57] (solid line). The upward muon flux from Eq. (5.2) is inconsistent with the upward muon flux shown in Fig. 5.15. In the figure, (*) refers to Eq. (5.2) and (**) to Ref. [57].

core and contribution from DM annihilation around the center of the core with specific angular cuts ($\theta \leq 5^\circ$) have been applied, so the normalization should be lower. The energy distribution has qualitatively the same behavior as our results, however, it does not vanish at the kinematic limit when $E_\mu = m_\chi$.

Similar conclusions can be derived in the case of capture of DM in the core of the Sun. As noted earlier, there is attenuation of the initial neutrino flux as it propagates from the core to the exterior of the Sun. The interaction length of the neutrinos with energy ~ 30 GeV becomes equal to the column depth of the Sun (the average density of the core of the Sun is ~ 150 g/cm^3). At higher energies, the interaction length becomes even smaller and the neutrino flux is reduced significantly. We do

not include neutrino oscillation in the Sun [15], which depending on the DM model, might affect the flux of $\nu_\mu + \bar{\nu}_\mu$.

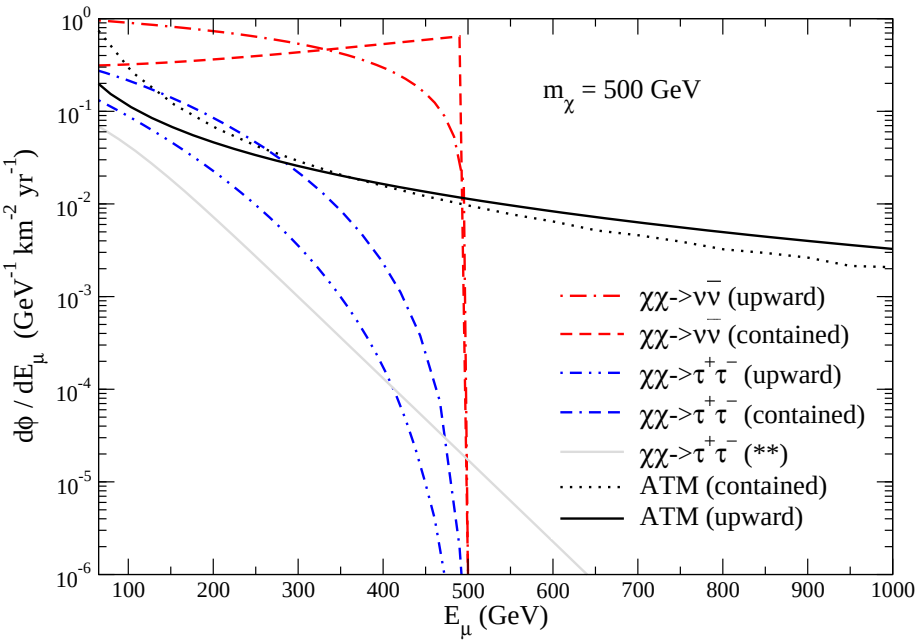

Figure 5.18: Muon fluxes obtained from dark matter annihilation into neutrinos in the core of the Sun, for upward events (dot-dashed and dot-dot-dashed lines), and for contained events (dashed and dot-dash-dashed lines). The upper curves are for the direct production of neutrinos, while the lower curves are for neutrinos from tau decays. Background upward muons are shown with the solid line and the contained muons are shown with the dotted line, where the evaluation used the angle-averaged atmospheric neutrino flux integrated over a solid angle with $\theta_{\rm max} = 1^\circ$. The thin solid line is from Edsjö's parametrization of the muon flux [57].

In Fig. 5.18, we show the upward muon and the contained muon fluxes for the direct production and for the τ production channels. In our calculations, we approximate neutrino attenuation in the Sun with an exponential suppression as presented in the previous section (Eqs. (3.39) and (3.40)). We note that this effect becomes stronger for higher neutrino energies which manifests itself when m_χ is large. Recall that the CC neutrino nucleon cross section increases with the neutrino

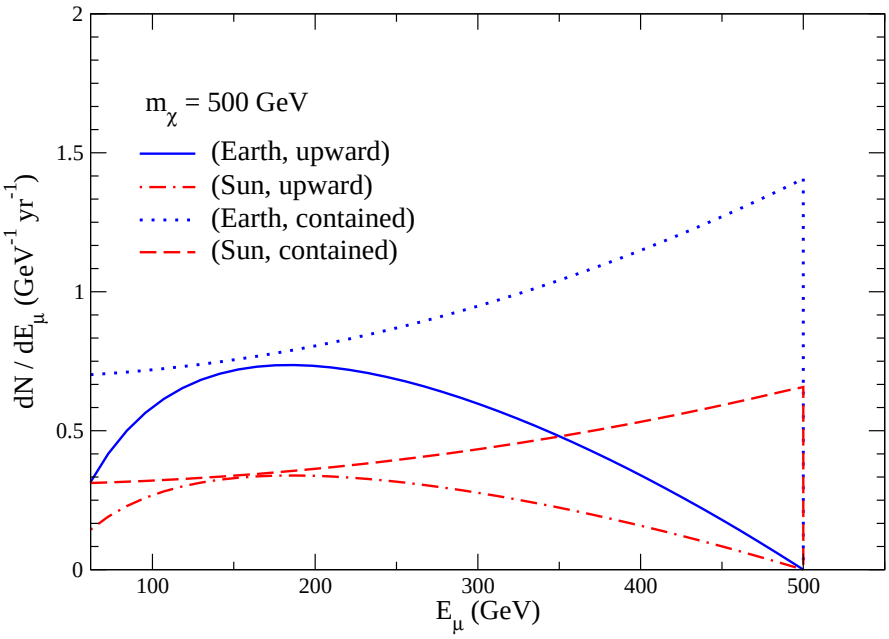

Figure 5.19: The upward muon flux times muon effective area obtained from dark matter annihilation to neutrinos in the core of the Earth (solid line) and Sun (dot-dashed line). For comparison, we also show the contained muon flux times 1 km^2 for the Earth (dotted line) and for the Sun (dashed line).

energy. As an example, the muon flux decreases by a factor of 3 for $m_\chi = 250$ GeV, factor of 10 for $m_\chi = 500$ GeV and two orders of magnitude for $m_\chi = 1$ TeV, as compared to the case with no attenuation.

We compare our results for muon flux with those in Ref. [57], where there is an assumption of DM distribution in the core of the Sun and contribution from DM annihilation around the center of the core with specific angular cuts have been applied. Effects due to neutrino flavor oscillations in the Sun have not been incorporated. The shape of the energy distribution is similar to our result, but with lower normalization and with a lack of the kinematic cutoff when $E_\mu = m_\chi$.

As in the case of the Earth, the upward muon flux from $\chi\chi \to \nu\bar{\nu}$ is larger than the contained flux for muon energies, $E_\mu < 380$ GeV, while in the case when

neutrinos are produced via $\chi\chi \to \tau^+\tau^-$, followed by $\tau \to \nu_\tau \mu \bar{\nu}_\mu$, the contained muon flux is always larger than the upward flux. We also show the angle-averaged atmospheric flux for a cone half angle 1°. For direct annihilation into neutrinos for the model in which the branching fraction is of the order of one, the signal is larger than the atmospheric background for both contained and upward muons. For the tau channel, signal is comparable to the background for upward muons when muons have energy around 200 GeV, however taking into account the effects of kinematics on the angular pointing of the muons at low energy may make this less apparent.

With the upward muon fluxes evaluated above from annihilation of DM in the Earth and the Sun, it is possible to estimate the event rate of muons in IceCube using the muon effective area given in Eq. (4.40). This effective muon area models the threshold detection effects near $E_\mu \sim 50$ GeV and local rock and ice below the IceCube detector. Fig. 5.19 shows our results for the upward muon flux times effective area with the solid and dot-dashed lines (solid for the Earth), and for the contained muon flux times the effective area of 1 km^2 (dotted and dashed lines, dotted for the Earth). The energy dependence of the effective area changes the shapes of the curves for upward muons at low energies.

5.3 Analytical Results for Final Muon and Shower Fluxes

The results that we present here are for the case of annihilating DM in the GC. The results for the annihilating DM signals from the cores of the Earth and the Sun can easily be found by re-scaling our results (see Table 4.3). The muon and shower fluxes for different annihilation channels are given. Independent of the overall normalizations, we present our results in terms of E_m which is the maximum possible energy for the muons or showers, i.e $E_m = m_\chi$ for annihilating DM particles. In order to obtain results for decaying DM, the re-scaling given in Eq. (4.11) can be used with setting $E_m = m_\chi/2$ in the equations below.

The differential upward muon flux for the $\chi\chi \to \nu\overline{\nu}$ channel is found to be

$$\frac{d\phi_\mu}{dE_\mu} = \frac{N_u}{(E_\mu + \alpha/\beta)}\Big[a(E_m - E_\mu) + \frac{b}{3E_m^2}(E_m^3 - E_\mu^3)\Big] \tag{5.3}$$

where

$$\begin{aligned} N_u &= B\frac{R_o\rho_o^2 B_F\langle\sigma v\rangle_F\langle J_2\rangle_\Omega\Delta\Omega m_p G_F^2 N_A}{4\pi^2\beta m_\chi^2} \\ &= 0.5859\left(\frac{m_\chi}{100\text{GeV}}\right)^{-2} B\langle J_2\rangle_\Omega\Delta\Omega \end{aligned} \tag{5.4}$$

in units of $\text{GeV}^{-1}\text{km}^{-2}\text{yr}^{-1}$. There is a separate distribution for neutrino and antineutrinos, since the parameters a and b depend on the incident particle and the target (see Tables 4.4 and 4.5). Also appearing are the Fermi constant $G_F \simeq 1.17\times10^{-5}$ GeV^{-2} and Avogadro's number $N_A \simeq 6\times10^{23}$. For standard rock, $\alpha \simeq 2\times10^{-3}$ $\text{GeV}\,\text{cm}^2/\text{g}$ accounts for the ionization energy loss and $\beta \simeq 3.0\times10^{-6}$ cm^2/g accounts for the bremsstrahlung, pair production and photonuclear interactions and we take $\rho = 2.6$ g/cm^3. Similar expressions can be derived as

$$\frac{d\phi_\mu}{dE_\mu} = N_c\left(a + b\frac{E_\mu^2}{E_m^2}\right)\Theta(E_m - E_\mu) \tag{5.5}$$

for the contained muon events and

$$\frac{d\phi_{sh}}{dE_{sh}} = N_c\left(a + b\frac{(E_m - E_{sh})^2}{E_m^2}\right)\Theta(E_m - E_{sh}) \tag{5.6}$$

for the shower events, where $\Theta(x) = 1$ if $x \geq 0$ and $\Theta(x) = 0$ otherwise, and

$$\begin{aligned} N_c &= DB\frac{R_o\rho_o^2 B_F\langle\sigma v\rangle_F\langle J_2\rangle_\Omega\Delta\Omega m_p G_F^2 N_A\rho}{4\pi^2 m_\chi^2} \\ &= 0.457\left(\frac{m_\chi}{100\text{GeV}}\right)^{-2} B\langle J_2\rangle_\Omega\Delta\Omega \end{aligned} \tag{5.7}$$

in units of $\text{GeV}^{-1}\text{km}^{-2}\text{yr}^{-1}$. where D is the size of the detector. We note that

$$\begin{aligned} \frac{d\phi_\mu}{dE_\mu} &\propto \rho^0 \quad \text{for the upward events} \\ \frac{d\phi_\mu}{dE_\mu} &\propto \rho^1 \quad \text{for the contained events,} \end{aligned}$$

so, the muon flux doesn't depend on the rock density for the upward events except through α and β, whereas for the contained events, the muon flux is directly proportional to the density of the medium.

All the expressions for the muon flux derived below contain a $\Theta(E_m - E_\mu)$ function. For secondary neutrinos which possess an energy spectrum in the form

$$\left(\frac{dN}{dE}\right)_\nu = A\left(\frac{E_\nu}{E_m}\right)^n \tag{5.8}$$

where A is an overall factor, the differential upward muon flux can be calculated by using

$$\begin{aligned}\frac{d\phi_\mu}{dE_\mu} &= \frac{N_u A}{E_m^n(E_\mu + \frac{\alpha}{\beta})}[P(E_m, E_\mu, n) + K(E_m, E_\mu, n) + \\ &+ L(E_m, E_\mu, n) + M(E_m, E_\mu, n)]\end{aligned} \tag{5.9}$$

where

$$\begin{aligned}P(E_m, E_\mu, n) &= \frac{aE_m^{(n+1)}(E_m - E_\mu)}{(n+1)} \\ K(E_m, E_\mu, n) &= -\frac{a(E_m^{(n+2)} - E_\mu^{(n+2)})}{(n+1)(n+2)} \\ L(E_m, E_\mu, n) &= \frac{bE_m^{(n-1)}(E_m^3 - E_\mu^3)}{3(n-1)} \\ M(E_m, E_\mu, n) &= -\frac{b(E_m^{(n+2)} - E_\mu^{(n+2)})}{(n-1)(n+2)}\ ,\end{aligned} \tag{5.10}$$

for $n \neq 1$ and when $n = 1$,

$$\frac{d\phi_\mu}{dE_\mu} = \frac{N_u A}{3E_m(E_\mu + \frac{\alpha}{\beta})}\left[E_m^3\left(a + \frac{b}{3}\right) - \frac{3aE_\mu E_m^2}{2} + E_\mu^3\left(b\ln\left(\frac{E_\mu}{E_m}\right) + \frac{a}{2} - \frac{b}{3}\right)\right]. \tag{5.11}$$

For the contained muon events and when $n \neq 1$,

$$\frac{d\phi_\mu}{dE_\mu} = \frac{N_c A}{E_m^n}\left[\frac{a}{(n+1)}(E_m^{(n+1)} - E_\mu^{(n+1)}) + \frac{bE_\mu^2}{(n-1)}(E_m^{(n-1)} - E_\mu^{(n-1)})\right]\ , \tag{5.12}$$

which reduces to

$$\frac{d\phi_\mu}{dE_\mu} = \frac{N_c A}{E_m}\left[\frac{a}{2}(E_m^2 - E_\mu^2) + bE_\mu^2\ln\left(\frac{E_m}{E_\mu}\right)\right]. \tag{5.13}$$

when $n = 1$. Similarly, for the shower events

$$\frac{d\phi_{sh}}{dE_{sh}} = \frac{N_c A}{E_m^n}\Big[\frac{a+b}{(n+1)}(E_m^{(n+1)} - E_{sh}^{(n+1)}) + \frac{bE_{sh}^2}{(n-1)}(E_m^{(n-1)} - E_{sh}^{(n-1)}) + -\frac{2bE_{sh}}{n}(E_m^n - E_{sh}^n)\Big] \tag{5.14}$$

when $n \neq 1$ and $n \neq 0$. It reduces to

$$\frac{d\phi_{sh}}{dE_{sh}} = N_c A\left[(a+b)(E_m - E_{sh}) - bE_{sh}^2\left(\frac{1}{E_m} - \frac{1}{E_{sh}}\right) + 2bE_{sh}\ln\left(\frac{E_{sh}}{E_m}\right)\right] \tag{5.15}$$

for $n = 0$ and

$$\frac{d\phi_{sh}}{dE_{sh}} = N_c A\left[\frac{(a+b)}{2E_m}(E_m^2 - E_{sh}^2) - \frac{2bE_{sh}}{E_m}(E_m - E_{sh}) - \frac{bE_{sh}^2}{E_m}\ln\left(\frac{E_{sh}}{E_m}\right)\right] \tag{5.16}$$

for $n = 1$.

5.4 Summary and Discussion

We have studied neutrino signals from DM annihilation in the GC. We have calculated contained and upward muon fluxes from neutrino interactions, when neutrinos are produced in annihilation of DM either directly or via the decay of taus, W-bosons or b-quarks. We have shown that in the case of direct neutrino production, the signal is above the atmospheric background for both contained and upward events, assuming that the annihilation rate is enhanced by boost factor of 200 (when the NFW DM halo profile is used) and that the branching ratio of DM annihilation into neutrinos is one. In general, the boost factor values that are required to explain the data obtained by the indirect detection experiments vary depending on the DM model and the DM mass. For the specific DM model our results can be rescaled by the corresponding product of the boost factor B and the branching ratio B_F.

We have found that the contained muon flux dominates over the upward muon flux for all energies when $m_\chi = 200$ GeV. However, as we increase the mass m_χ of the

DM particle, for example when $m_\chi = 500$ GeV, the upward muon flux dominates up to $E_\mu = 300$ GeV, and for $m_\chi = 800$ GeV, up to $E_\mu = 500$ GeV. This is due to the increasing muon range as the muon initial energy increases, which becomes possible when m_χ is larger thus producing higher energy neutrinos in the annihilation. In the case of secondary neutrino production, the signal becomes comparable to the background if the boost factor is an order of magnitude larger than the value we considered. We have shown that the shape of the muon flux depends on the specific decay mode, and that the dominant flux comes from tau decay at low muon energies, and from W-decay for muon energies above 200 GeV. The total upward muon rates have a weak dependence on m_χ and on the muon energy threshold for $m_\chi > 400$ GeV, due to the balance of the energy dependence of the muon range, the upper limit of the muon energy (given by m_χ) and the explicit dependence on m_χ ($\sim m_\chi^{-2}$) of the muon flux. However, the total contained muon rates show a sharp decrease with m_χ for $m_\chi > 150$ GeV due to the finite size of the detector. Upward muon events dominate over contained muon events for $m_\chi > 550$ GeV.

We have also shown that showers produced by neutrino interactions, when neutrinos are produced directly in DM annihilation, could also be used to detect a DM signal from the GC. In particular, electromagnetic showers have much smaller background, from atmospheric electron neutrinos, than the hadronic showers. In addition, we have studied the contour plots of both the upward muon events and the showers and we have shown the required dependence of the annihilation cross section on the DM mass in order to observe a fixed number of event rates. We have discussed the origin of different shapes for the contour curves in each case and pointed out the contained event nature of the shower events. We have shown that after one year IceCube+DeepCore detector could potentially observe a 5σ signal effect by measuring contained muons (for direct neutrino production), or in 5 to 8 years a 2σ effect with hadronic showers even in the case when they are due to secondary neutrinos.

IceCube+DeepCore will be able to identify track-like events due to the CC interactions of muon neutrinos, the showers due to NC interactions of all the neutrino

flavors and the CC interactions of electron and tau neutrinos. In particular, above the neutrino energy of 40 GeV the signal to background ratio for showers is further enhanced since the atmospheric tau and electron neutrino fluxes are suppressed relative to the atmospheric muon neutrino flux. Thus, the main background is the NC interaction whose cross section is about a factor of three less than the CC cross section of the atmospheric muon neutrinos. The measurement of the ratio of track-like muon and shower events eliminates the dependence on some parameters of the theory (e.g., boost factor, the DM density profile, etc) which only determine the overall normalization for the energy dependent differential muon fluxes, so the physical properties of the DM particle can better be determined.

In addition to the possible signals to be detected in the neutrino telescopes due to DM annihilation in the GC, we have also calculated muon fluxes from DM annihilation, when DM is trapped in the the Sun's (Earth's) core. Without using a specific model for DM, we have considered $\chi\chi \to \nu\bar{\nu}$ and $\chi\chi \to \tau^+\tau^-$, followed by $\tau \to \nu_\tau \mu \bar{\nu}_\mu$ channels as representatives of direct and of the secondary neutrino production. We have taken into account neutrino attenuation as it propagates from the core of the Sun to its surface. In the evaluation of the upward muon flux, we have incorporated muon energy loss, as described by the muon range.

We have shown that our results exhibit a very different energy dependence than those obtained from Eq. (5.2) that is widely used in the literature [15, 51, 53, 106, 208, 209, 210], however, there is reasonably good agreement with the parametrization of Ref. [50, 57] away from the region of maximum energy $E_\mu \sim m_\chi$. Our results are obtained with the assumption that the DM annihilation occurs at the maximum rate, when the annihilation rate is half the capture rate. This is reasonable for the Sun but requires significant enhancement of the capture rate (or annihilation cross section) for the Earth to be in equilibrium [53].

In our calculation we have used spin independent DM-nucleon cross sections which have much stronger experimental bound than the spin dependent cross sections [108, 109, 207, 211, 212, 213, 214, 215, 216, 217]. In the core of the Sun the capture rate might be dominated by the spin dependent (SD) DM-hydrogen nucleus

interactions, which would increase the signal rates by a couple of orders of magnitude and still be consistent with AMANDA limits on annihilation rates [37, 38].

Furthermore, incorporating neutrino oscillations and the regeneration effects in the Sun will likely affect the final muon flux from DM annihilations in the Sun, especially in the models which possess an asymmetry in the initial neutrino fluxes or where $\chi\chi \to \tau^+\tau^-$ is the dominant mode [15]. We have used a model independent normalization, $\sigma_0^i \simeq 10^{-8} N_i^4$ pb and $B_F = 1$ to evaluate the muon flux. We have found that for this branching fraction signals from $\chi\chi \to \nu\bar{\nu}$ and $\chi\chi \to \tau^+\tau^-$, followed by $\tau \to \nu_\tau \mu \bar{\nu}_\mu$, when DM annihilation happens in the core of the Sun, are comparable or even larger than the background (upward) muons from atmospheric neutrinos. In the case of direct neutrino production, the upward muon flux is larger than the contained flux for $E_\mu < 350$ GeV for $m_\chi = 500$ GeV, due to the muon range. When neutrinos are produced via secondary processes, contained events always dominate upward muons.

Model dependence is an important element, for example, $\chi\chi \to \nu\bar{\nu}$ is not allowed when the DM particles are neutralinos [15]. However, with the formalism developed, one can determine muon fluxes for specific DM model by summing up the contributions from all decay channels weighted with corresponding branching fractions.

CHAPTER 6

PROBING DARK MATTER MODELS WITH NEUTRINOS

The ingredients for theoretical predictions of particle fluxes from DM annihilation or decay include a model for the DM distribution, a particle physics model for the DM particle couplings to SM particles, and SM physics processes for the resulting produced particles. In this chapter, we analyze the neutrino signals from DM particles proposed by different particle physics models. For the DM distribution in the galaxy, we use the Navarro-Frenk-White (NFW) [92] profile as a typical realistic DM density profile. The expressions for the neutrino fluxes and its dependence on the DM profile are presented in Chapters 3 and 4. In case of DM decay (annihilation), the neutrino spectrum has linear (quadratic) dependence on the DM density.

The particle physics models on which we focus in this study consist of the leptophilic, Kaluza-Klein and gravitino DM particles. Either thermal averaged annihilation cross section times velocity $\langle \sigma v \rangle$ or a decay time τ specific to the model is required. Characteristically for annihilation, the required $\langle \sigma v \rangle$ is larger [64, 66, 77, 218, 219] than the value required for a thermal relic abundance [13, 55]: $\langle \sigma v \rangle_0 = 3 \times 10^{-26}$ cm^{3}s^{-1}. Following the current convention, we write

$$\langle \sigma v \rangle = B \, \langle \sigma v \rangle_0 \ , \tag{6.1}$$

with a boost factor B. There are theoretical evaluations of the boost factor [30, 54, 124, 125, 126, 220, 221], however, we treat the boost factor as a phenomenological parameter in this study. To explain the lepton excesses, some models have constraints on the boost factor as a function of DM mass [77].

In leptophilic DM models [76, 77, 78, 79, 80, 81, 82, 83, 222, 223] explaining the PAMELA positron excess, the DM annihilation or decay must proceed dominantly to leptons in order to avoid the overproduction of antiprotons. Moreover, according to the FERMI data, the direct production of electrons must be suppressed with

respect to the production of electrons (and positrons) as secondaries. It was shown [77] that the leptophilic DM with mass (m_χ) in the range between 150 GeV and a few TeV, which annihilates or decays into τ's or μ's can fit the PAMELA [116] and Fermi [33] data as well as the HESS high energy photon data [24, 32]. The best fit parameters for the boost factor (B) and the decay time (τ) which determine the overall normalizations, for the specific case involving muons from annihilation ($\chi\chi \to \mu^+\mu^-$) or decay ($\chi \to \mu^+\mu^-$), respectively, are given by [77]

$$\begin{aligned} B &= 431 m_\chi - 38.9 \\ \tau &= \left(2.29 + \frac{1.182}{m_\chi}\right) \times 10^{26} \text{ sec} \\ &= B_\tau \times 10^{26} \text{ sec} \end{aligned} \tag{6.2}$$

for m_χ in TeV. The annihilation channel into tau pairs is less favored by the data [77].

Some Kaluza-Klein models can provide a DM candidate which gives the correct relic density [75]. To account for the HESS results [24, 32], the lightest Kaluza-Klein particle (LKP) would have a mass of the order of a TeV [74]. The LKP is also assumed to be neutral and non-baryonic. In this model, the particle couplings are fixed such that LKP pairs annihilate into quark pairs (35%), charged lepton pairs (59%), neutrinos (4%) and higgs/gauge bosons (2.0%) [74, 75].

The first DM candidate proposed in the context of supersymmetry is the gravitino ($\psi_{3/2}$) which would be the lightest supersymmetric particle (LSP). The gravitino is the superpartner of the graviton. With the existence of small R-parity breaking to allow the LSP to decay, the gravitino decays into SM particles. The decay rate of the gravitino in this scenario is so small that it can have a sufficiently long lifetime for the correct DM relic density today.

In order to account for the observed anomalous positron excess in the PAMELA data and positron plus electron excess in the FERMI data, the lifetime of the gravitino DM is constrained to be of the order of $\sim 10^{26}$ seconds and its mass to be in the range between few 100 GeV and few TeV [87]. To explain the data, the three-body gravitino decay mode ($\psi_{3/2} \to l^+ l^- \nu$) was considered [87]. We use the parameters

of this model to explore neutrino signals from gravitino decay. For illustration, in addition to three-body decay, we also consider the two-body gravitino decay modes ($\psi_{3/2} \rightarrow (W^{\mp}l^{\pm}, Z\nu, \gamma\nu)$) assuming the same lifetime and mass as for the three-body decay, and with the branching fractions given in Table 6.1.

Table 6.1: Branching fractions for the two-body gravitino decay into different R-parity violating channels for different masses [85].

$m_{\psi_{3/2}}$(GeV)	$B_F(\psi_{3/2} \rightarrow \gamma\nu)$	$B_F(\psi_{3/2} \rightarrow Wl)$	$B_F(\psi_{3/2} \rightarrow Z\nu)$
10	1	0	0
85	0.66	0.34	0
100	0.16	0.76	0.08
150	0.05	0.71	0.24
200	0.03	0.69	0.28
400	0.03	0.68	0.29

Table 6.2: Model parameters characterizing fits to explain FERMI and PAMELA anomalies used as examples in this study.

Particle/mode	mass	B_τ or B
$\psi_{3/2} \rightarrow l^+l^-\nu$	400 GeV	B_τ=2.3
$\psi_{3/2} \rightarrow (Wl, Z\nu, \gamma\nu)$	400 GeV	B_τ=2.3
$\chi \rightarrow \mu^+\mu^-$	2 TeV	B_τ=2.9
$B^{(1)}B^{(1)} \rightarrow (q\bar{q}, l^+l^-, W^+W^-, ZZ, \nu\bar{\nu})$	800 GeV	$B = 200$
$\chi\chi \rightarrow \mu^+\mu^-$	1 TeV	$B = 400$

Selected DM model parameters are shown in Table 6.2. For each of the DM models considered, the decay distribution of the produced particles to neutrinos in case of DM annihilation, or the gravitino decay distribution to neutrinos, enters into the calculation of the neutrino fluxes that arrive at Earth. For annihilation directly to neutrinos, the energy distribution of each neutrino is a delta function in energy, with the energy equal to the DM mass. This case has been well studied in the literature [53, 70, 71, 224, 225, 226]. Here, we look at the secondary neutrinos. Fig.

6.1 shows neutrino spectra, plotted in terms of $x \equiv E_\nu/E_{\nu,max}$ where $E_{\nu,max} = m_\chi$ for annihilating DM and $E_{\nu,max} = m_\chi/2$ for decaying DM models. The curves in the figure are normalized to count the number of neutrinos, and in the case of the $Z\nu$ final state, the fraction of Z decays to neutrinos. The muon neutrino spectra in the figure should be multiplied by the branching fraction for a specific decay channel in a given model.

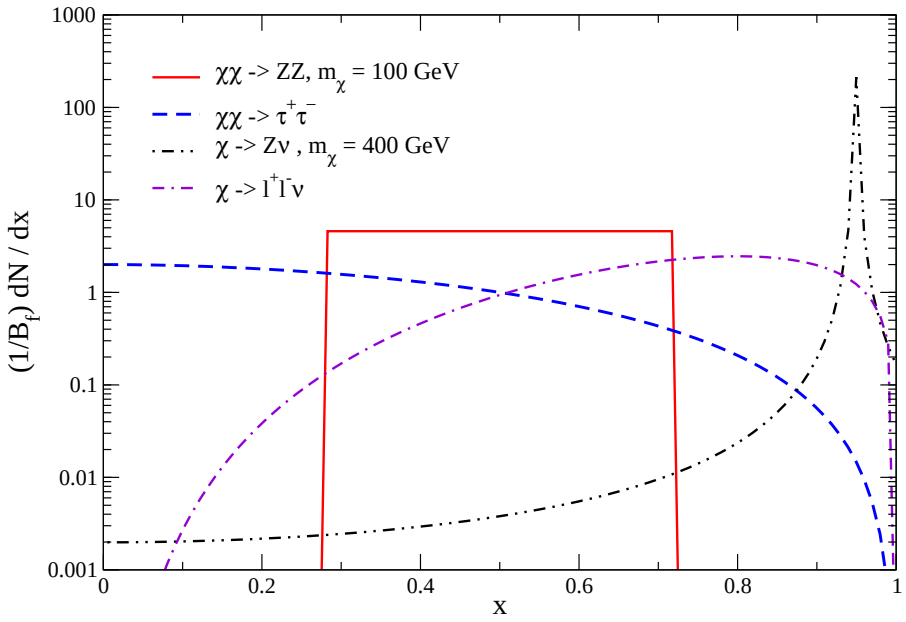

Figure 6.1: Muon neutrino (ν_μ) spectra in terms of $x = E_\nu/E_{\nu,max}$ from the three-body decay of gravitino (dot-dash-dashed line), from the decay of τ (dashed line), Z boson (solid line) and from one of the two-body decay channels of gravitino ($\psi \to Z\nu$) for which Breit-Wigner distribution is used. The distributions should be multiplied by the branching fractions, and oscillations should be taken into account for the flux of neutrinos at Earth.

The neutrino flux at Earth can be evaluated using the neutrino flux expressions given by Eqs. (4.7) and (4.8) and the neutrino spectra given in Chapter 3 with taking the neutrino oscillation effects into account. In Fig. 6.2, we show the muon neutrino flux at Earth for three decay channels and two annihilation channels.

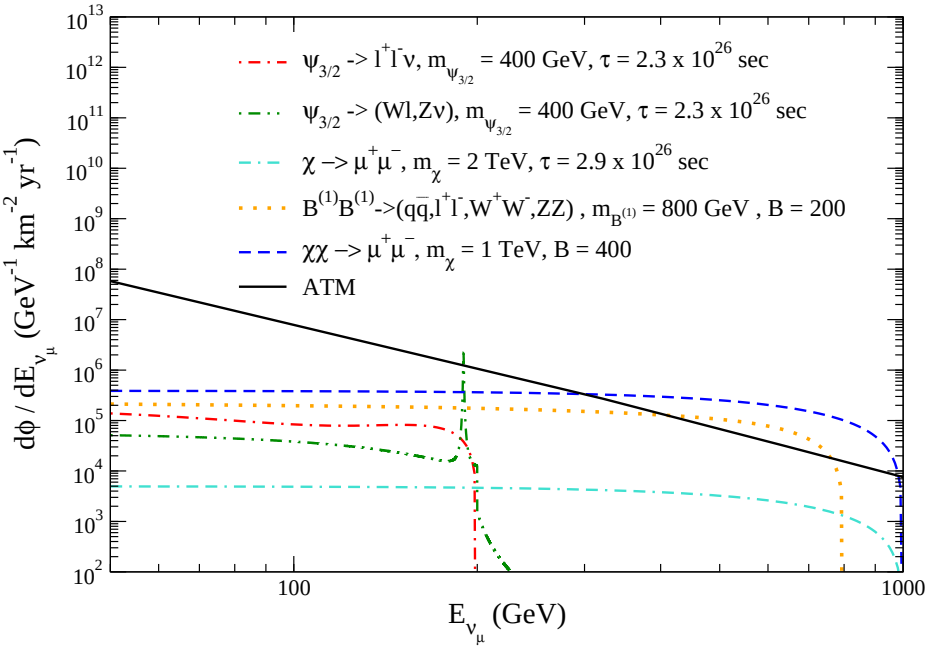

Figure 6.2: Muon neutrino (ν_μ) fluxes from the annihilation of the Kaluza-Klein (dotted line), leptophilic (dashed line), and the decay of leptophilic (dash-dot-dashed line), three-body decay (dot-dashed line) and two-body decay (dot-dot-dashed line) of gravitino DM particles. Neutrino oscillations have been taken into account. The angle-averaged atmospheric muon neutrino flux at the surface of the Earth is also presented (solid line). The corresponding values of the parameters for each model are shown as well.

In some DM models all three flavors of neutrinos can be generated by DM annihilation or decay, implying the flavor ratio $\nu_e : \nu_\mu : \nu_\tau$ at the production site to be 1:1:1. This ratio remains unchanged with oscillation. This is the case for the gravitino decay and Kaluza-Klein DM annihilation. However, in case of the leptophilic DM model, in which $\chi \to \mu^+\mu^-$, the initial neutrino flavor ratio is $1 : 1 : 0$ which becomes $1 : 0.5 : 0.5$ as neutrinos travel astrophysical distances for maximal mixing of muon and tau neutrinos. We take this oscillation effect into account when we evaluate muon neutrino fluxes presented in Fig. 6.2 and when we evaluate muon event rates below.

Fig. 6.2 shows that with the exception of the gravitino decays, the distributions of neutrinos have very weak energy dependence. The two-body gravitino decay gives a spiked feature at the kinematic limit in neutrino energy. The relative normalizations of the DM curves comes from different DM lifetimes or boost factors. Also shown in Fig. 6.2 is the angle-averaged atmospheric muon neutrino flux at the surface of the Earth as described in Chapter 4.

6.1 Neutrino Signals from Dark Matter

For each DM candidate and model, there are several signals to pursue in underground detectors. One possibility is to measure or constrain the rate of muons produced by muon neutrinos, over and above the expected atmospheric background rate. High energy muons point essentially in the same direction as the incident neutrino, and the angular resolution of high energy muon tracks is quite good. With good enough energy and angular resolution, and a large enough target volume, one looks for neutrinos coming directly from DM annihilation in the GC, however, the target volume may be a limitation for constraining model parameters including the boost factor. A comparison of the upward-going muon rate, where the target volume is enhanced by the muon range at high energies, and the contained rate of muon production by neutrinos in the detector, is a useful exercise.

For the IceCube+DeepCore detector, the GC is above the horizon, so the upward muon rate of DM produced neutrinos is from the Galactic halo in a direction pointing away from the GC. We consider this possibility as well.

Showers, either electromagnetic or hadronic, are produced by neutrinos. We look at the optimization for these as well as a function of cone half angle, but we note that the current capabilities for shower angular resolution are somewhat limited, on the order of 50° [88, 133].

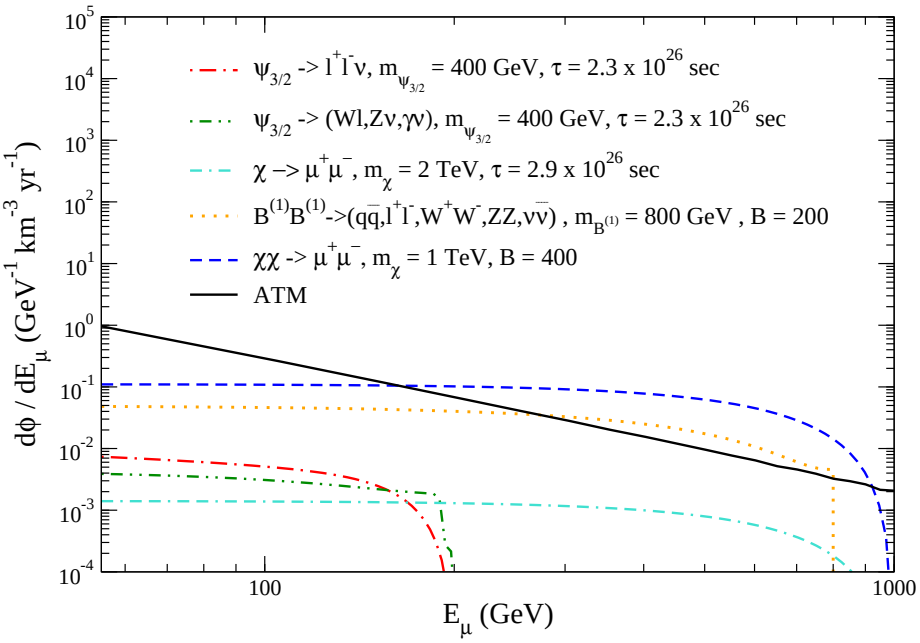

Figure 6.3: Muon flux for the contained events for gravitino decay (dot-dashed and dot-dot-dashed lines), Kaluza-Klein annihilation (dotted line), leptophilic model (dashed line for annihilation and dash-dash-dotted line for decay) compared with the atmospheric background (solid line), for the case when $\theta_{\rm max} = 1^\circ$. Model parameters are given in Table 6.2.

6.1.1 Contained and Upward Muon Fluxes

We evaluate the muon flux from neutrino CC interactions in the detector, when neutrinos are produced in DM annihilation or DM decay. In Fig. 6.3 we show muon fluxes for the case when the DM particle is a gravitino, a Kaluza-Klein particle and for a leptophilic model in which DM annihilation or decay produces $\mu^+\mu^-$, for the model parameters listed in Table 6.2. We take the cone half angle around the GC to be $\theta_{\rm max} = 1^\circ$.

In case of the gravitino DM decay and for Kaluza-Klein DM annihilation, there are discontinuities in the slopes at the highest muon energies coming from the superposition of the direct neutrino production (dot-dot-dashed line for DM decay

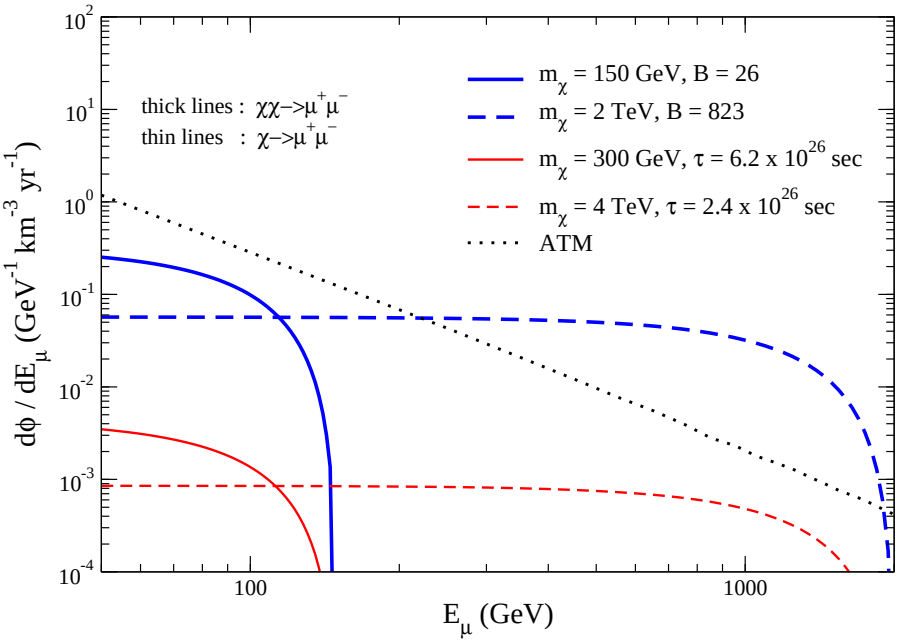

Figure 6.4: Contained muon flux from the annihilation, $\chi\chi \to \mu^+\mu^-$ (thick lines) and the decay, $\chi \to \mu^+\mu^-$ (thin lines) processes. The relation between the boost factor and m_χ, and between the lifetime and m_χ are given by Eq. (6.2). We take $\theta_{\rm max} = 1^\circ$.

and dotted line for the Kaluza-Klein annihilation). The direct neutrino production, $\chi\chi \to \nu\bar{\nu}$ is the "golden channel" for DM detection because in this case the muon flux is increasing with energy, and it peaks at $E_\mu = m_\chi$ [71].

As noted in previous section, the parameters used for DM masses, boost factors and lifetimes are characteristic of those that were shown to describe PAMELA, Fermi/LAT and HESS data [74, 77, 87]. Changing the value of the boost factor or the lifetime affects only the overall normalization of the muon flux. We find that for this choice of the parameters, DM signals in leptophilic model exceed the atmospheric background for $E_\mu > 175$ GeV, while for the Kaluza-Klein DM model the signal is above the background for $E_\mu > 275$ GeV. In both cases, the signal cuts off when $E_\mu = m_\chi$.

We consider the effect on the muon flux shape when we change the parameters, for example for the leptophilic model. In Fig. 6.4 we show the contained muon flux from DM annihilation and decay in a leptophilic model for different values of the parameters B, τ and m_χ, which are constrained to satisfy Eq. (6.2) to describe the data [77]. The decays (lower thin lines) have lower fluxes than the annihilations (upper thick lines), even though the shapes are similar. For leptophilic models, one cannot enhance the signal rate by increasing B or decreasing τ with m_χ fixed if the Fermi and PAMELA data are explained by the model.

Contained muons, produced by neutrino interactions in the detector, make up one set of muon signals. Muons can also be produced in neutrino interaction in the rock below the detector. Muons produced with energy E_μ^i, interact with the medium and finally reach the detector with energy E_μ. The effective volume of the detector is enhanced by the muon range at high energies. We denote these events as upward muon events (see Chapter 4 for details).

We show in Fig. 6.5, the upward muon flux for a generic northern hemisphere detector, looking down through the Earth with a cone half angle of $\theta_{\rm max} = 1^\circ$ around the GC. The muon fluxes are smoothed relative to Fig. 6.3 as a consequence of the energy loss. For DM particles with masses of order 1 TeV, the upward muon flux is larger at low energies than for the contained muons because the muon range is larger than 1 km, effectively enhancing the volume of the kilometer-size detector. When $m_\chi = 400$ GeV, the energies of the produced muons are such that the muon range is less than 1 km, which is the size of the detector for which the contained muon flux was calculated. If the depth of the detector is 500 m, the contained and upward muon fluxes for the DM mass of 400 GeV would be approximately equal at low energies, although the contained muon flux would have a little harder spectrum. This is direct consequence of muon range dependence on the DM mass. For example, muon with initial energy of 400 GeV (1 TeV) has a range of 500 m (1 km).

The contained and upward muon event rates are obtained by using Eqs. (4.38) and (4.39) where we consider an energy independent IceCube+DeepCore effective volume, $V_{\rm eff} = 0.04$ km^3, for the contained muon events [62, 88] and the angle-

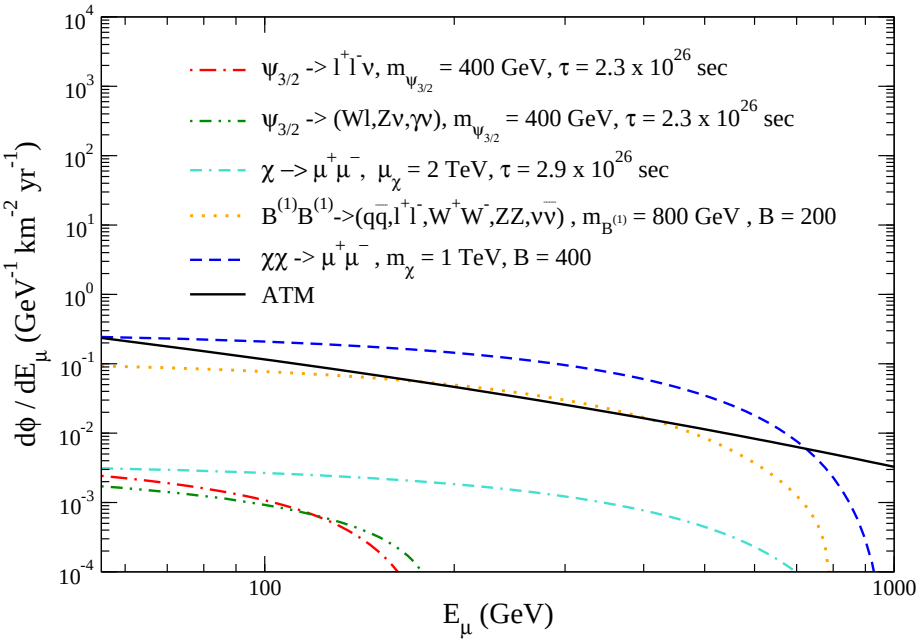

Figure 6.5: Upward muon flux for the annihilating and decaying DM models from Table 6.2. We take $\theta_{\max} = 1^\circ$.

averaged muon effective area, $A_{\text{eff}} = 1$ km^2, for the upward muon events to be observed in a kilometer-size detector in the Northern Hemisphere. In our calculations, we also choose $E_\mu^{th} = 50$ GeV for the energy threshold of the muon detector.

The event rates for contained and upward muons for a cone half angle of $\theta_{\max} = 1^\circ$ are shown in Table 6.3 for different DM models. We also obtain the number of years required for the 2σ detection significance (see Eq. (4.42)). From Table 6.3 we note that for the parameters that we considered, only the Kaluza-Klein DM and leptophilic annihilation models have a reasonable chance of detection for $\theta_{\max} = 1^\circ$.

The model parameters such as DM masses, annihilation cross sections and decay times that we consider are introduced to explain some indirect DM searches as explained in the previous section. However, it is also possible that the signals that have been observed [24, 32, 33, 116] in these searches have no DM origin. Then,

Table 6.3: Event rates per year and the time required to reach 2σ detection significance for the upward and the contained muons (μ) for a cone half angle of $\theta_{\max} = 1^{\circ}$. Results for different DM models are obtained by taking $A_{\rm eff} = 1{\rm km}^2$ and $V_{\rm eff} = 0.04$ km^3 for the upward and contained muon events, respectively.

	$A_{\rm eff} = 1{\rm km}^2$		$V_{\rm eff} = 0.04$ km^3	
	N_μ^{up}	t (yr)	N_μ^{ct}	t (yr)
$\psi_{3/2} \rightarrow l^+l^-\nu$	0.12	7811	0.0224	1.8×10^4
$\psi_{3/2} \rightarrow (Wl, Z\nu, \gamma\nu)$	0.1	1.1×10^4	0.0156	3.8×10^4
$\chi \rightarrow \mu^+\mu^-$	0.6	317	0.027	1.2×10^4
$B^{(1)}B^{(1)} \rightarrow (q\bar{q}, l^+l^-, \nu\bar{\nu}, ...)$	16	0.7	0.72	23
$\chi\chi \rightarrow \mu^+\mu^-$	46	0.14	2.1	4
ATM	28		2.28	

m_χ and B or τ can be varied independently. In terms of the neutrino signals, the dependence of the signals on the annihilation cross sections or on the decay times is trivial since these parameters affect only the overall normalization. The dependence on DM mass is not that straightforward.

In order to see the dependence of the signals on DM mass, we set the values of the boost factor and the decay times to those in Table 6.2 and calculate the event rates as a function of DM mass for each model. We present our results for the contained muon event rates in Fig. 6.6 and for the upward muons in Fig. 6.7. The solid line in each figure corresponds to the muon background due to the atmospheric neutrinos.

From Fig. 6.6 we note that the contained muon rates for annihilating DM models decrease with m_χ. On the other hand the event rates for the decaying DM models increase slowly with m_χ, for $m_\chi < 1$ TeV and for $m_\chi > 1$ TeV, they become almost independent of m_χ. The m_χ dependence of the contained muon event rates is mainly due to the m_χ^{-2} (m_χ^{-1}) dependence in the neutrino flux for DM annihilation (DM decay) combined with the upper limit of integration dependence on m_χ. For DM masses in the range $E_\mu^{th} < m_\chi < 400$ GeV, where $E_\mu^{th} = 50$ GeV, the integration region is sensitive to the value of the DM mass, while for $m_\chi \gg E_\mu^{th}$ there is only

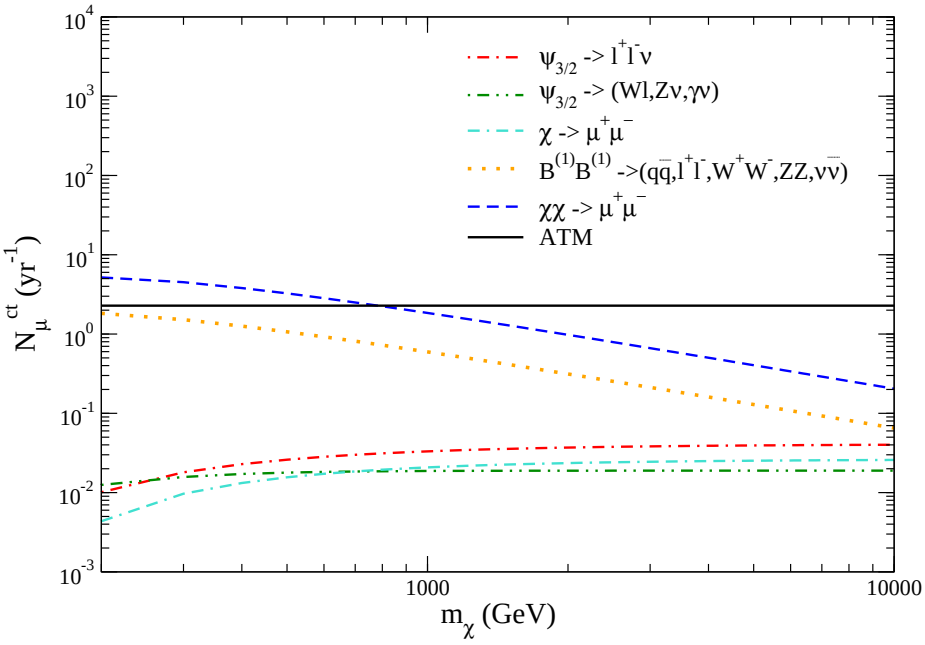

Figure 6.6: Contained muon rates as a function of DM mass for the models presented in Table 6.2. We take the muon detector threshold to be $E_\mu^{th} = 50$ GeV and the cone half angle to be $\theta_{\max} = 1^\circ$.

weak dependence on m_χ. These combined effects are responsible for the observed m_χ dependence of the contained muon event rates presented in Fig. 6.6.

The m_χ dependence of the upward muon rates is shown in Fig. 6.7. We find that the event rates for decaying DM models increase with m_χ while for annihilating DM models there is almost no m_χ dependence for a wide range of DM masses. In contrast to the contained muon rates, for upward muons there is additional m_χ that is present in the muon range. As we increase the value of DM mass, the effective volume which depends on the muon range in rock becomes larger.

The upward muon rates for a decaying DM particle have steeper increase with increasing DM mass than for contained muon rates, because of the energy dependent effective volume which increases with m_χ, when compared to the case for the contained muon events.

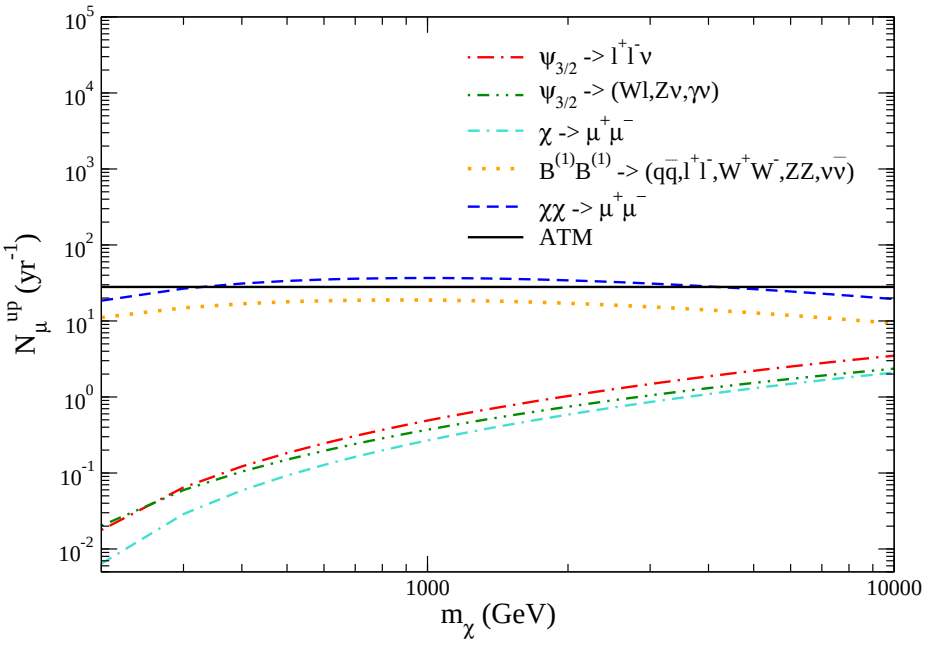

Figure 6.7: Upward muon rates as a function of DM mass for the DM models presented in Table 6.2. We take the muon detector threshold to be $E_\mu^{th} = 50$ GeV and the cone half angle to be $\theta_{\max} = 1^\circ$.

In Fig. 6.8, we present results for DM annihilation cross section required for a given DM mass in order to reach 2σ detection significance in five years of observation within $\theta_{\max} = 1^\circ$ for Kaluza-Klein (solid lines) and annihilating leptophilic (dashed lines) models. From Fig. 6.6 we note that the contained muon event rates decrease with m_χ for a fixed annihilation cross section (i.e. fixed boost factor). Therefore, in order to have the same detection significance for each DM mass, DM annihilation cross section needs to increase with m_χ as shown in Fig. 6.8. However, for the upward muons, the event rates increase with m_χ for $m_\chi < 1$ TeV and exhibit a slight decrease for higher DM masses for a fixed annihilation cross section. Thus, in order to have the same significance independent of the DM mass for the upward muon events the DM annihilation cross section has to decrease with m_χ for $m_\chi <$ 1 TeV and increase for $m_\chi > 1$ TeV as seen in Fig. 6.8. If there is no signal

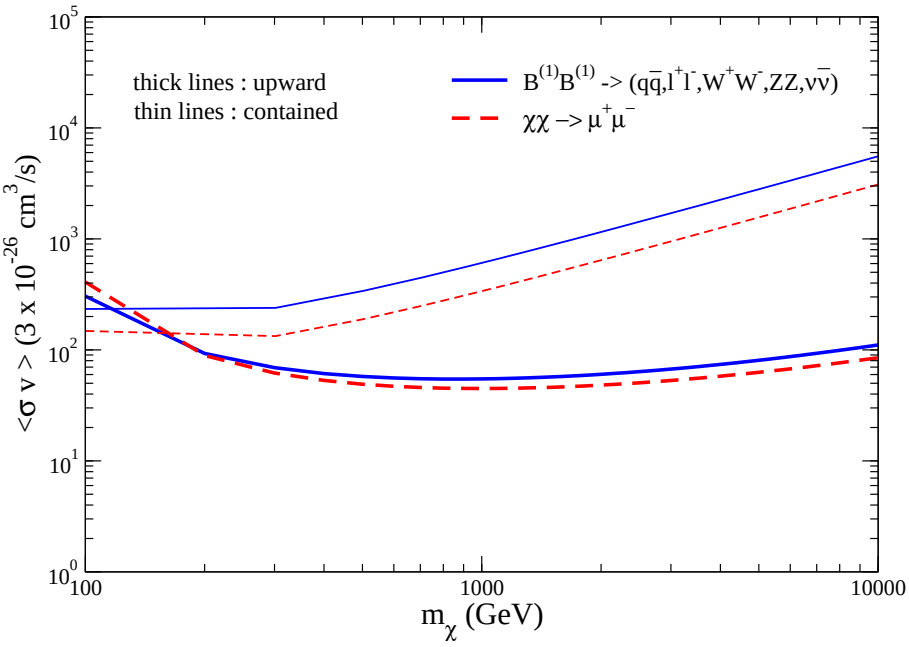

Figure 6.8: Annihilation cross section versus DM mass for upward and for contained muon events to reach 2σ detection significance with five years of observation for the case of Kaluza-Klein (solid lines) and leptophilic (dashed lines) models. We take $\theta_{\rm max} = 1^\circ$ and $E_\mu^{th} = 50$ GeV.

detected at 2σ level in five years, the parameter space above each curve is excluded at that significance level. Our results also indicate that the upward muons are more promising than the contained muons in constraining the model parameters. Increasing the observation time would result in larger excluded parameter space.

Similar to the models for the annihilating DM, we evaluate the parameter space for the decaying DM models. In Fig. 6.9 we show the decay time as a function of the DM mass for $\theta_{\rm max} = 1^\circ$ that is needed in order to reach 2σ detection significance with five year observation period. For a wide range of DM masses, the contained muon event rates have weak dependence on m_χ, while the upward muon event rates show a steep increase with increasing m_χ as can be seen from Figs. 6.6 and 6.7. This implies that we need longer decay time for the upward muon events than for

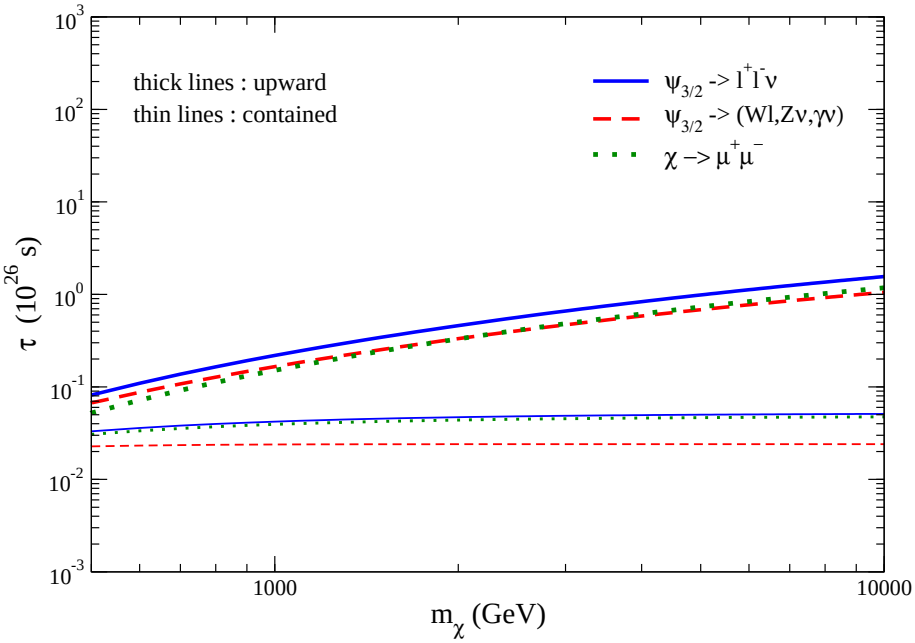

Figure 6.9: Decay time versus DM mass for upward and for contained muon events to reach 2σ detection significance with five years of observation for the case of decaying DM models: gravitino three-body(solid lines), gravitino two-body (dashed lines) and leptophilic (dotted lines). We take $\theta_{\rm max} = 1^\circ$ and $E_\mu^{th} = 50$ GeV.

the contained muon events to reach the same detection significance for a five year observation time while the decay time has almost no dependence on the DM mass for the contained muon events. The parameter space below each curve corresponds to the exclusion region at 2σ level after five years of no signal detection.

As noted earlier, size of the cone (cone half angle value) that is too small can restrict the number of events too much. In Fig. 6.10, we present contour plots similar to those in Fig. 6.9 but for $\theta_{\rm max} = 10^\circ$. With increasing θ_{max} from 1° to 10°, the J factor ($\langle J_1 \rangle_\Omega \Delta\Omega$) entering into the neutrino flux increases, resulting in stronger restriction on the DM lifetime.

In what follows we consider cone half angles larger than $\theta_{\rm max} = 1^\circ$. In Fig. 6.11, the detection times required for the 2σ detection significance for the Kaluza-Klein

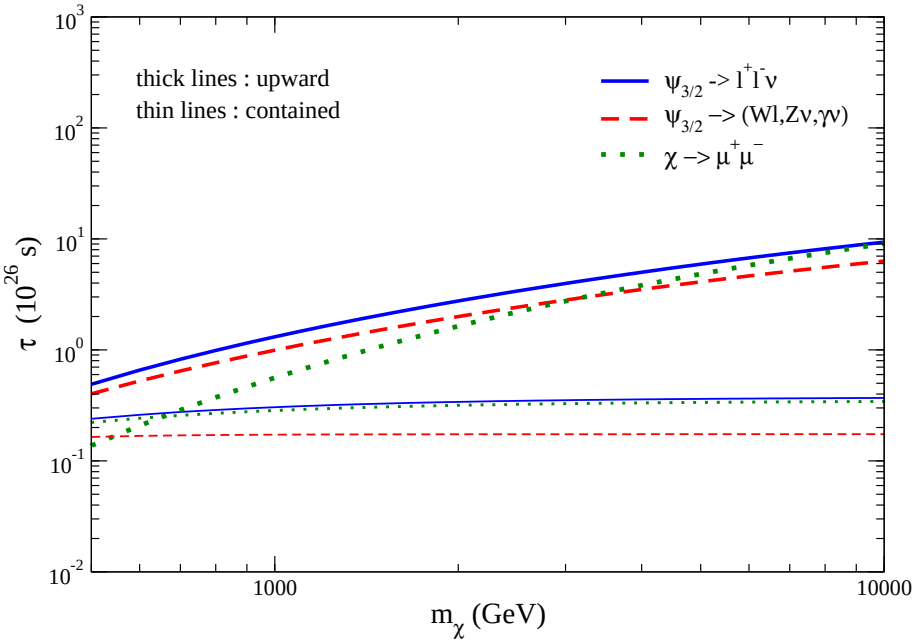

Figure 6.10: Decay time versus DM mass for both upward and contained muon events to reach 2σ detection significance after five years of observation for the case of decaying DM models: gravitino three-body (solid lines), gravitino two-body (dashed lines) and leptophilic (dotted lines). We take $\theta_{\rm max} = 10^\circ$ and $E_\mu^{th} = 50$ GeV.

and leptophilic annihilation cases are shown as a function of cone half angle. The optimal angle depends on the model and is of the order of a few degrees. The observation time is almost independent on the cone half angle in the range of a few degrees to about 10 degrees, but it increases for larger cone half angles where the signal increases slower than the background.

As shown in Fig. 6.12 for the decaying DM models, the observation time to reach the same significance decreases with the cone half angle $\theta_{\rm max}$, for $\theta_{\rm max} < 50^\circ$, and it increases only slowly for the higher cone sizes, as the signal in directions away from the GC are relatively more important.

We find that it takes, in general, shorter amount of time for the upward muon events than the contained muon ones to reach the desired detection significance. It

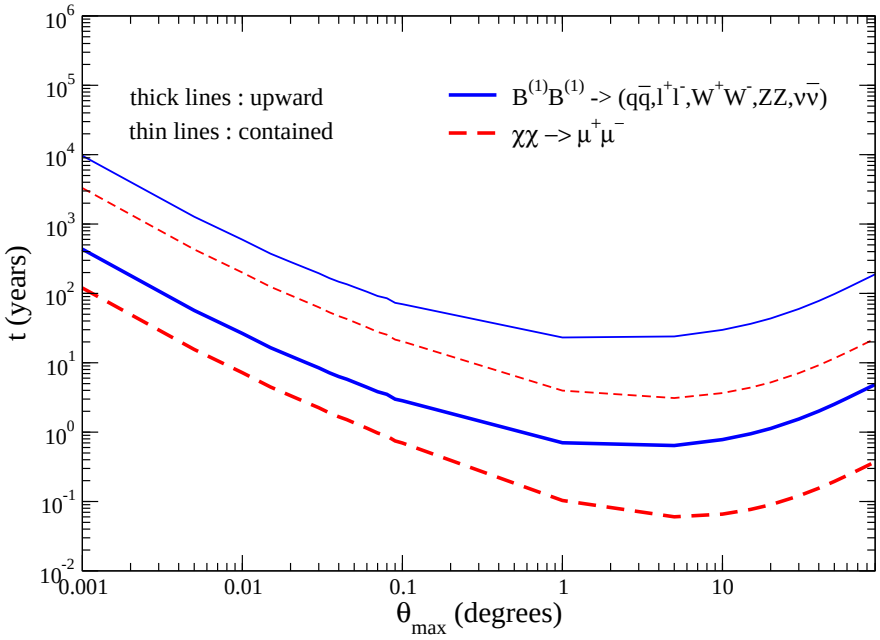

Figure 6.11: The observation time t versus cone half angle $\theta_{\rm max}$ centered at the Galactic center to reach 2σ detection significance for the upward and contained muon events produced by the muon neutrinos originated from the annihilation of DM particles. Kaluza-Klein (solid lines) and leptophilic where $\chi\chi \to \mu^+\mu^-$ (dashed lines) models are considered. We take $E_\mu^{th} = 50$ GeV.

is mostly because of the small effective volume of the detector for contained events which results in lower event rates. The background is also small in this situation, however, still longer observation times are required due to low statistics. Among all the decaying DM models that we consider, the leptophilic model ($\chi \to \mu^+\mu^-$) seems most promising for detection of DM signal at 2σ level for $\theta_{\rm max} > 20^\circ$ via upward muon events within a few years of observation.

6.1.2 Shower Fluxes

In addition to muons, the showers produced in neutrino interactions could be used as signals of DM. We obtain the shower flux and shower event rates using Eq. (4.37)

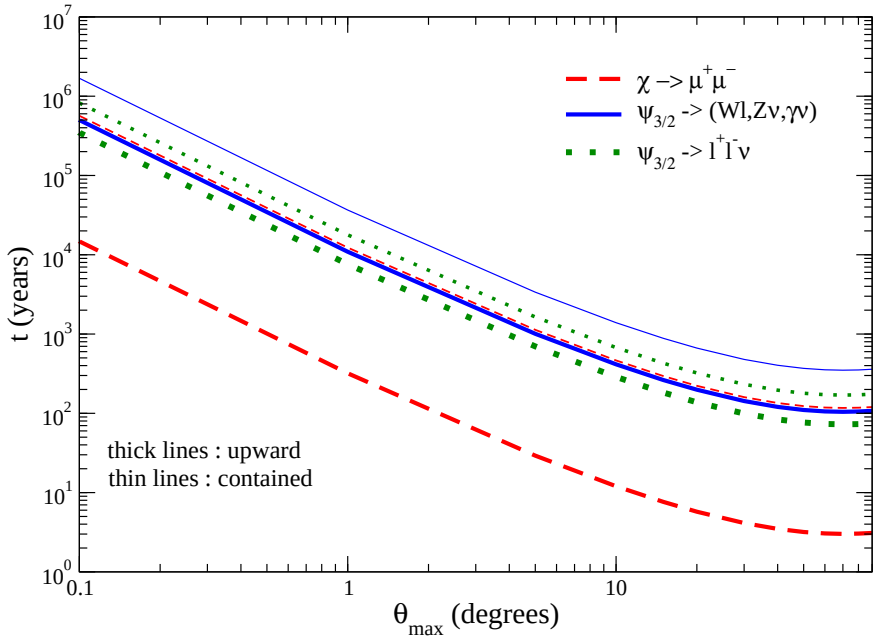

Figure 6.12: The observation time t versus cone half angle $\theta_{\rm max}$ centered at the Galactic center to reach 2σ detection significance for the upward and contained muon events produced by the muon neutrinos originated from the decaying DM particles. Decay of leptophilic where $\chi \to \mu^+\mu^-$ (dashed lines), two-body decay (solid lines) and three-body decay (dotted lines) of gravitino are considered. We take $E_\mu^{th} = 50$ GeV.

and Eq. (4.41), respectively. In our calculations, we use an energy independent IceCube+DeepCore volume whose value is $V_{\rm eff} = 0.02$ km^3 for the showers [62, 88, 149]. The detector threshold is again set to be $E_{sh}^{th} = 50$ GeV.

In Fig. 6.13. we show shower flux for the case when the DM particle is a Kaluza-Klein particle, a gravitino and for a leptophilic model, for the model parameters listed in Table 6.2. We take the cone half angle around the GC to be $\theta_{\rm max} = 50°$. The shapes of the shower fluxes are similar to the contained muon fluxes presented in Fig. 6.3. The "golden channel", $\chi\chi \to \nu\overline{\nu}$, as in the case of contained muons, contributes to the shower events at the highest kinematically allowed energy for

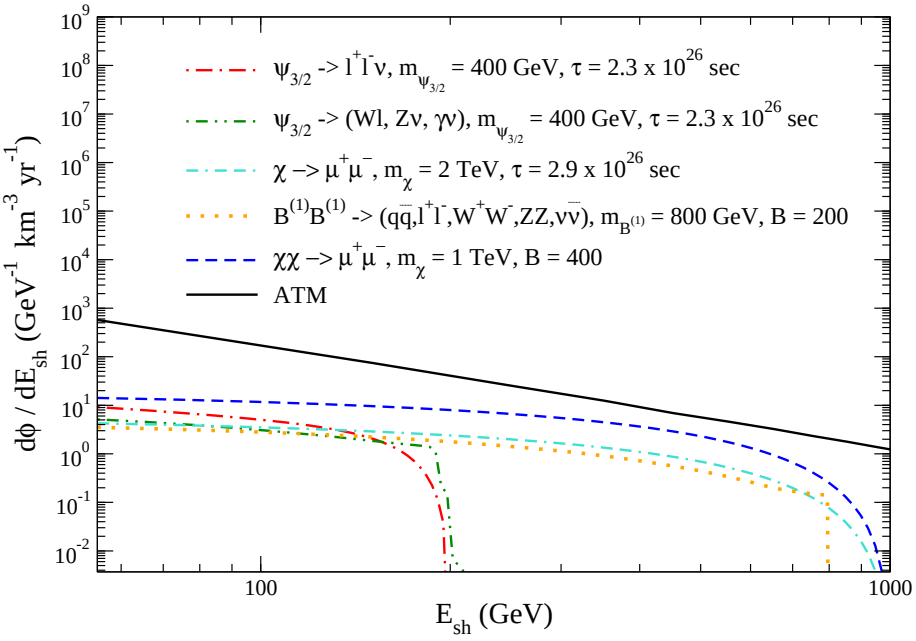

Figure 6.13: Flux for the shower events for two-body (dot-dot-dashed line) and three-body (dot-dashed line) gravitino decay, decaying leptophilic model (dash-dash-dotted line), Kaluza-Klein annihilation (dotted line) and annihilating leptophilic model (dashed line) compared with the atmospheric background (solid line), for the case when $\theta_{\rm max} = 50^\circ$. Model parameters are given in Table 6.2.

the case when the DM particle is a Kaluza-Klein particle (dotted line) and when it is a gravitino (dot-dot-dashed line). While for the case of contained muons (Fig. 6.3), DM signal in models with annihilating DM (Kaluza-Klein and leptophilic) exceeded the atmospheric background at high energies, shower signals for the same models are below the background. In addition, shower signals for the models in which DM annihilate are comparable to those in which DM decays. This is mainly due to our choice of large $\theta_{\rm max}$ for the showers ($\theta_{\rm max} = 50^\circ$). This can be seen by comparing $\langle J_2 \rangle_\Omega$ (for DM annihilation) and $\langle J_1 \rangle_\Omega$ (for DM decay) given in Eq. (4.6) for different values of the cone size. For example, $\langle J_2 \rangle_\Omega / \langle J_1 \rangle_\Omega = 75$ for $\theta_{\rm max} = 1^\circ$ whereas $\langle J_2 \rangle_\Omega / \langle J_1 \rangle_\Omega = 3$ for $\theta_{\rm max} = 50^\circ$. Furthermore, shower fluxes extend to

higher energies for the models in which DM annihilates than the case of DM decay, due to the kinematic constraints.

Table 6.4: Shower event rates per year and the time required to reach 2σ detection significance for the hadronic showers. We consider DM signals from different models described in the text. We take the effective volume to be $V_{\rm eff} = 0.02{\rm km}^3$.

	$\theta_{\rm max} = 50^\circ$	
	N_{sh}	t_{sh} (yr)
$\psi_{3/2} \to l^+l^-\nu$	11	23
$\psi_{3/2} \to (Wl, Z\nu, \gamma\nu)$	7	56
$\chi \to \mu^+\mu^-$	20	7
$B^{(1)}B^{(1)} \to (q\bar{q}, l^+l^-, \nu\bar{\nu}, ...)$	15	12
$\chi\chi \to \mu^+\mu^-$	68	0.64
ATM	676	

Using Eq. (4.41), we evaluated the shower rates which we present in Table 6.4 for a cone size of $\theta_{\rm max} = 50^\circ$ for the DM models shown in Fig. 6.13. Although the number of events for all models is relatively small compared to the atmospheric background, the number of years needed for detection of the 2σ effect is encouraging for the leptophilic model as seen in Table 6.4. We note that showers seem to be the best way to look for the signal of decaying DM.

The shower event rates depend on the DM decay time and the boost factor as an overall normalization while the dependence on DM mass is non-trivial. In order to illustrate shower event rate dependence on the DM mass, we take fixed boost factor or fixed decay time used in Fig. 6.13 for the annihilating (decaying) DM models and we obtain shower rates for different m_χ. From Fig. 6.14 we note that the shower event rate dependence on m_χ has similar behavior to to the case of contained muon events (see Fig 6.6), due to the similar flux of showers and muons in neutrino CC and NC interactions. For the case when the DM is a Kaluza-Klein particle or in the leptophilic ($\chi\chi \to \mu^+\mu^-$) model the shower rates decrease with the DM mass while for the decaying DM models it is slowly increasing with m_χ for $m_\chi < 1$ TeV and become almost m_χ independent for higher values of m_χ. For the shower events,

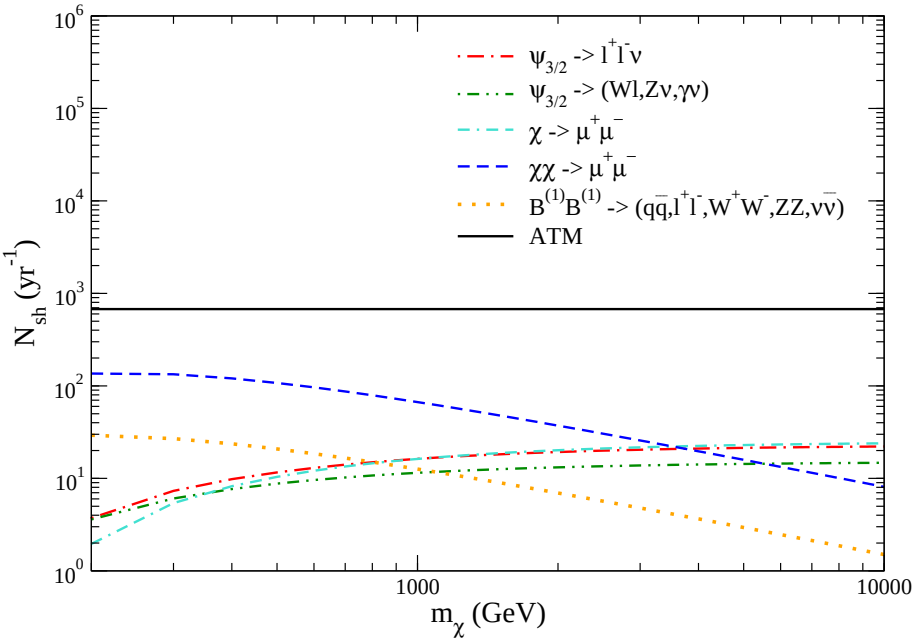

Figure 6.14: Shower event rates as a function of DM mass for models considered in Table 6.2. The boost factors for annihilating DM models and the decay times for the decaying DM models are fixed to the values in Table 6.2. We take $\theta_{\rm max} = 50^\circ$ and $E_{sh}^{th} = 50$ GeV.

the differential weak scattering cross section in Eq. (4.37) becomes higher for low shower energies so that the rates for the showers tend to increase more than those for the muons as the energy decreases. Consequently, the dependence on the choice of the detector threshold becomes more significant for the DM masses close to the threshold energy. We also note that within the cone half angle of 50° and with the chosen model parameters the rates for showers due to decaying DM models are comparable to those for the annihilating DM models. For $m_\chi > 1$ TeV ($m_\chi > 4$ TeV), the shower rates for decaying DM models are larger than for the Kaluza-Klein (leptophilic where $\chi\chi \to \mu^+\mu^-$) model.

The time required for the shower signal to be at 2σ level for different values of the cone half angle centered at the GC is presented in Fig. 6.15 for the Kaluza-

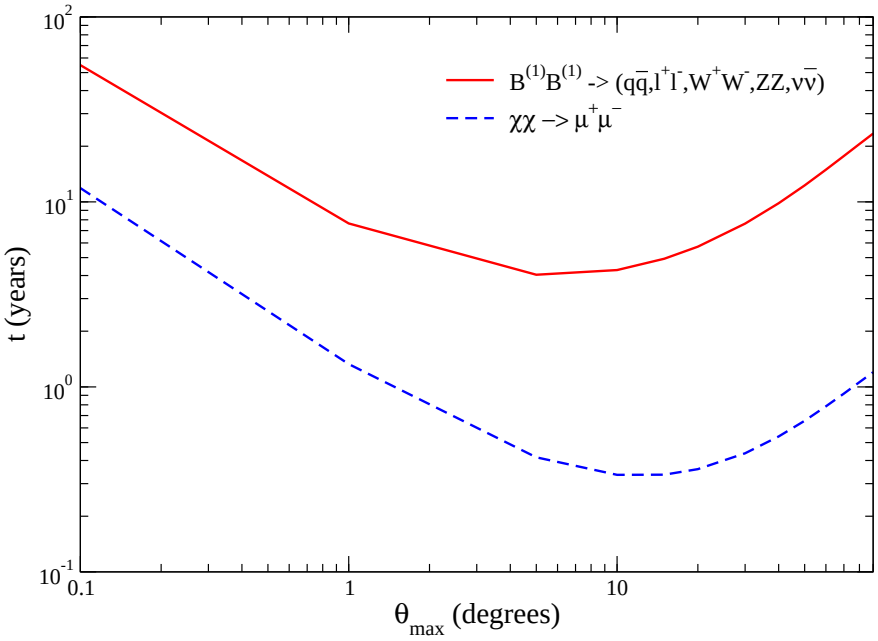

Figure 6.15: The time t versus cone half angle $\theta_{\rm max}$ centered at the Galactic center to reach 2σ detection significance for the hadronic showers produced by the neutrinos from $\chi\chi \to \mu^+\mu^-$ (dashed line) and from the Kaluza-Klein DM particle (solid line). We take $E_{sh}^{th} = 50$ GeV.

Klein DM particle (solid line) and for leptophilic model (dashed line) as example for annihilating and decaying DM models. We find that the optimum time is for the cone half angle of 4° - 10°. For leptophilic model, one could reach 2σ signal within few months of observation for $\theta_{max} = 10°$. In case of Kaluza-Klein DM particle, one needs about 4 years of data taking for $\theta_{\rm max} = 4°$. For comparison, in Fig. 6.16 we show the time needed for detection of 2σ signal for the leptophilic model when a DM particle decays (dashed line), and for gravitino two-body decay (solid line) and three-body decay (dotted line) models. The optimum angle for decaying DM models is about 50°. This is similar to the previously discussed muon signal presented in Fig. 6.12, but shower signals seem to be better for possible detection of the gravitino. This is because of better statistics with the increase in the cone half

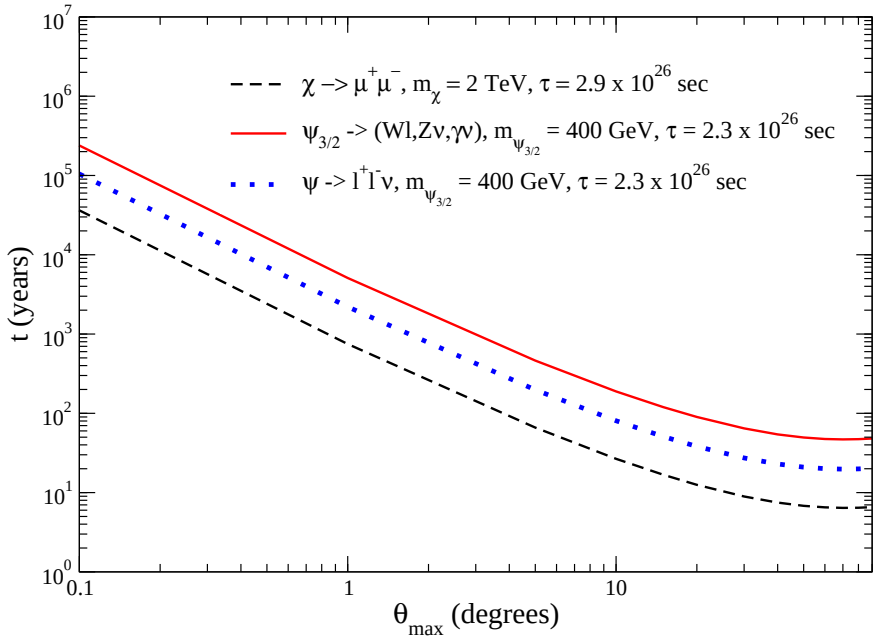

Figure 6.16: The time t versus cone half angle $\theta_{\rm max}$ centered at the Galactic center to reach 2σ detection significance for the hadronic showers produced by the neutrinos from $\chi \to \mu^+\mu^-$ (dashed line) and from the two-body (solid line) and three-body (dotted line) decay models of gravitino. We take $E_{sh}^{th} = 50$ GeV.

angle and also the inclusion of the contributions from the CC and NC interactions of the tau neutrinos and electron neutrinos with the detector medium. We note, however, that the 20 years required for $\theta \geq 50^\circ$ for these parameters is not feasible in practice.

In Fig. 6.17, we present results for DM annihilation cross section required for a given DM mass in order to reach 2σ detection significance with shower events in five years of observation within $\theta_{\rm max} = 1^\circ$. From Fig. 6.14 we note that the shower event rates decrease with m_χ for annihilating DM particles for fixed annihilation cross section, therefore the curves for DM annihilation cross section versus DM mass in Fig. 6.17 increase in order for reach 2σ effect for a given m_χ. The parameter space above the curves defines the exclusion region and the leptophilic model seems to be

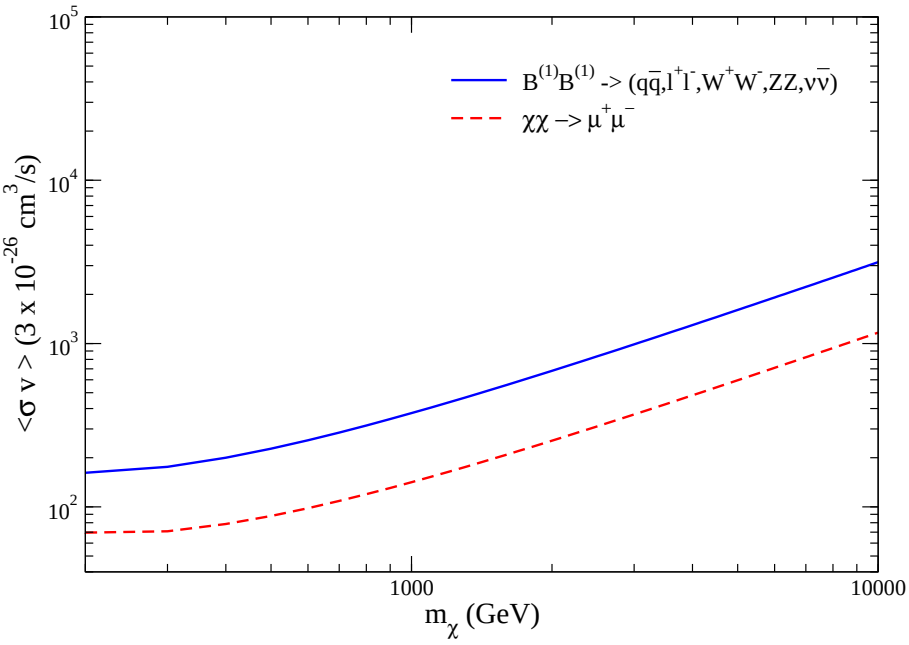

Figure 6.17: Annihilation cross section versus DM mass for shower events to reach 2σ detection significance after five years of observation for the case of Kaluza-Klein (solid lines) and leptophilic (dashed lines) models. We take $\theta_{\max} = 50^\circ$ and $E_{sh}^{th} = 50$ GeV.

more constrained than the Kaluza-Klein model. For the decaying DM models, our results for shower event rates obtained with fixed decay times (Fig. 6.14) indicate that the 2σ detection significance in five years curves for the decay time versus DM mass should increase with m_χ for $m_\chi < 1$ TeV and becomes almost flat for $m_\chi > 1$ TeV. This is shown in Fig. 6.18. In this case, the exclusion regions for the model parameters, decay time and the mass, at 2σ level in five years are the regions below the curves. For the leptophilic models with parameters that satisfy Eq. (6.2), 2σ signal detection would imply that the DM particle mass is 250 GeV in case of the annihilating DM, while for the case of the decaying leptophilic DM, the DM mass would be 3 TeV.

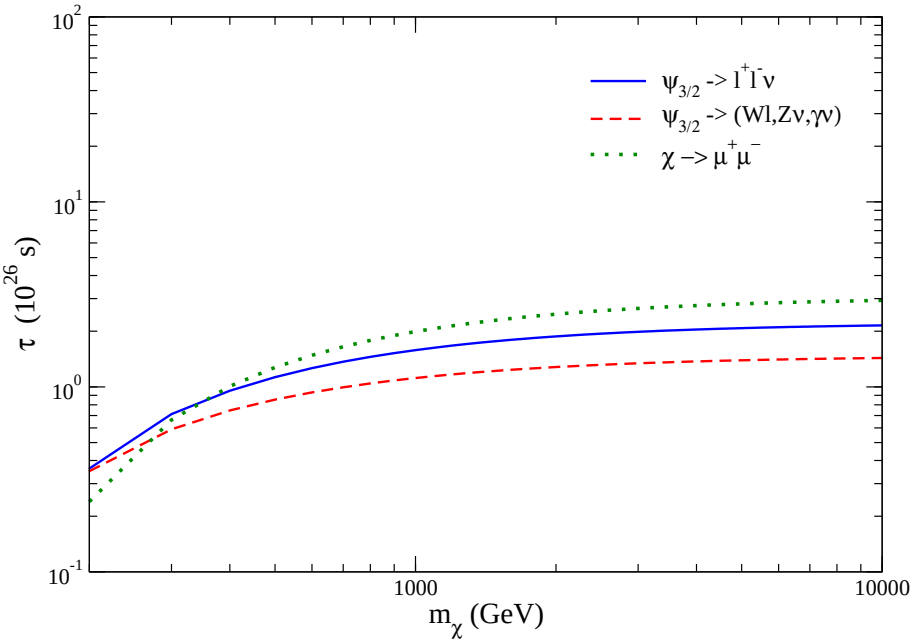

Figure 6.18: Decay time versus DM mass for shower events to reach 2σ detection significance after five years of observation for the case of decaying DM models: gravitino three-body(solid lines), gravitino three-body (dashed lines) and leptophilic (dotted lines). We take $\theta_{\rm max} = 50^\circ$ and $E_{sh}^{th} = 50$ GeV.

6.2 Parametrizations of the Muon and Shower Fluxes

Our results for the contained muon fluxes given in Fig. 6.3 can be parametrized as

$$\begin{aligned} \frac{d\phi_\mu^{ct}}{dE_\mu} &= \left(\frac{B}{100}\right)\left(\frac{\langle J_2\rangle \Delta\Omega}{1.35}\right)\frac{\xi(x)}{(m_\chi/\text{TeV})^2} \\ \frac{d\phi_\mu^{ct}}{dE_\mu} &= \left(\frac{\tau}{10^{26}\text{sec}}\right)^{-1}\left(\frac{\langle J_1\rangle \Delta\Omega}{0.018}\right)\frac{\xi(x)}{(m_\chi/\text{TeV})} \end{aligned} \tag{6.3}$$

in units of $\text{GeV}^{-1}\text{km}^{-3}\text{yr}^{-1}$ for annihilation and decay processes, respectively. The upward muon fluxes presented in Fig. 6.5 can be parametrized as

$$\begin{aligned} \frac{d\phi_\mu^{up}}{dE_\mu} &= \left(\frac{B}{100}\right)\left(\frac{\langle J_2\rangle \Delta\Omega}{1.35}\right)\frac{1}{(m_\chi/\text{TeV})}\frac{C(x)\xi(x)}{(1+1.5\frac{E_\mu}{\text{TeV}})} \\ \frac{d\phi_\mu^{up}}{dE_\mu} &= \left(\frac{\tau}{10^{26}\text{sec}}\right)^{-1}\left(\frac{\langle J_1\rangle \Delta\Omega}{0.018}\right)\frac{C(x)\xi(x)}{(1+1.5\frac{E_\mu}{\text{TeV}})}, \end{aligned} \tag{6.4}$$

in units of $\mathrm{GeV}^{-1}\mathrm{km}^{-2}\mathrm{yr}^{-1}$. Here, we define $x = E_\mu/m_\chi$ for DM annihilation and $x = 2E_\mu/m_\chi$ for the DM decay. The functions $\xi(x)$ and $C(x)$ are fitted to our results for muon fluxes and parametrizes as

$$\begin{aligned} \xi(x) &= a_1 + a_2 e^{-x} + a_3 x + a_4 x^2 + a_5 x^3 + \\ &\quad + a_6 x^4 + a_7 \ln(x) \\ C(x) &= 1 + a_8 x \ , \end{aligned} \tag{6.5}$$

with the best fit values for the parameters given in Tables 6.5 and 6.6 for the contained and upward muons, respectively.

Table 6.5: The best fit parameter values for the contained muon fluxes for different DM models.

	$\psi_{3/2}$ (three-body)	$\psi_{3/2}$ (two-body)	$\chi \to \mu^+\mu^-$	$B^{(1)}B^{(1)} \to \cdots$	$\chi\chi \to \mu^+\mu^-$
a_1	16.651	-32.032	0.0554	2.5637	0.029
a_2	-16.642	32.04	-0.0472	-2.5470	-0.0012
a_3	-16.640	32.03	-0.0472	-2.5546	-0.0012
a_4	8.242	-15.93	-0.00934	1.2381	-0.11
a_5	-2.553	5.022	0.0254	-0.3780	0.11
a_6	0.423	-0.87	-0.0069	0.06929	-0.027
$a_7(10^{-6})$	0	0	-0.0765	215.8	-0.04

The background muon flux from atmospheric neutrinos can be written in a parametric form as

$$\left(\frac{d\phi_\mu}{dE_\mu}\right)^{\mathrm{ct}}_{\mathrm{ATM,avg}} = 3186.2 \left(\frac{E_\mu}{\mathrm{GeV}}\right)^{-2.062} \left(\frac{\Delta\Omega}{10^{-3}\mathrm{sr}}\right) \tag{6.6}$$

in units of $\mathrm{GeV}^{-1}\mathrm{km}^{-3}\mathrm{yr}^{-1}$ for the contained muon events and

$$\left(\frac{d\phi_\mu}{dE_\mu}\right)^{\mathrm{up}}_{\mathrm{ATM,avg}} = 89.0 \left(\frac{E_\mu}{\mathrm{GeV}}\right)^{-1.475} \left(\frac{\Delta\Omega}{10^{-3}\mathrm{sr}}\right) \tag{6.7}$$

in units of $\mathrm{GeV}^{-1}\mathrm{km}^{-2}\mathrm{yr}^{-1}$ for the upward muon events.

Table 6.6: Same as Table 6.5 but for the upward muon fluxes.

	$\psi_{3/2}$ (three-body)	$\psi_{3/2}$ (two-body)	$\chi \to \mu^+\mu^-$	$B^{(1)}B^{(1)} \to \cdots$	$\chi\chi \to \mu^+\mu^-$
a_1	1.251	1.292	-0.7716	-3.4381	-4.60
a_2	-1.239	-1.285	0.781	3.4847	4.67
a_3	-1.266	-1.296	0.747	3.3390	4.44
a_4	0.638	0.641	-0.341	-1.5573	-2.0
a_5	-0.203	-0.196	0.0918	0.4439	0.526
a_6	0.0364	0.032	-0.0132	-0.0694	-0.073
$a_7(10^{-6})$	0	0	0.45	41.47	3.6
a_8	0.3	0.3	1.5	1.2	1.5

Our results for shower flux presented in Fig. 6.13 can be parametrized as

$$\begin{aligned} \frac{d\phi_{sh}}{dE_{sh}} &= \left(\frac{B}{100}\right)\left(\frac{\langle J_2\rangle\Delta\Omega}{27.75}\right)\frac{\xi(x)}{(m_\chi/100\text{GeV})^2} \\ \frac{d\phi_{sh}}{dE_{sh}} &= \left(\frac{\tau}{10^{26}\text{sec}}\right)^{-1}\left(\frac{\langle J_1\rangle\Delta\Omega}{8.79}\right)\frac{\xi(x)}{(m_\chi/\text{GeV})} \end{aligned} \tag{6.8}$$

in units of $\text{GeV}^{-1}\text{km}^{-3}\text{yr}^{-1}$ for DM annihilation and DM decay processes, respectively. Here, we define $x = E_{sh}/m_\chi$ for DM annihilation and $x = 2E_{sh}/m_\chi$ for the DM decay. The best fit values for the parameters is given in Table 6.7.

Table 6.7: The best fit parameter values for the shower fluxes for different DM models.

	$\psi_{3/2}$ (three-body)	$\psi_{3/2}$ (two-body)	$\chi \to \mu^+\mu^-$	$B^{(1)}B^{(1)} \to \cdots$	$\chi\chi \to \mu^+\mu^-$
a_1	-6.335	-14.129	-22.867	-8.765	-32.43
a_2	6.355	14.139	22.898	8.78	32.48
a_3	6.274	14.100	22.765	8.72	32.29
a_4	-2.991	-6.952	-11.134	-4.25	-15.79
a_5	0.813	2.127	3.325	1.25	4.71
a_6	-0.099	-0.347	-0.5125	-0.189	-0.73
$a_7(10^{-3})$	-0.472	0	0	0	0

The background shower flux from atmospheric neutrinos can be written in a parametric form as

$$\left(\frac{d\phi_{sh}}{dE_{sh}}\right)_{\rm ATM,avg} = 3.21\times10^{6}\left(\frac{E_\mu}{\rm GeV}\right)^{-2.155}\left(\frac{\Delta\Omega}{2.24{\rm sr}}\right) \tag{6.9}$$

in units of $\mathrm{GeV}^{-1}\mathrm{km}^{-3}\mathrm{yr}^{-1}$.

6.3 Summary and Discussion

We have studied neutrino signals from DM annihilation and decay in the GC assuming NFW profile as the DM density distribution in the Galaxy. We have considered models in which DM particle is a gravitino, a Kaluza-Klein particle and a particle in a leptophilic model. In case of the leptophilic model, we have considered both the case of decaying and annihilating DM. For a gravitino, we have taken into account both two-body and three-body decay channels. For each DM model, we have calculated contained and upward muons and showers using the model parameters that were obtained by fitting the excesses in γ-ray and in the positron or electron plus positron data from the observations of HESS, PAMELA and FERMI/LAT. We have used a cone half angle of 1° (50°) for the muon (shower) events. In addition, we have studied the dependence on the choice of the cone size and DM mass.

Our results are summarized in Table 6.8. The specific models which are designed to account for the lepton excesses, listed in Table 6.2, are indicated by the italic entries (highlighted in red). In addition, in Table 6.8, we show the event rates and time required for a 2σ observation for a range of masses and several values of $\theta_{\rm max}$. Note that the event rates for different $\theta_{\rm max}$ can be obtained by using rescaling of J-factors, for example $J_1(50^\circ)/J_1(10^\circ) = 9$ and $J_1(10^\circ)/J_1(1^\circ) = 50$ for decaying DM models; $J_2(50^\circ)/J_2(10^\circ) = 2.7$ and $J_2(10^\circ)/J_2(1^\circ) = 7.2$ for annihilating DM models. In Table 4.2 one can find the values of $J(\theta_{\rm max})$.

For the leptophilic model ($\chi\chi \to \mu^+\mu^-$), for example with $m_\chi = 1$ TeV and $B = 400$, the muon flux due to DM annihilation dominates over muons produced by the atmospheric neutrinos, for the muon energies in the range, 200 GeV $< E_\mu <$

Table 6.8: Summary of the results for the event rates and the time that it takes to reach 2σ effect for different values of m_χ and $\theta_{\max}$, where the threshold enery is taken as 50 GeV for both muon and shower events. In this table we do not include results which have $t > 15$ years for all m_χ. Results for the specific choice of the parameters in each model corresponding to fitting PAMELA, FERMI/LAT and HESS data are presented in red italic fonts.

		m_χ (TeV)									
		0.2	0.4	0.6	0.8	1	2	4	6	8	10
$\psi_{3/2} \to l^+l^-\nu$	$N_\mu^{ct}(50°)$	4.94	*11.15*	13.8	15.3	16.2	18.1	19.0	19.3	19.5	19.6
$B_\tau = 2.3$	$N_\mu^{up}(50°)$	8.68	*59.5*	120	180	239	503	912	1228	1485	1704
	$N_{sh}(50°)$	4	*11*	13	15	16.3	19	21	22	22	22
	$t_\mu^{up}(10°)$	1.3×10^4	*277*	69	30	17	4	1.2	0.7	0.5	0.4
	$t_\mu^{up}(50°)$	3490	*74*	18	8	5	1	0.32	0.18	0.12	0.09
	$t_{sh}(50°)$	196	*23*	16	12	10	7	6.3	5.8	5.8	5.8
$\psi_{3/2} \to (Wl, Z\nu, \gamma\nu)$	$N_\mu^{ct}(50°)$	6.1	*8.4*	8.9	9.1	9.15	9.2	9.2	9.2	9.2	9.2
$B_\tau = 2.3$	$N_\mu^{up}(50°)$	9.9	*50.9*	95.6	139	181	364	638	844	1010	1150
	$N_{sh}(50°)$	3.6	*7.66*	9.6	10.74	11.5	13.17	14.12	14.46	14.64	14.74
	$t_\mu^{up}(10°)$	1×10^4	*378*	107	51	30	7.5	2.5	1.4	1	0.8
	$t_\mu^{up}(50°)$	2693	*101*	29	14	8	2	0.7	0.4	0.3	0.2
	$t_{sh}(50°)$	210	*47*	30	24	21	16	14	13	13	13
$\chi \to \mu^+\mu^-$	$N_\mu^{ct}(50°)$	2.13	6.45	8.43	9.5	10.2	*11.5*	12.2	12.4	12.5	12.6
$B_\tau = 2.9$	$N_\mu^{up}(50°)$	3.14	29	62.3	97	131	*286*	533	728	886	1022
	$N_{sh}(50°)$	1.95	8.22	12.09	14.55	16.2	*20.2*	22.45	23.27	23.68	23.94
	$t_\mu^{up}(10°)$	1×10^5	1×10^3	252	104	57	*12*	3.5	1.9	1.3	0.97
	$t_\mu^{up}(50°)$	2.6×10^4	316	68	28	15	*3.2*	0.93	0.5	0.34	0.26
	$t_{sh}(50°)$	709	40	19	13	11	*6.9*	5.5	5.2	5	4.8
$B^{(1)}B^{(1)} \to ...$	$N_\mu^{ct}(10°)$	14.2	9.8	7.2	*5.6*	4.6	2.4	1.25	0.84	0.63	0.51
$B = 200$	$N_\mu^{up}(10°)$	86.1	131	140	*130*	128	124	108	92	81	72
	$N_{sh}(10°)$	11	9	7	*5.7*	4.8	2.6	1.4	0.9	0.7	0.6
	$t_\mu^{up}(1°)$	1.27	0.63	0.54	*0.65*	0.66	0.7	0.87	1.14	1.42	1.72
	$t_\mu^{up}(10°)$	1.55	0.68	0.57	*0.71*	0.72	0.76	1.0	1.36	1.76	2.2
	$t_\mu^{up}(50°)$	5.1	2.2	1.84	*2.29*	2.3	2.44	3.2	4.5	5.8	7.2
	$t_{sh}(1°)$	3.4	4.4	5.9	*7.7*	9.6	22	61	116	189	280
	$t_{sh}(10°)$	1.3	1.9	2.9	*4.3*	5.8	18	64	136	237	364
	$t_{sh}(50°)$	3.3	5	8	*12*	16.3	57	204	445	777	1202
$\chi\chi \to \mu^+\mu^-$	$N_\mu^{ct}(10°)$	40.19	29.58	22.01	17.39	*14.3*	7.59	3.90	2.63	1.98	1.59
$B = 400$	$N_\mu^{up}(10°)$	144	241	273	283	*320*	266	221	190	167	151
	$N_{sh}(10°)$	51.4	45.6	36.4	30	*25*	14	7.4	5	3.8	3
	$t_\mu^{ct}(1°)$	1.11	1.68	2.55	3.61	*4*	13.64	44	92	156	238
	$t_\mu^{ct}(10°)$	0.66	1.18	2.06	3.24	*4.7*	16.31	61	133	234	364
	$t_\mu^{ct}(50°)$	1.93	3.55	6.38	10.2	*15*	53	201	444	781	1213
	$t_\mu^{up}(1°)$	0.54	0.24	0.2	0.18	*0.14*	0.21	0.28	0.35	0.43	0.50
	$t_\mu^{up}(10°)$	0.47	0.21	0.16	0.15	*0.12*	0.17	0.25	0.33	0.42	0.52
	$t_\mu^{up}(50°)$	1.83	0.65	0.51	0.47	*0.37*	0.54	0.78	1.1	1.35	1.7
	$t_{sh}(1°)$	0.63	0.72	0.91	1.12	*1.37*	2.58	5.5	9	13	18
	$t_{sh}(10°)$	0.12	0.14	0.2	0.26	*0.34*	0.87	2.63	5.34	9	13.6
	$t_{sh}(50°)$	0.18	0.22	0.33	0.48	*0.7*	2.1	7.2	15.5	27	42
	ATM_μ^{ct}	2.28(1°)				227.5(10°)			5347(50°)		
	ATM_μ^{up}	28(1°)				2794(10°)			65668(50°)		
	ATM_{sh}	0.3(1°)				28.8(10°)			676(50°)		

950 GeV (50 GeV$< E_\mu <$750 GeV) for the contained (upward) muon events with cone half angle $\theta_{\max} = 1^\circ$. The shower event rates for this same model never exceed the atmospheric neutrino induced shower rates, for $\theta_{\max} = 50^\circ$, in part due to the cone size.

For $m_\chi = 800$ GeV, $B = 200$ and $\theta_{\max} = 1^\circ$, the contained muon flux due to annihilating Kaluza-Klein particles becomes larger than the background for $E_\mu >$ 300 GeV and up to the kinematic cut-off $E_\mu = m_\chi = 800$ GeV. The muon flux is comparable to the background for muon energies 200 GeV $< E_\mu <$ 400 GeV for the upward muons.

With the model parameters that we considered, the decaying DM models do not produce the muon signal (upward or contained) that is above the atmospheric background. The muon flux from the decaying DM would be comparable to those for the annihilating DM models only if the decay times were of the order $\sim 10^{25}$ sec and $\sim 10^{24}$ sec for contained muon and upward muon events, respectively. In contrast to the muon case, we find that for a wide range of shower energies, the shower flux for decaying leptophilic particle ($\chi \to \mu^+\mu^-$) is larger than for annihilating Kaluza-Klein particle.

We have also calculated the total muon and shower event rates by folding the corresponding fluxes with the energy independent IceCube+DeepCore effective volume, i.e $V_{\text{eff}} = 0.04(0.02)$ km^3 for the contained muon (shower) events. Due to its location IceCube detector is unable to study the upward muons produced by the neutrinos coming from the GC. However, we have calculated the upward muon rates for the IceCube-type detector in the Northern hemisphere by folding the muon fluxes with a muon effective area, which is assumed to be $A_{\text{eff}} = 1$ km^2.

Even if there is a significant signal to background ratio, low statistics may yield difficulties in confirming the presence of a DM signal via neutrinos. Thus, we have evaluated how many years it would take to observe 2σ effect. Using our results for the muon and shower event rates, we have also obtained the contour exclusion plots in which we show the regions for the model parameter space for each DM model in the case of no signal detection at 2σ detection significance in five years.

We find that the leptophilic model ($\chi\chi \rightarrow \mu^+\mu^-$) has stronger constraints on DM annihilation cross section (or the boost factor) and m_χ than the case of the Kaluza-Klein particle. In terms of the constraint on the annihilation cross section, for the leptophilic DM model where the boost factor and DM mass are related by Eq. (6.2), after five years, the range of $m_\chi > 250$ GeV would be excluded by upward muon events for $A_{\rm eff} = 1$ km^2 and events within a cone half angle of $\theta_{\rm max} = 1^\circ$. A similar limit is obtained from the shower rate as well. More generally, we find that the upward muon and the shower events are more constraining than the contained muon ones. If there is no upward muon signal detected in five years, with $\theta_{\rm max} = 10^\circ$, for the decaying leptophilic model ($\chi \rightarrow \mu^+\mu^-$) which satisfies the constraint given by Eq. (6.2), m_χ is constrained to be smaller than 3 TeV.

In our calculations, we have taken the detector muon and shower energy thresholds to be 50 GeV. Changing the detector threshold energy to about 100 GeV does not affect our results significantly. However, decreasing the threshold energy down to ~ 10 GeV results in a larger atmospheric background relative to the DM signal. Consequently, detecting a DM signal via muon or shower events with low detector thresholds (~ 10 GeV) becomes more difficult.

Increasing the cone half angle, $\theta_{\rm max}$ about the GC increases the DM signal, however it does not necessarily improve the detection significance since the background signal due to atmospheric neutrinos is also enhanced. We have found the optimum cone half angles for all types of events in order to reach 2σ detection level. For the annihilating DM models, we have found the optimum angle to be a few degree for the muon events and about 10° for the shower events. In both cases, we have shown that there is a good chance of detecting both leptophilic and Kaluza-Klein particles in less than ten years for some DM masses.

In the case of the decaying DM models, the optimum angle is about 50° for both muons and showers. For gravitino DM, signals could be detected in ten years only with shower events, while the decaying leptophilic particle can be detected with upward muon events as well in few years.

Our results with fixed annihilation cross section or decay time and variable DM

mass can be used to predict neutrino signals for any other values for the parameters of the models we consider. For example, in the literature, the HESS data is also explained by a hypothetical Kaluza-Klein particle with mass $m_\chi = 10$ TeV [74]. The boost factor that is required, in this case, is $B = 1000$. By rescaling the results in the previous sections, we find that the observation time to reach 2σ detection significance becomes 0.1 years for the upward muon events. For contained muons and showers, it is not feasible to detect 2σ effect within reasonable time ($t \gg 20$ years). Increasing the boost factor by a factor of 5 and the DM mass by a factor of about 10 relative to the parameters of Table 6.2 significantly improves the chance for detecting the Kaluza-Klein particle via upward muon events.

Similar to the decaying leptophilic model, the gravitino model ($\psi_{3/2} \to l^+ l^- \nu$) with a gravitino mass of 3.3 TeV and decay time $\tau = 5 \times 10^{25}$ sec can also account for the FERMI data [86]. For a decaying DM particle, increasing the DM mass (for a fixed decay time) increases the event rates. Since the neutrino flux scales as $\sim \tau^{-1}$ (see Eq. (4.8)), decreasing the decay time also enhances the neutrino signals for a decaying DM particle. Therefore, combination of higher mass and shorter decay time should increase all the event rates that we have calculated for a lighter ($m_{\psi_{3/2}} = 400$ GeV) gravitino particle which has a longer decay time ($\tau = 2.3 \times 10^{26}$ sec). For the model parameters, $m_\chi = 3.3$ TeV and $\tau = 5 \times 10^{25}$ sec we find that the 2σ detection significance can be reached in 2.6 years via upward muons and in less than a year via the hadronic showers. In addition, for the contained muons the observation time decreases by two orders of magnitude relative to the value given in Table 6.3.

The dependence of the signal on the cone half angle is different for the annihilating DM particles than for the decaying DM particles. We have demonstrated this by choosing wedges between $\theta_{\max} - 1^\circ$ and $\theta_{\max}$ centered at the GC and calculating $\langle J_n \rangle_\Omega \Delta\Omega$, which defines an overall normalization for the neutrino signals, for different $\theta_{\max}$ for both annihilating and decaying DM particles. The angular wedges can be used to rescale event rates as well. Our results indicate that the J factor for annihilating DM particle decreases sharply with $\theta_{\max}$ whereas for the case

of decaying DM particle, for a wide range of $\theta_{\rm max}$, the J factor has a weak $\theta_{\rm max}$ dependence. In determining the nature of the DM (annihilating or decaying), the directional dependence of the neutrino signals gives valuable information.

CHAPTER 7

CONCLUSION

The DM has been a very intriguing topic in the field of both astrophysics and particle physics. Its presence has been confirmed by many independent experiments over the last seven decades. Interestingly, current data imply that it is five times more prevalent than ordinary matter and composes about the quarter of the density of the Universe. All of the evidence collected so far is based on its gravitational interactions. However, no useful information has been found to pinpoint what the nature of this mysterious form of matter is. Unraveling the properties of DM would help understand how the structure forms and impacts the evolution of the Universe from past to present and to future in astrophysics and would help explore the physics beyond the SM in elementary particle physics.

The detection of DM is a very challenging task. Independent but complementary experiments including the direct and indirect searches are carried out in the Earth-based and space-based detectors. Among the indirect searches, neutrino astronomy also plays a crucial role in the quest of DM and the future kilometer scale neutrino telescopes will be extremely useful to discover DM or to put stringent bounds on the properties of DM. This study presents a comprehensive picture of DM detection via neutrino signals in the large-scale ice or water based neutrino detectors.

So far, the present neutrino telescopes have observed only the expected atmospheric neutrino background which falls dramatically with increasing energy. The future large-scale neutrino telescopes with energy thresholds of 100 GeV will open up a range of energies to be probed where the background is negligible. As we have pointed out in this study, the energy distributions of final muon fluxes can give a clear evidence for the presence of DM above these threshold energies. In addition, the shape of the energy distributions can also help in distinguishing which SM particles DM annihilates into. The typical discovery channel, the so-called "golden channel"

where the DM annihilates or decays directly into neutrinos, produces monoenergetic neutrinos with energies of the order of DM mass. These neutrinos exhibit a delta function behavior in their spectra, however, due to smearing, the final muon flux (for upward or contained muon events) shows a continuous distribution with a high energy cutoff. For the contained muon events, the muon flux increases with increasing muon energy which is a unique signature. Thus, "golden channel" becomes apparent in contained muon events.

We have presented results for upward and contained muon and shower fluxes in the neutrino detectors due to DM annihilation/decay in the cores of the astrophysical objects (Earth and Sun) or in the Galaxy. Independent of the location for the direct neutrino production from DM, we have found that the contained muon flux observed in a kilometer size detector exceeds the upward muon one in the range $E_\mu \geq 0.6 m_\chi$ for a given DM mass, m_χ. In terms of total rates from $\chi\chi \rightarrow \nu\bar{\nu}$ in a kilometer scale detector ($A_{eff} = 1\text{km}^2$ for the upward muon and $V_{eff} = 1\text{km}^3$ for the contained muon events), the upward muon events dominate over the contained muon events for $m_\chi > 600(700)$ GeV for the DM signals from GC (from the core of the Earth or the Sun). We have also obtained relative normalizations for the neutrino fluxes due to DM annihilations in GC and due to DM annihilations in the core of the Earth/Sun.

In addition to the shape of the final muon fluxes, we have also studied the dependence of the DM signals from GC on the choice of the density profile, the size of the region about the GC (i.e, the choice of the cone half angle), the nature of DM (annihilating or decaying), and the physical processes such as Sommerfeld effect that cause a significant enhancement (which is quantified as the boost factor in our calculations) in the signal. In addition to the Sommerfeld effect, there may also be potential enhancement of the DM signal due to the existence of small substructures in the Galactic halo [124]. The observation of this additional enhancement may be difficult because of the small population of these substructures unless the neutrino detectors have a very good angular resolution [66]. For a neutrino detector with good angular resolution, to decrease cone half angle in search of Galactic DM significantly

reduces the atmospheric background, however, low statistics make it difficult to confirm the detection of a signal. Therefore, the required time to reach the desired detection significance is a function of cone half angle.

We have shown that the muon rates (both contained and upward) can dominate significantly over the atmospheric background when the boost factor is $B = 200$ for the cone half angles less than 10°. We have noted that signal to background ratios larger than the case for the muon events can be achieved with the shower events for the neutrino energies above 100 GeV. This is due to the suppression of the atmospheric tau and electron neutrino fluxes relative to the atmospheric muon neutrino flux. In this case the main background comes from the NC interactions of the atmospheric muon neutrinos with the detector medium whose cross section is about a factor of three less than the CC one. We have also considered the detection of DM signals from GC in the form of contained muon (shower) events in the IceCube+DeepCore detector which has an effective volume of 0.04 (0.02) km^3. We have shown that after one year IceCube+DeepCore detector could potentially observe a 5σ effect by measuring contained muons (for the $\chi\chi \rightarrow \nu\bar{\nu}$ channel), or in five to eight years a 2σ signal level with hadronic showers even in the case when they are due to secondary neutrinos.

We have also studied the neutrino signals from gravitino, Kaluza-Klein and leptophilic DM particles (with the model parameters given in Table 6.2) used in the literature to explain the data from several indirect searches looking for DM in the Galaxy. We have shown that for the annihilating DM models both muon track-like events and shower events look promising for discovery in a few years of observation whereas for the decaying DM models only shower events give reasonable detection significances for the same observation time. This is mainly due to the fact that the signal level depends on the square of the DM density in the case for annihilating DM whereas the signal from decaying DM is linearly proportional to the density. In the analysis of finding the shortest observation time to reach a 2σ detection significance for each DM model, we have shown that for the muon (shower) events, the optimal cone half angle is around $4^\circ - 10^\circ$ (50°). With the choice of these op-

timal angles, we have found the parameter space probed for each DM model with five years of observation. We have shown that in the study of neutrino signals due to DM annihilation/decay in the Galaxy, the upward muon events observed in a hypothetical kilometer size detector located in Northern Hemisphere are more constraining than the contained muon events observed in IceCube+DeepCore. However, shower events in IceCube+DeepCore would be complementary to the upward muon events observed in the kilometer-scale hypothetical detector in constraining the model parameters.

To provide a simple way for other studies, we have parametrized our results and also derived analytical expressions for the muon and shower fluxes for given decay channels. Our results in this study are relevant to future large-scale neutrino detectors. IceCube detector with its sub-detector DeepCore will be fully operational in the near future. The GC stays above the horizon throughout the year for an observer on the South Pole. Therefore, for the DM signals from the GC, IceCube+DeepCore will be able to analyze only contained muon and shower events. Due to its location in the northern hemisphere, the future KM3NeT experiment will be complementary to IceCube+DeepCore in searching for neutrino signals from DM annihilation in the GC through the observation of upward muon events. The atmospheric muon background at the KM3NeT will be suppressed significantly since the Earth will act as a shield to the atmospheric muons. Independent searches of the upward muon events by KM3NeT and the contained muon and shower events by IceCube+DeepCore look promising for the discovery of the mysterious DM particle.

APPENDIX A

COLD DARK MATTER IN STANDARD COSMOLOGY

The uniformity principles (homogeneity and isotropy) in cosmological models constitute the cosmological principle which implies that there is not any preferred spatial location or a preferred direction for an observer in space [13]. The general space-time metric, $g_{\mu\nu}$, obtained by using the cosmological principle is called the Friedmann-Lemaitre metric which suggests that the line-element takes the form

$$ds^2 = -dt^2 + a^2(t)\left(\frac{dr^2}{1-Kr^2} + r^2 d\Omega^2\right). \tag{A.1}$$

Here, the term in parenthesis describes the spatial metric in comoving coordinates where the cosmic time, t, appears only in the scale factor $a(t)$. The quantity, K, in this metric is a pure number which prescribes the spatial curvature. For a flat space, $K = 0$. In the physical space, the separation of two comoving observers with trajectories $\vec{x}_1$ and $\vec{x}_2$ is given by

$$\vec{r}_{12} = a(t)(\vec{x}_1 - \vec{x}_2) \tag{A.2}$$

which leads to

$$\dot{\vec{r}}_{12} = H\vec{r}_{12}\ , \tag{A.3}$$

where the dot represents the derivative with respect to the cosmic time, t and the quantity $H = \dot{a}/a$ is the Hubble parameter. Then, the above relations suggest that the farther the observers are from each other, the greater is their relative velocity. This is called the Hubble law. Clearly, H is time dependent and several different observations (see Ref. [13] for a review) suggest that its present value is

$$H_\circ = 100h\ \ \mathrm{kms}^{-1}\mathrm{Mpc}^{-1} \tag{A.4}$$

where $h \sim 0.7$ suggesting the expansion of the Universe. In addition to the metric which can be used to obtain the terms on the left hand side of Einstein's equations

$$G_{\mu\nu} + \Lambda g_{\mu\nu} = \kappa T_{\mu\nu}, \tag{A.5}$$

the energy-momentum tensor $T_{\mu\nu}$ is also needed to obtain the relations between the cosmological parameters. Here, Λ is the cosmological constant, $\kappa = 8\pi G_N$ and G_N is the Newton constant. The most general form for the energy momentum tensor is fixed by the cosmological principle as

$$T_{\mu\nu} = (P + \rho)u_\mu u_\nu + P g_{\mu\nu} \tag{A.6}$$

where the only freedom is the choice of the equation of state, i.e., the relation between the pressure P and the energy density ρ. Consequently, the Einstein equations reduce to

$$H^2 = \frac{\kappa}{3}\rho - \frac{K}{a^2} + \frac{\Lambda}{3}. \tag{A.7}$$

and

$$\frac{\ddot{a}}{a} = -\frac{\kappa}{6}(\rho + 3P) + \frac{\Lambda}{3} \tag{A.8}$$

which are called Friedmann equations. One can also introduce the energy density parameters as

$$\Omega = \frac{\kappa\rho}{3H^2}, \quad \Omega_\Lambda = \frac{\Lambda}{3H^2}, \quad \Omega_K = -\frac{K}{H^2 a^2} \tag{A.9}$$

for the matter, the cosmological constant and the curvature, respectively. The matter term can be decomposed as a sum of different components (e.g photons, neutrinos, baryons (b), dark matter (χ), etc.), i.e $\Omega = \sum_X \Omega_X$ where $\Omega_X = \frac{\kappa\rho_X}{3H^2}$. Then, Eq. (A.7) can be written as

$$\sum_X \Omega_X + \Omega_\Lambda + \Omega_K = 1. \tag{A.10}$$

In the flat ($K = 0$) ΛCDM model, for the late time evolution the space is dominated by the pressureless ($P = 0$) fluid and the cosmological constant, Λ. In this model,

using Eq. (A.8), one can find that the present values for the density parameters $\Omega_{m\circ}$ and $\Omega_{\Lambda\circ}$ satisfy

$$\frac{\ddot{a}_\circ}{a_\circ H_\circ^2} = \Omega_{\Lambda\circ} - \frac{1}{2}\Omega_{m\circ} \tag{A.11}$$

where the term $\Omega_{m\circ}$ includes only the contributions from baryons and dark matter since the contribution from radiation is negligible today.

A.1 Observations and Constraints on the Cosmological Parameters

In the search for the cosmological parameters including the Hubble parameter, the Supernova Cosmology Project (SCP) [8] and the High-Z Supernova Search Team (HZT) [9] teams have put constraints on $\Omega_{m\circ}$ and $\Omega_{\Lambda\circ}$. The analysis of both teams shows that

$$\frac{\ddot{a}_\circ}{a_\circ H_\circ^2} > 0 \tag{A.12}$$

which implies that $\Omega_{\Lambda\circ} > \frac{1}{2}\Omega_{m\circ}$ in the ΛCDM model (see Eq. (A.11)). Moreover, the best fit parameter values turn out to be constrained by

$$8\Omega_{m\circ} - 6\Omega_{\Lambda\circ} \simeq -2 \mp 1 \tag{A.13}$$

according to their data.

Furthermore, the data from the cosmological microwave background searches conducted by WMAP[10, 11] and baryon acoustic oscillations (BAOs) observed by the Sloan Digital Sky Survey (SDSS) [12] put additional constraints on the cosmological parameters. The combined data of all these searches indicate that for a ΛCDM Universe, the best fit values for the cosmological parameters are given by [10, 11]

$$\begin{aligned} \Omega_\chi h^2 &\simeq 0.1131 \mp 0.0034 \\ \Omega_{\rm b} h^2 &\simeq 0.02267 \mp 0.0006 \end{aligned}$$

$$\begin{aligned} \Omega_\Lambda &\simeq 0.726 \mp 0.015 \\ H_\circ &\simeq 70.5 \mp 1.3 \text{ km s}^{-1}\text{Mpc}^{-1} . \end{aligned} \tag{A.14}$$

A.2 Particles in Thermodynamic Equilibrium

After giving a brief presentation of ΛCDM cosmology, we will now study the properties of particles in the early Universe, where the Universe is dominated by radiation. To describe physical processes in the radiation-dominated era the particle distributions should be determined. The particles present in the early Universe can be considered to have interaction rates larger than the Hubble expansion rate, maintaining them in thermodynamic equilibrium with the radiation field at a temperature T. In the thermodynamic equilibrium at temperature T, the particles can be treated as perfect Bose-Einstein and Dirac-Fermi gases whose distributions are given as

$$F_i(E,T) = \frac{g_i}{(2\pi)^3}\frac{1}{exp[(E-\mu_i)/T_i(t)] \pm 1} \equiv \frac{g_i}{(2\pi)^3} f_i(E,T) \tag{A.15}$$

where g_i is the degeneracy, μ_i is the chemical potential and E is the energy ($E^2 = p^2 + m^2$) of the particle species i. The distribution functions are used to define some macroscopic quantities such as the particle number density, n, energy density ρ and pressure P:

$$\begin{aligned} n_i(T) &= \int F_i(p,T) d^3p \\ \rho_i(T) &= \int F_i(p,T) E(p) d^3p \\ P_i(T) &= \int F_i(p,T) \frac{p^2}{3E} d^3p. \end{aligned} \tag{A.16}$$

The values of these quantities in the limits $T \gg m, \mu$ and $T \ll m$ for fermions (F) and bosons (B) are given in Table A.1 where $\zeta(3) \simeq 1.202$ is the value of the Riemann zeta function at 3.

In the regime where the matter content is dominated by radiation, the radiation

Table A.1: Number density (n), energy density (ρ) and pressure (P) for fermions (F) and bosons (B) in thermodynamic equilibrium. Certain limits are considered.

limit	particle	n	ρ	P
T$\gg m, \mu$	B	$g(\zeta(3)/\pi^2)T^3$	$(\pi^2/30)gT^4$	$\rho/3$
	F	$g(3\zeta(3)/4\pi^2)T^3$	$(7\pi^2/(8\times 30))gT^4$	$\rho/3$
T$\ll m$	B,F	$g(mT/2\pi)^{3/2}e^{(\mu-m)/T}$	$(m+3T/2)n$	nT

density at a given temperature reads

$$\rho(T) = g_*(T)\left(\frac{\pi^2}{30}\right)T^4 \tag{A.17}$$

where g_* represents the relativistic degrees of freedom at that temperature

$$g_*(T) = \sum_{i=bosons} g_i\left(\frac{T_i}{T}\right)^4 + \frac{7}{8}\sum_{i=fermions} g_i\left(\frac{T_i}{T}\right)^4 \tag{A.18}$$

From the first law of thermodynamics, $TdS = d(\rho a^3) + Pda^3$ as long as particles are neither created nor destroyed. The quantity, S is the entropy. Then, for a given temperature T, the entropy is given as

$$S = sa^3 = \frac{\rho + P}{T} = \frac{4\rho a^3}{3T} \tag{A.19}$$

where s is defined as the entropy density. Then,

$$s = \frac{2\pi^2}{45}q_*T^3 \tag{A.20}$$

and

$$q_*(T) = \sum_{i=bosons} g_i\left(\frac{T_i}{T}\right)^3 + \frac{7}{8}\sum_{i=fermions} g_i\left(\frac{T_i}{T}\right)^3 \tag{A.21}$$

As a consequence, we observe that if all the relativistic particles are at the same temperature $T_i = T$, then $q_* = g_*$. Hence, we also notice that in the radiation era, the Friedmann equation reduces to

$$H^2 = \frac{8\pi G_N}{3}g_*\left(\frac{\pi^2}{30}\right)T^4 \tag{A.22}$$

which shows that the Hubble parameter, H scales as $H \propto T^2$.

A.3 Particle Freeze-Out

Interaction of particles are in general characterized by the reaction rate, Γ which is directly proportional to the cross section (σ) and the number density (n), i.e $\Gamma \sim n\sigma$. The particles are considered to be in thermodynamic equilibrium at a temperature T as long as this reaction rate is larger than the Hubble expansion rate. Since all the interacting particles have the same temperature, T must be equal to the photon temperature, T_γ, for those which interact with the persistent background radiation field in the Universe. That is why it is not surprising that the photon temperature is often called the temperature of the Universe. For the cases when the cross section scales as $\sigma \sim E^{\rm n} \sim T^{\rm n}$, then $\Gamma \sim T^{\rm n+3}$. In the previous section, we see that $H \sim T^2$ in the radiation period. Thus, if n+1>0, there will always be a temperature T_f below which the reaction is no longer efficient for the given species and they can not be kept in equilibrium with the other components. This mechanism is called "decoupling". As an example, for a stable massive particle X which is in thermodynamic equilibrium with its antiparticle $\bar{X}$, its density is determined by the annihilation and the inverse annihilation of the form

$$X + \bar{X} \leftrightarrow l + \bar{l}\,. \tag{A.23}$$

If it had never decoupled from the thermal bath until today, its number density n_X would have been completely negligible due to the exponential suppression, $n_X \propto exp(-m/T)$. However, in an expanding Universe, the annihilation is not expected to last indefinitely and freeze out occurs at some temperature T_f at which the massive particle becomes a relic.

A.3.1 Evolution of the particle distributions and densities

To describe the decoupling, or the freeze-out of an interaction, is a very complex problem. After decoupling, the particles no longer stay in thermodynamic equilibrium with the background radiation. Thus, the distribution functions are not simple functions of only temperature for the decoupled particles. Since the thermalization

is not that effective, the Hubble expansion reduces their number density. However, the number density is not affected by the temperature changes which introduces $exp(-m/T)$ suppression for the particles in thermodynamic equilibrium. In practice, the evolution of the particle density for the decoupled particles is obtained from the Boltzmann equation which, in a homogeneous and isotropic space-time reduces to

$$\dot{n}_i + 3Hn_i = C_i \tag{A.24}$$

where the left hand side of the equation is the total time rate of change of the number density which includes the Hubble expansion and the right hand side describes the particle interactions. Here, the difficult part lies in the modeling of the collision term C_i which for the type of interaction

$$i + j \leftrightarrow k + l \tag{A.25}$$

is given as

$$C_i = - < \sigma v > (n_i n_j - \bar{n}_i \bar{n}_j) \tag{A.26}$$

where $\bar{n}$ denotes the values in thermodynamic equilibrium. This implies when the particle species is in chemical equilibrium, $C_i = 0$, or equivalently the particle number density per comoving volume is constant $d(n_i a^3) = 0$. Here, the term $< \sigma v >$ is defined as the thermal-averaged annihilation cross section. In order to find the particle number densities, we consider the type of reaction given in Eq.(A.23), assuming that X is its own anti-particle. After defining $Y_X = n_X/s$, the conservation of entropy ($d(sa^3) = 0$) implies that

$$\dot{n}_X + 3Hn_X = s\dot{Y}_X \tag{A.27}$$

so that for the X particles we obain

$$\dot{Y}_X = - < \sigma v > s(Y_X^2 - \bar{Y}_X^2) \tag{A.28}$$

Defining $\Delta = Y_X - \bar{Y}_X$ and $x = m/T$, and using the expressions for H and s from the previous section, the final form of the equation is obtained

$$\frac{d\Delta}{dx} = -\frac{d\bar{Y}_X}{dx} - \lambda x^{-2} \Delta(\Delta + 2\bar{Y}_X) \tag{A.29}$$

with

$$\lambda =< \sigma v > \sqrt{\frac{\pi}{45}} \frac{q_*}{g_*^{1/2}} m M_P \tag{A.30}$$

where $M_P = 1/\sqrt{G_N}$.

A.3.2 Cold Relic Density

The dark matter searches which are presented in this study suggest the existence of massive cold dark matter relics in the Universe. Thus, this section is devoted to present the calculation of the present number densities of the cold relics relying on the above mentioned theoretical framework. For cold relics, it is assumed that the decoupling occurs at the freeze-out temperature, T_f when the particle is non-relativistic, $x_f = m/T_f > 1$. From the previous results (see Table (A.1) and Eq. (A.20)) it is easy to show that

$$\bar{Y}_X = \frac{45}{2\pi^4} \sqrt{\frac{\pi}{8}} \frac{g_X}{q_*} x^{3/2} e^{-x} \ . \tag{A.31}$$

Although the solution to Eq. (A.29) requires numerical analysis, one can obtain some limiting behaviors. For example, a long time after decoupling ($x \gg x_f$), $\bar{Y}_X$ decreases exponentially and becomes negligible, so that $Y_X \sim \Delta$ and the equation takes the form

$$\frac{d\Delta}{dx} = -\lambda \frac{\Delta^2}{x^2} \tag{A.32}$$

which can be integrated from $x = x_f$ to $x = \infty$ to get

$$Y_\infty \simeq \left[\int_{x_f}^{\infty} \frac{\lambda}{x^2} dx \right]^{-1} \ , \tag{A.33}$$

where x_f can be determined by using $\Gamma(x_f) = H(x_f)$, which leads to

$$\frac{g_X}{g_*^{1/2}} x_f^{1/2} e^{-x_f} < \sigma v > m M_P = 4\pi^3 \sqrt{\frac{2}{45}}. \tag{A.34}$$

So, using the entropy density of the today's Universe

$$s_\circ = 7.039 \left(\frac{q_{*\circ}}{3.91} \right) n_{\gamma\circ} \tag{A.35}$$

and assuming $q_*(x_f) \simeq g_*(x_f)$, the relic density of the particle X, $n_{X\circ} = s_\circ Y_\infty$ can be estimated as

$$n_{X\circ} = \frac{1.09 \times 10^4}{\sqrt{g_*}} \left(\frac{q_{*\circ}}{3.91}\right) \left(\frac{T_\circ}{2.725\mathrm{K}}\right)^3 \frac{\left(\int_{x_f}^{\infty} < \sigma v > /x^2 dx\right)^{-1}}{mM_P} \mathrm{cm}^{-3} \,. \tag{A.36}$$

It is also convenient to express this result in terms of the density parameter of X, $\Omega_X = \rho_X/\rho_{crit} = mn_{X\circ}/\rho_{crit}$ where the critical density of the Universe is $\rho_{crit} = 3H^2/(8\pi G_N)$. Using the current value of the Hubble parameter $H = 100h$ km s^{-1} Mpc^{-1} (where $h \sim 0.7$), the number of relativistic degrees of freedom $q_{*\circ} = 3.91$, the temperature of the Universe $T_\circ = 2.725$ K, assuming $g_*(x_f) \simeq 100$ and approximating the annihilation cross section with a non-relativistic expansion, i.e $< \sigma v >= a + b < v^2 > +... \simeq a + 6\, b/x$, we get

$$\Omega_{X\circ} h^2 = 0.0031 x_f \left(\frac{a + 3b/x_f}{3 \times 10^{-26} \mathrm{cm}^3/\mathrm{s}}\right)^{-1} \tag{A.37}$$

or if $x_f \simeq 30$ which is a typical value from the numerical simulations,

$$\Omega_{X\circ} h^2 \simeq 0.1 \left(\frac{a + b/10}{3 \times 10^{-26} \mathrm{cm}^3/\mathrm{s}}\right)^{-1} \,. \tag{A.38}$$

It is worth to note that the smaller the annihilation cross section, the greater is the relic abundance. The present value of the relic abundance depends only on the annihilation cross section at freeze out which for the s-wave annihilation is independent of the temperature or energy. Fig. (A.1) shows the evolution of Y_X compared with the equilibrium value $\bar{Y}_X$ for different annihilation cross sections for the case of p-wave annihilation ($a = 0$ and $b \neq 0$).

Several independent observations which are discussed in the introduction support the cold dark matter (χ) scenario with a density parameter $\Omega_{\chi\circ} h^2 \simeq 0.1$. According to Eq. (A.38), any dark matter model which satisfies $< \sigma v >= 3 \times 10^{-26}$ cm^3/s at freeze out could be a plausible explanation for the dark matter problem in physics.

On dimensional grounds, for a generic weak-scale particle which annihilates through the exchange of electroweak gauge or Higgs bosons, the annihilation cross section is expected to be

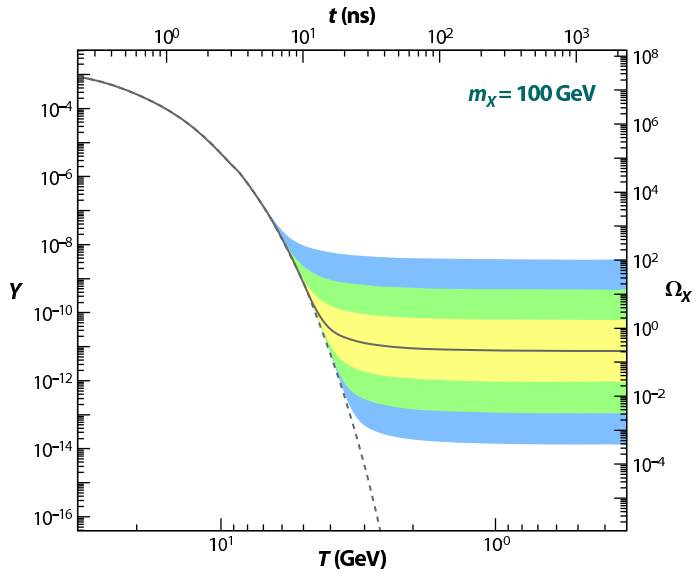

Figure A.1: From [14]. The thermal relic density (right) and the variable $Y = n/s$ (left) as a function of temperature (bottom) and time (top) for a P-wave annihilating dark matter with mass 100 GeV. The dashed line shows the equilibrium values. The solid line is for an annihilation cross section which gives the correct relic density today and the cross section for each shaded region differs by one order of magnitude from cross sections for the adjacent regions. The cross section increases from top to bottom, so the higher the annihilation cross section is, the smaller the present cold relic density is.

$$\sigma = \frac{g_{weak}^4}{16\pi^2 m_\chi^2} \tag{A.39}$$

where $g_{weak} = 0.65$ is the weak interaction gauge coupling. At the time of freeze-out, $v \sim 0.3$. Then, coincidentally, σv for a generic weak-scale particle becomes comparable to the value of the annihilation cross section obtained for a cold relic for the particles with mass in the range $\sim$ 100 GeV-1 TeV. This is often called the "WIMP Miracle" (see, e.g [14] for a review) which states that weak-scale particles make excellent dark matter candidates.

A.3.3 Hot Relic Density

The decoupling occurs for a hot relic when it is still relativistic, then using Table (A.1) and Eq. (A.20) we obtain

$$\bar{Y}_X = \frac{45\zeta(3)}{2\pi^4}\epsilon_{\rm FB}\frac{g_X}{q_*}, \tag{A.40}$$

where $\epsilon_{\rm FB} = 1(3/4)$ for bosons (fermions). After decoupling, the interaction is no longer effective since $\bar{Y}_X$ becomes constant and can be approximated by its value at freeze-out. In this case, the relic density depends on the equilibrium value at freeze-out:

$$\rho_{X\circ} = m_X s_\circ \bar{Y}_X(x_f)\ . \tag{A.41}$$

Then, the density parameter becomes

$$\Omega_{X\circ}h^2 = 0.739\left(\frac{m_X}{10{\rm eV}}\right)\frac{\epsilon_{\rm FB}g_X}{q_*(x_f)}\ . \tag{A.42}$$

As an example, the neutrinos which have small mass decouple from the cosmic plasma when $T_\gamma \simeq 1$ MeV and $q_*(x_f) \simeq 10$. Then, if we assume three flavors of neutrinos, Eq. (A.42) gives

$$\Omega_{X\circ}h^2 = \sum_{i=1}^{3}\frac{m_{\nu i}}{90{\rm eV}}\ , \tag{A.43}$$

where $m_{\nu i}$ is the mass of the neutrino with flavor i. However, the tritium β-decay experiments have put an upper limit on the neutrino mass [227],

$$m_\nu < 2.05\ {\rm eV}. \tag{A.44}$$

This limit actually applies to all neutrino mass eigenstates since the mass differences between them are sufficiently small (see Table 3.1). Thus, this implies an upper bound on the total neutrino relic density

$$\Omega_{\nu\circ}h^2 \leq 0.07\ , \tag{A.45}$$

which means that neutrinos can not account for the dark matter alone. A more stringent constraint on the neutrino relic density was obtained from the analysis of

CMB anisotropies, suggesting that the neutrinos can only compose 2% of the total density of the Universe [10, 11]. This excludes neutrinos from being a viable dark matter candidate.

If the relic particles are slightly massive and decouple from the plasma at $T_f \simeq 300$ GeV ($q_* \simeq 107$), we get

$$\Omega_{X\circ} h^2 = \frac{m_X}{900\text{eV}} \tag{A.46}$$

These particles with moderate masses are called warm relics which also have a very small relic abundance.

APPENDIX B

CAPTURE RATES IN ASTROPHYSICAL OBJECTS

In this chapter we will give a brief review of the theoretical framework of the capture of DM in astrophysical objects following the earlier works by Gould [90, 91]. We first assume the capture by a thin spherical shell with radius r and thickness dr where the escape velocity is v and the velocity of DM is w. The DM is assumed to have an isotropic velocity distribution $f(u)du$ far from the gravitational field. Then, the conservation of energy implies $w^2 = u^2 + v^2$. The inward flux of DM across a large imaginary surface with radius R can be calculated as

$$dF = \frac{2\pi R^2 d(cos\theta)}{4\pi R^2} u\cos(\theta) f(u)du = \frac{1}{4} f(u)u\ du\ d(\cos^2\theta) \quad 0 \leq \theta \leq \frac{\pi}{2}, \tag{B.1}$$

where θ is the angle between u and the radial direction. In order to find the differential number (dN) of DM particles entering the region per unit time, one can use the change of variable from θ to the angular momentum per unit mass,

$$J = Ru\ \sin(\theta) \tag{B.2}$$

and integrate Eq. (B.1) over the surface area to get

$$dN = \pi \frac{f(u)}{u}\ du\ dJ^2\ . \tag{B.3}$$

After finding the number of DM particles entering the region per unit time, one can find the fraction of these being captured by the spherical shell at radius r. In order for the capture to occur inside the shell, DM velocity w must scatter to a velocity less than v during its passage. The event rate for that process is quantified by the term $\Omega_v(w)$. For a spherical shell, it is easy to show that the time span (Δt) inside the shell (with thickness Δr) by a DM particle is given as

$$\Delta t = \frac{2}{w}\left[1-\left(\frac{J}{rw}\right)^2\right]^{-1/2}\Delta r\Theta(J_{\max}-J)\ , \tag{B.4}$$

where $J_{\max} = rw$ is the maximum possible value for the angular momentum per unit mass. Then, the differential capture rate ($dC = \Omega_v(w)\Delta t dN$) can be written in the form by using Eqs.(B.3) and (B.4),

$$dC = \frac{2\pi f(u)}{uw}\Omega_v(w)\left[1-\left(\frac{J}{rw}\right)^2\right]^{-1/2}\Theta(J_{\max}-J)\ du\ dr\ dJ^2\ . \tag{B.5}$$

After integrating over all angular momenta,

$$dC = 4\pi r^2 w\Omega_v(w)\frac{f(u)}{u}\ du\ dr\ . \tag{B.6}$$

Thus, the total capture rate per unit volume reads

$$\frac{dC}{dV} = \int_0^\infty du\frac{f(u)}{u}w\Omega_v(w)\ . \tag{B.7}$$

Now, suppose the shell is composed of nuclei with mass m_N, number density n and a DM particle with mass m_χ enters in the shell. The interaction cross section is σ which is assumed to be velocity independent. From simple kinematics, the maximum energy loss of a DM particle after colliding with a nucleus is given as

$$\left(\frac{\Delta E}{E}\right)_{\max} = \frac{4m_\chi m_N}{(m_\chi+m_N)^2} = \frac{\mu}{\mu_+^2} \tag{B.8}$$

where

$$\mu = \frac{m_\chi}{m_N},\quad \mu_\pm = \frac{\mu\pm 1}{2} \tag{B.9}$$

and by requiring that the initial velocity w reduce to a value less than v after the scattering, the energy loss must be at least

$$\left(\frac{\Delta E}{E}\right)_{\min} = \frac{u^2}{w^2}\ . \tag{B.10}$$

Hence, the distribution of the energy loss is uniform in the given interval. Then, using the rate of scattering $\sigma n w$, the conditional probability

$$P = \frac{(\Delta E/E)_{\max}-(\Delta E/E)_{\min}}{(\Delta E/E)_{\max}} \tag{B.11}$$

and the relation $\Omega_v(w) = P\sigma nw$, one can obtain

$$w\Omega_v(w) = \frac{\sigma n v^2}{A^2}(A^2 - x^2)\Theta(A - x) \ , \tag{B.12}$$

where $\Theta(A-x)$ appears from the requirement $(\Delta E/E)_{\max} > (\Delta E/E)_{\min}$ and

$$x^2 = \frac{M}{2k_BT}u^2, \quad A^2 = \frac{3}{2}\frac{v^2}{\overline{v}^2}\frac{\mu}{\mu_-^2}, \quad \overline{v}^2 \equiv \frac{3k_BT}{M} \ . \tag{B.13}$$

Here, the velocity dispersion ($\overline{v}$) is defined in terms of the DM temperature (T), and $k_B = 1.38 \times 10^{-23}$J/K is the Boltzmann constant.

If DM with number density n_χ is assumed to have a Maxwell-Boltzmann distribution in the form

$$f(u)du = n_\chi \frac{4}{\pi^{1/2}}x^2 exp(-x^2)dx, \tag{B.14}$$

for an observer at rest with respect to the GC, the capture rate becomes

$$\frac{dC}{dV} = \left(\frac{6}{\pi}\right)^{1/2}\sigma n n_\chi \overline{v}\frac{v^2}{\overline{v}^2}\left[1 - \frac{1 - exp(-A^2)}{A^2}\right] \ . \tag{B.15}$$

The motion of the observer affects the capture rate; the faster the observer moves, the harder to capture the DM since the average kinetic energy of the particles increases in that frame. In that respect, the correction factor which accounts for the motion of the observer is defined:

$$\xi_\eta(A) \equiv \frac{dC_\eta(A)/dV}{dC(A)/dV} \ , \tag{B.16}$$

where η is the dimensionless observer velocity for an observer moving with velocity $\tilde{v}$,

$$\eta^2 \equiv \frac{M}{2k_BT}\tilde{v}^2 \ . \tag{B.17}$$

A typical value expected for the DM velocity dispersion $\overline{v} \simeq 300$km/s suggests that $\eta \sim 1$ for the astrophysical objects in our solar system since the solar system orbits the GC at $\tilde{v} \simeq 250$km/s. It was shown in Ref. [90] that the limiting values of $\xi_\eta(A)$ for $\eta = 1$ are $\xi_\eta(\infty) = 0.75$ and $\xi_\eta(0) = 0.37$.

For convenience, one can define a dimensionless quantity ϕ which is related to the gravitational potential at the shell and to the escape velocity at the surface of the astrophysical object, $v_{\rm esc}$,

$$\phi = \frac{v^2}{v_{\rm esc}^2} \, . \tag{B.18}$$

Including the effect of the motion of the observer, the total capture rate can be written as (the brackets $\langle\rangle$ indicate averaging over the volume of the object)

$$C = \left(\frac{6}{\pi}\right)^{1/2} \sigma n n_\chi \frac{v_{\rm esc}^2}{\overline{v}} \langle\phi\rangle [\xi_\eta(\infty)] \langle S(A)\rangle \, , \tag{B.19}$$

where $\langle S(A)\rangle$ is the suppression factor due to the mismatching of the masses of DM particle and the nucleus;

$$S(A) = \frac{\phi}{\langle\phi\rangle} \left(1 - \frac{1 - exp(-A^2)}{A^2}\right) \frac{\xi_\eta(A)}{\xi_\eta(\infty)} \, . \tag{B.20}$$

For example, if $m_N \simeq m_\chi$ then $A \to \infty$ and $\langle S(A)\rangle$ approaches to 1 but becomes considerably small when the two masses differ from each other. In general, the astrophysical objects are composed of more than one nuclear species so the contributions from each species to the capture rate must be taken into account. In the limit $\eta \to 1$, the function $\langle S(A)\rangle$ can be approximated as [197]

$$\langle S(A)\rangle \simeq S(\mu) = \frac{B}{(1 + B^{1.5})^{2/3}} \quad \text{where} \quad B(\mu) = \frac{3}{2} \frac{\mu}{(\mu - 1)^2} \left(\frac{\langle v_{esc}\rangle}{\bar{v}}\right)^2 \tag{B.21}$$

and $\mu \equiv m_\chi / M_N$. The quantity $\langle v_{esc}\rangle$ is the mean escape velocity; $\langle v_{esc}\rangle = 1156$km s^{-1} for the Sun and $\langle v_{esc}\rangle = 13.2$km s^{-1} for the Earth [197]. Therefore, for the given local density (ρ^χ), velocity distribution ($\overline{v}$) of the DM particles with mass m_χ, and the DM-nucleus interaction cross section (σ_0^i) for the ith nucleus with mass m_{N_i} and mass fraction f_i relative to the Sun (or the Earth), the total capture rate reduces to [91, 197]

$$C = c \frac{\rho_{0.3}^\chi}{(m_\chi / GeV) \overline{v}_{270}} \sum_i f_i \, \langle\phi_i\rangle \, S_i(\mu) \frac{\sigma_0^i}{10^{-8}\text{pb}} \frac{1\text{GeV}}{m_{N_i}}, \tag{B.22}$$

where

$$\rho^{\chi}_{0.3} = \frac{\rho^{\chi}}{0.3\ \mathrm{GeV/cm}^3}\,, \qquad \overline{v}_{270} = \frac{\overline{v}}{270\ \mathrm{km/s}} \tag{B.23}$$

and

$$c = \begin{cases} 4.8 \times 10^{11}\mathrm{s}^{-1} & \text{Earth,} \\ 4.8 \times 10^{20}\mathrm{s}^{-1} & \text{Sun.} \end{cases} \tag{B.24}$$

So far we have assumed that the interaction cross sections are velocity independent and the DM interacts with the nuclei coherently. This assumption is valid only if the interaction is not affected by the internal structure of the nucleus, i.e the momentum transfer, q is small compared to the inverse of the nuclear radius, R

$$qR \ll \hbar\ . \tag{B.25}$$

In the cases when Eq. (B.25) is not satisfied, the coherence of the interaction is lost and the capture becomes less efficient. In general, the lack of coherence in interactions with nuclear material is described by a form-factor suppression, $|F(q^2)|^2$ in the form [90, 91]

$$|F(q^2)|^2 = exp(-\Delta E/E_0) \tag{B.26}$$

where ΔE represents the energy loss of DM and

$$E_0 \equiv \frac{3\hbar^2}{2m_N R^2} \tag{B.27}$$

is the characteristic coherence energy. The introduction of lack of coherence modifies the definition of the scattering function, $\Omega_v(w)$ so now it is defined as

$$\Omega_v(w) = (\sigma n w) \int_{\Delta_{\min}}^{\Delta_{\max}} \frac{1}{\Delta_{\max}} exp(-\Delta E/E_0) d\left(\frac{2\Delta E}{m_\chi w^2}\right) \tag{B.28}$$

where $\Delta_{\max} = (\Delta E/E)_{\max}$ and $\Delta_{\min} = (\Delta E/E)_{\min}$ are given in Eqs. (B.11) and (B.10) respectively. It was shown that the form factor suppression is not more than a 5% effect for the capture of DM in the Earth [197]. In the context of form factor suppression for the capture of DM in the Sun, the earlier results of Gould [90] were

used and a fairly accurate analytic fit was obtained by Jungman, Kamionkowski and Griest [197], i.e

$$F_i(m_\chi) = F_i^{inf} + (1 - F_i^{inf}) exp\left[- \left(\frac{ln\, m_\chi}{ln\, m_c^i} \right)^{\alpha_i} \right] \tag{B.29}$$

for a DM particle with mass m_χ interacting with a nucleus of type i. The fit parameters F_i^{inf}, m_c^i and α_i can be found in [197]. Then, the total capture rate, after including the form factor suppression, takes the form

$$C = c \frac{\rho_{0.3}^\chi}{(m_\chi / GeV)\overline{v}_{270}} \sum_i F_i(m_\chi)\, f_i\, \langle \phi_i \rangle\, S_i(\mu) \frac{\sigma_0^i}{10^{-8}\text{pb}} \frac{1\text{GeV}}{m_{N_i}} \,. \tag{B.30}$$

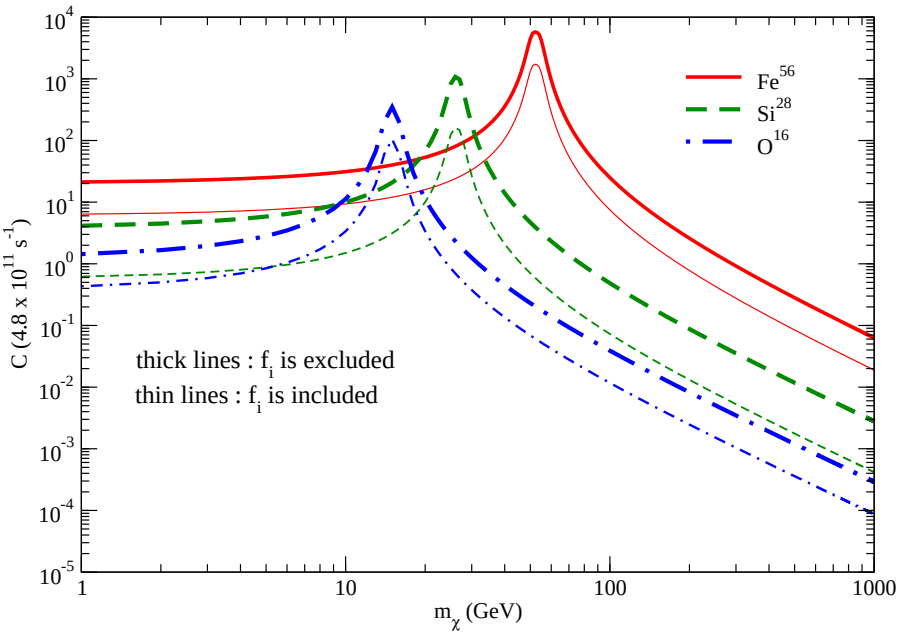

Figure B.1: Capture Rate in the core of the Earth as a function of dark matter mass m_χ. Contributions from different nuclei; iron (solid line), silicon (dashed line) and oxygen (dot-dashed line) are considered when the actual mass fractions are taken (thin lines) and also when the core of the Earth is assumed to contain single type of nucleus (thick lines).

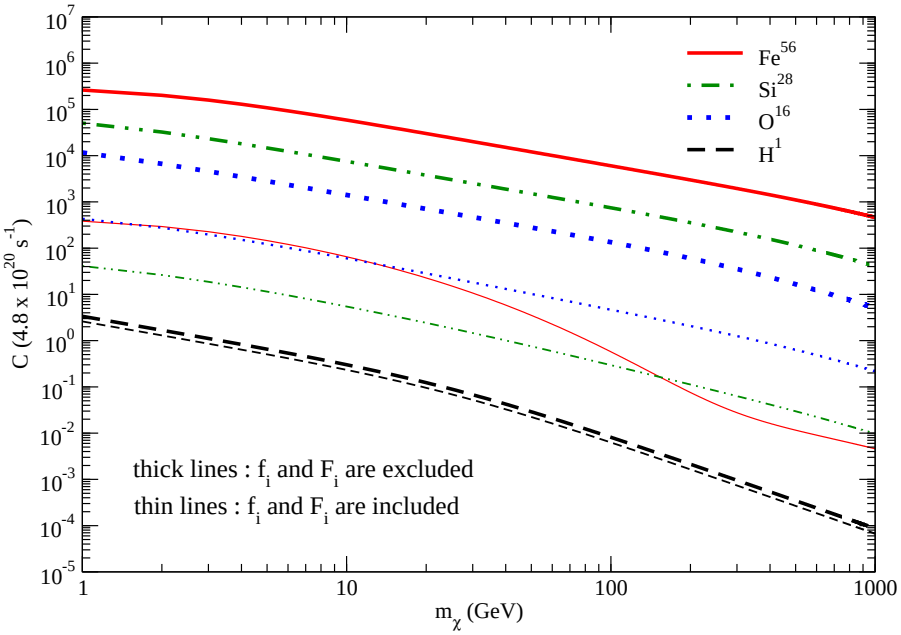

Figure B.2: Capture Rate in the core of the Sun as a function of dark matter mass m_χ. Contributions from different nuclei; iron (solid line), silicon (dot-dashed line), oxygen (dotted line) and hydrogen (dashed line) are considered when the mass fraction and lack of coherence in DM-nucleus interaction effects are included (thin lines) and when these effects are ignored (thick lines).

In Figs. B.1 and B.2 we present the contribution of several different nuclei to the total capture rate in the Earth and in the Sun, respectively. In each case, we assume that DM-nucleus cross section can be approximated, for a nucleus with N_i nucleons, as

$$\sigma_0^i \simeq \sigma_0 N_i^4 \tag{B.31}$$

where DM-nucleon cross section is taken to be 10^{-8}pb. Furthermore, we take the composition of the Earth and the Sun given in [197].

In Fig. B.1, we show the capture rates due to oxygen, silicon and iron nuclei in the Earth for the case when $f_i = 1$ (thick lines) and when the actual mass fractions given in Ref. [197] are taken into account (thin lines). The effect of the kinematic

factor $S(\mu)$ is observed as resonance peaks when the DM mass and the mass of the nucleus are the same. In a wide range of DM masses, the contribution to the capture rate from the iron nucleus seems more effective than from the other nuclei except in the resonance regions.

In Fig. B.2, we show the capture rates due to oxygen, silicon, iron and hydrogen nuclei in the Sun. We present the capture rates due to each nucleus in the case when we take $f_i = F_i = 1$ (thick lines) and in the case when f_i and F_i take their actual values (thin lines) given in Ref. [197]. It is very important to note that even if the hydrogen is the most abundant element ($f_i \sim 0.8$) in the Sun, due to nature of the scalar interactions given in Eq.(B.31), heavier nuclei turn out to be more effective in capturing DM. In addition, the form factor suppression exhibits a large effect on the iron nucleus especially for DM particles with mass, $m_\chi > 10$ GeV. For DM masses below 20 GeV, both oxygen and iron nuclei are important in the capture, however, for heavier DM particles the main contribution to the total capture rate comes from oxygen. Unlike the case for the Earth, we do not observe any resonance behaviours for the capture in the Sun. This is due to the large mean escape velocity for the Sun which renders the kinematic suppression ($S(\mu)$) negligible, independent of the ratio of the DM and the nucleus masses. It is worthwhile to note that in the case of scalar (or spin-independent) DM-nucleus interactions, neglecting the contributions from heavy nuclei in the capture process does not seem a reasonable assumption which is frequently used in the literature [15, 36, 42].

REFERENCES

[1] F. Zwicky. Spectral displacement of extragalactic nebulae. *Helv. Phys. Acta*, 6:110, 1933.

[2] F. Zwicky. On the masses of nebulae and of clusters of nebulae. *Astrophys. J.*, 86:217, 1937.

[3] A. Borriello and P. Salucci. The dark matter distribution in disk galaxies. *MNRAS*, 323:285, 2001.

[4] M. Tegmark. Cosmological parameters from SDSS and WMAP. *Phys. Rev.*, D69:103501, 2004.

[5] D. N. Spergel *et al.* [WMAP Collaboration]. First year Wilkinson Microwave Anisotropy Probe (WMAP) observations: determination of cosmological parameters. *Astrophys. J. Suppl.*, 148:175, 2003.

[6] D. N. Spergel *et al.* [WMAP Collaboration]. Wilkinson Microwave Anisotropy Probe (WMAP) three year results: implications for cosmology. *Astrophys. J. Suppl.*, 170:170, 2007.

[7] A. G. Sanchez *et al.* Cosmological parameters from CMB measurements and the final 2dFGRS power spectrum. *MNRAS*, 366:189, 2006.

[8] S. Perlmutter *et al.* Measurement of Ω and Λ from 42 high-z supernovae. *Astrophys. J.*, 517:565, 1999.

[9] A. G. Riess *et al.* Observational evidence from supernovae for an accelerating Universe and a cosmological constant. *Astron. J.*, 116:1009, 1998.

[10] E. Komatsu *et al.* [WMAP Collaboration]. Five-year Wilkinson Microwave Anisotropy Probe (WMAP) observations: cosmological interpretation. *Astrophys. J. Suppl.*, 180:330, 2009.

[11] E. Komatsu *et al.* [WMAP Collaboration]. Seven-year Wilkinson Microwave Anisotropy Probe (WMAP) observations: cosmological interpretation. arXiv:1001.4538.

[12] M. Tegmark *et al.* [SDSS Collaboration]. The 3-D power spectrum of galaxies from the SDSS. *Astrophys. J.*, 606:702, 2004.

[13] P. Peter and J. P. Uzan. The standard Big-Bang model. In *Primordial Cosmology*. Oxford University Press, 2009.

[14] J. L. Feng. Dark matter candidates from particle physics and methods of detection. arXiv:1003.0904.

[15] V. Barger, W. Y. Keung, G. Shaughnessy, and A. Tregre. High energy neutrinos from neutralino annihilations in the Sun. *Phys. Rev.*, D76:095008, 2007.

[16] D. Hooper and E. A. Baltz. Strategies for determining the nature of dark matter. *Ann. Rev. Nucl. Part. Sci.*, 58:293, 2008.

[17] G.'t Hooft. Recent developments in gauge theories. In *Proceedings of NATO Advanced Study Institute*, volume B59, page 135, (Plenum, New York, 1980).

[18] H. Baer and X. Tata. Dark matter and the LHC. arXiv:0805.1905.

[19] G. B. Gelmini. Search for dark matter. *Int. J. Mod. Phys.*, A23:4273, 2008.

[20] W. B. Atwood *et al.* [Collaboration]. The Large Area Telescope on the Fermi Gamma-ray telescope mission. *Astrophys. J.*, 697:1071, 2009.

[21] C. Boehm, D. Hooper, J. Silk, M. Casse, and J. Paul. MeV dark matter: Has it been detected? *Phys. Rev. Lett.*, 92:101301, 2004.

[22] P. Jean *et al.* Early SPI/INTEGRAL measurements of 511 keV line emission from the 4th quadrant of the Galaxy. *Astron. Astrophys.*, 407:L55, 2003.

[23] D. Hooper, D. P. Finkbeiner, and G. Dobler. Possible evidence for dark matter annihilations from the excess microwave emission around the center of the Galaxy seen by the Wilkinson Microwave Anisotropy Probe . *Phys. Rev.*, D76:083012, 2007.

[24] F. Aharonian *et al.* [HESS Collaboration]. Very high energy gamma rays from the direction of Sagittarius A*. *Astron. Astrophys.*, 425:L13, 2004.

[25] E. O. Wilhelmi [HESS Collaboration]. Status of the HESS telescope. *AIP Conf. Proc.*, 1112:16, 2009.

[26] S. Chang and L. Goodenough. A new approach to searching for dark matter signals in Fermi-LAT gamma rays. *JCAP*, 1008:035, 2010.

[27] C. Goy [AMS Collaboration]. Indirect search for dark matter with AMS. *J. Phys. Conf. Ser.*, 39:185, 2006.

[28] M. Aguilar *et al.* [AMS-01 Collaboration]. Cosmic-ray positron fraction measurement from 1 to 30-GeV with AMS-01. *Phys. Lett.*, B646:145, 2007.

[29] S. W. Barwick *et al.* [HEAT Collaboration]. Measurements of the cosmic ray positron fraction from 1-GeV to 50-GeV. *Astrophys. J.*, 482:L191, 1997.

[30] I. Cholis, G. Dobler, D. P. Finkbeiner, L. Goodenough, and N. Weiner. The case for a 700+ GeV WIMP: cosmic ray spectra from ATIC and PAMELA. *Phys. Rev.*, D80:123518, 2009.

[31] K. Yoshida *et al.* Cosmic-ray electron spectrum above 100-GeV from PPB-BETS experiment in Antarctica. *Adv. Space Res.*, 42:1670, 2008.

[32] F. Aharonian *et al.* [HESS Collaboration]. Probing the ATIC peak in the cosmic-ray electron spectrum with HESS. *Astron. Astrophys.*, 508:561, 2009.

[33] A. A. Abdo *et al.* [Fermi LAT Collaboration]. Measurement of the cosmic ray e+ plus e- spectrum from 20 GeV to 1 TeV with Fermi Large Area Telescope. *Phys. Rev. Lett.*, 102:181101, 2009.

[34] P. Meade, M. Papucci, A. Strumia, and T. Volansky. Dark matter interpretations of the e+- excesses after Fermi. *Nucl Phys.*, B831:178, 2010.

[35] P. Crotty. High energy neutrino fluxes from supermassive dark matter. *Phys. Rev.*, D66:063504, 2002.

[36] D. Hooper and J. Silk. Searching for dark matter with neutrino telescopes. *New J. Phys.*, 6:23, 2004.

[37] A. Achterberg *et al.* Limits on the muon flux from neutralino annihilations at the center of the Earth with AMANDA. *Astropart. Phys.*, 26:129, 2006.

[38] M. Ackermann *et al.* Limits to the muon flux from neutralino annihilations in the Sun with the AMANDA detector. *Astropart. Phys.*, 24:459, 2006.

[39] D. Hubert [IceCube Collaboration]. Neutralino dark matter searches with neutrino telescopes: AMANDA results and IceCube prospects. *Nucl. Phys. Proc. Suppl.*, B173:87, 2007.

[40] F. Halzen and D. Hooper. The indirect search for dark matter with IceCube. *New J. Phys.*, 11:105019, 2009.

[41] U. F. Katz [KM3NeT Collaboration]. Status of the KM3NeT project. *Nucl. Instrum. Meth.*, A602:40, 2009.

[42] D. Hooper and G. D. Kribs. Probing Kaluza-Klein dark matter with neutrino telescopes. *Phys. Rev.*, D67:055003, 2003.

[43] G. Bertone, E. Nezri, J. Orloff, and J. Silk. Neutrinos from dark matter annihilations at the Galactic center. *Phys. Rev.*, D70:063503, 2004.

[44] F. Halzen and J. E. Jacobsen. The detection of cold dark matter with neutrino telescopes. arXiv:hep-ph/9406309.

[45] M. Blennow, H. Melbeus, and T. Ohlsson. Neutrinos from Kaluza-Klein dark matter in the Sun. *JCAP*, 1001:018, 2010.

[46] T. Flacke, A. Menon, D. Hooper, and K. Freese. Kaluza-Klein dark matter and neutrinos from annihilation in the Sun. arXiv:0908.0899.

[47] D. Spolyar, M. Buckley, K. Freese, D. Hooper, and H. Murayama. High energy neutrinos as a test of leptophilic dark matter. arXiv:0905.4764.

[48] S. Andreas, M. H. G. Tytgat, and Q. Swillens. Neutrinos from inert doublet model. *JCAP*, 0904:004, 2009.

[49] K. Griest, M. Kamionkowski, and M. S. Turner. Supersymmetric dark matter above the W mass. *Phys. Rev.*, D41:3565, 1990.

[50] G. Wikstrom and J. Edsjo. Limits on the WIMP-nucleon scattering cross section from neutrino telescopes. *JCAP*, 0904:009, 2009.

[51] M. Blennow, J. Edsjo, and T. Ohlsson. Neutrinos from WIMP annihilations using a full three-flavor Monte Carlo. *JCAP*, 0801:021, 2008.

[52] M. Lindner, A. Merle, and V. Niro. Enhancing dark matter annihilation into neutrinos. arXiv:1005.3116.

[53] C. Delaunay, P. J. Fox, and G. Perez. Probing dark matter dynamics via Earthborn neutrinos at IceCube. *JHEP*, 0905:099, 2009.

[54] S. M. Koushiappas and M. Kamionkowski. Galactic substructure and energetic neutrinos from the Sun and the Earth. *Phys. Rev. Lett.*, 103:2009, 121301.

[55] G. Jungman and M. Kamionkowski. Neutrinos from particle decay in the Sun and Earth. *Phys. Rev.*, D51:328, 1995.

[56] S. Ritz and D. Seckel. Detailed neutrino spectra from cold dark matter annihilations in the sun. *Nucl. Phys.*, B304:877, 1988.

[57] J. Edsjo. Neutrino-induced muon fluxes from neutralino annihilations in the Sun and in the Earth. *Nucl. Phys. Proc. Suppl.*, 43:265, 1995.

[58] M. Kamionkowski. Energetic neutrinos from heavy-neutralino annihilation in the Sun. *Phys. Rev.*, D44:3021, 1991.

[59] L. Covi, M. Grefe, A. Ibarra, and D. Tran. Neutrino signals from dark matter decay. *JCAP*, 1004:017, 2010.

[60] L. Covi, M. Grefe, A. Ibarra, and D. Tran. Unstable gravitino dark matter and neutrino flux. *JCAP*, 0901:029, 2009.

[61] J. Hisano, M. Kawasaki, K. Kohri, and K. Nakayama. Neutrino signals from annihilating/decaying dark matter in the light of recent measurements of cosmic ray electron/positron fluxes. *Phys. Rev.*, D79:043516, 2009.

[62] S. K. Mandal, M. R. Buckley, K. Freese, D. Spolyar, and H. Murayama. Cascade Events at IceCube+DeepCore as a definitive constraint on the dark matter interpretation of the PAMELA and Fermi Anomalies. *Phys. Rev.*, D81:043508, 2010.

[63] E. Athanassoula, F. S. Ling, E. Nezri, and R. Teyssier. Gamma ray and neutrinos fluxes from a cosmological dark matter simulation. *Astropart. Phys.*, 31:37, 2009.

[64] J. Hisano, K. Nakayama, and M. J. S. Yang. Upward muon signals at neutrino detectors as a probe of dark matter properties. *Phys. Lett.*, B678:101, 2009.

[65] M. R. Buckley, K. Freese, D. Hooper, D. Spolyar, and H. Murayama. High-energy neutrino signatures of dark matter decaying into leptons. *Phys. Rev.*, D81:016006, 2010.

[66] J. Liu, P. F. Yin, and S. H. Zhu. Prospects for detecting neutrino signals from annihilating/decaying dark matter to account for the PAMELA and ATIC results. *Phys. Rev.*, D79:063522, 2009.

[67] C. Wiebusch [IceCube Collaboration]. Physics capabilities of the IceCube DeepCore detector. arXiv:0907.2263.

[68] R. Abbasi *et al.* [IceCube Collaboration]. The IceCube data acquisition system: signal capture, digitization, and timestamping. *Nucl. Instrum. Meth.*, A601:294, 2009.

[69] R. Abbasi *et al.* [IceCube Collaboration]. The first search for extremely-high energy cosmogenic neutrinos with the IceCube Neutrino Observatory. *Phys. Rev.*, D82:072003, 2010.

[70] A. E. Erkoca, M. H. Reno, and I. Sarcevic. Muon Fluxes from dark matter annihilation. *Phys. Rev.*, D80:043514, 2009.

[71] A. E. Erkoca, G. Gelmini, M. H. Reno, and I. Sarcevic. Muon fluxes and showers from dark matter annihilation in the galactic center. *Phys. Rev.*, D81:096007, 2010.

[72] A. E. Erkoca, M. H. Reno, and I. Sarcevic. Probing dark matter models with neutrinos from the galactic center. *Phys. Rev.*, D82:113006, 2010.

[73] R. Abbasi *et al.* The energy spectrum of atmospheric neutrinos between 2 and 200 TeV with AMANDA-II detector. *Astropart. Phys.*, 34:48, 2010.

[74] L. Bergstrom, T. Bringmann, M. Eriksson, and M. Gustafsson. Gamma rays from Kaluza-Klein dark matter. *Phys. Rev. Lett.*, 94:131301, 2005.

[75] G. Servant and T. M. P. Tait. Is the lightest Kaluza-Klein particle a viable dark matter candidate? *Nucl. Phys.*, B650:391, 2003.

[76] P. J. Fox and E. Poppitz. Leptophilic dark matter. *Phys. Rev.*, D79:083528, 2009.

[77] V. Barger, Y. Gao, W. Y. Keung, D. Marfatia, and G. Shaughnessy. Dark matter and pulsar signals for Fermi LAT, PAMELA, ATIC, HESS and WMAP data. *Phys. Lett.*, B678:283, 2009.

[78] R. Harnik and G. D. Kribs. An effective theory of dirac dark matter. *Phys. Rev.*, D79:095007, 2009.

[79] Q. H. Cao, E. Ma, and G. Shaughnessy. Dark matter: The leptonic connection. *Phys, Lett.*, B673:152, 2009.

[80] B. Kyae. PAMELA/ATIC anomaly from the meta-stable extra dark matter component and the leptophilic Yukawa interaction. *JCAP*, 0907:028, 2009.

[81] D. J. Phalen, A. Pierce, and N. Weiner. Cosmic ray positrons from annihilations into a new, heavy lepton. *Phys. Rev.*, D80:063513, 2009.

[82] H. S. Goh, L. J. Hall, and P. Kumar. The leptonic higgs as a messanger of dark matter. *JHEP*, 0905:097, 2009.

[83] A. Ibarra, A. Ringwald, D. Tran, and C. Weniger. Cosmic rays from leptophilic dark matter decay via kinetic mixing. *JCAP*, 0908:017, 2009.

[84] A. Ibarra, D. Tran, and C. Weniger. Decaying dark matter in light of the PAMELA and Fermi LAT data. *JCAP*, 1001:009, 2010.

[85] A. Ibarra and D. Tran. Gamma ray spectrum from gravitino dark matter decay. *Phys. Rev. Lett.*, 100:061301, 2008.

[86] W. Buchmuller, A. Ibarra, T. Shindou, F. Takayama, and D. Tran. Probing gravitino dark matter with PAMELA and Fermi. *JCAP*, 0909:021, 2009.

[87] B. Bajc, T. Enkhbat, D. K. Ghosh, G. Senjanovic, and Y. Zhang. MSSM in view of PAMELA and Fermi-LAT. *JHEP*, 1005:048, 2010.

[88] E. Resconi [IceCube Collaboration]. Status and prospects of the IceCube neutrino telescope. *Nucl. Instrum. Meth.*, A602:7, 2009.

[89] J. Ahrens *et al.* Sensitivity of the IceCube detector to astrophysical sources of high energy muon neutrinos. *Astropart. Phys.*, 20:507, 2004.

[90] A. Gould. Resonant enhancements in weakly interacting massive particle capture by the Earth. *Astrophys. J.*, 321:571, 1987.

[91] A. Gould. Cosmological density of WIMPs from solar and terrestrial annihilations. *Astrophys. J.*, 388:338, 1992.

[92] J. F. Navarro, C. S. Frenk, and S. D. M. White. The structure of cold dark matter halos. *Astrophys. J.*, 462:563, 1996.

[93] A. Klypin, H. Zhao, and R. S. Somerville. Lambda CDM-based models for the Milky Way and M31 I: Dynamical models . *Astrophys. J.*, 573:597, 2002.

[94] B. Moore, T. Quinn, F. Governato, J. Stadel, and G. Lake. Cold collapse and the core catastrophe. *MNRAS*, 310:1147, 1999.

[95] A. V. Kravtsov, A. A. Klypin, J. S. Bullock, and J. R. Primack. The cores of dark matter dominated galaxies: Theory versus observations. *Astrophys. J.*, 502:48, 1998.

[96] L. Bergstrom, P. Ullio, and J. H. Buckley. Observability of gamma-rays from dark matter neutralino annihilations in the Milky Way halo. *Astropart. Phys.*, 009:137, 1998.

[97] J. N. Bahcall, M. Schmidt, and R. M. Soneira. The Galactic Spheroid. *Astrophys. J.*, 265:730, 1983.

[98] J. Einasto. Dark Matter. arXiv:0901.0632.

[99] N. Bahcall. Clusters and superclusters of galaxies. arXiv:astro-ph/9611148.

[100] A. A. Penzias and R. W. Wilson. A measurement of excess antenna temperature at 4080 Mc/s. *Astrophys. J.*, 142:419, 1965.

[101] G. F. Smooth *et al.* Structure in the COBE differential microwave radiometer first-year maps. *Astrophys. J. Lett.*, 396:L1, 1992.

[102] C. L. Bennett *et al.* Four year COBE DMR Cosmic Microwave Background Observations: Maps and Basic results. *Astrophys. J. Lett.*, 464:L1, 1996.

[103] A. Melchiorri *et al.* A measurement of Ω from the North American Test Flight of Boomerang. *Astrophys. J.*, 536:L63, 2000.

[104] E. M. Leitch *et al.* DASI three-year cosmic microwave background polarization results. *Astrophys. J.*, 624:10, 2005.

[105] J. L. Sievers *et al.* Cosmological Parameters from Cosmic Background Imager observations and comparisons with BOOMERANG, DASI, and MAXIMA. *Astrophys. J.*, 591:599, 2003.

[106] G. Bertone, D. Hooper, and J. Silk. Particle dark matter: Evidence, candidates and constraints. *Phys. Rept.*, 405:279, 2005.

[107] J. Angle *et al.* [XENON Collaboration]. First results from the XENON10 dark matter experiment at the Gran Sasso National Laboratory. *Phys. Rev. Lett.*, 100:021303, 2008.

[108] Z. Ahmed *et al.* [CDMS Collaboration]. Search for weakly interacting massive particles with the first five-tower data from cryogenic dark matter search at the Soudan Underground Laboratory. *Phys. Rev. Lett.*, 102:011301, 2009.

[109] Z. Ahmed *et al.* [CDMS Collaboration]. Results from the final exposure of the CDMS II experiment. arXiv:0912.3592.

[110] R. Bernabei *et al.* [DAMA Collaboration]. First results from DAMA/LIBRA and the combined results with DAMA/NaI. *Eur. Phys. J.*, C56:333, 2008.

[111] G. B. Gelmini. Theory of dark matter. arXiv:1009.1942.

[112] J. Rico *et al.* [MAGIC Collaboration]. Status and recent results of MAGIC. *AIP Conf. Proc.*, 1112:23, 2009.

[113] J. Holder *et al.* Status of the VERITAS Observatory. *AIP Conf. Proc.*, 1085:657, 2009.

[114] R. Enomoto [for the CANGAROO Collaboration]. Status of CANGAROO-III. *AIP Conf. Proc.*, 1085:661, 2009.

[115] D. J. Thompson. Gamma ray astrophysics: the EGRET results. *Rept. Prog. Phys.*, 71:116901, 2008.

[116] O. Adriani *et al.* [PAMELA Collaboration]. An anomalous positron abundance in cosmic rays with energies 1.5-100 GeV. *Nature*, 458:607, 2009.

[117] J. Chang *et al.* An excess of cosmic ray electrons at energies of 300-800 GeV. *Nature*, 456:362, 2008.

[118] P. Blasi. The origin of the positron excess in cosmic rays. *Phys. Rev. Lett.*, 103:051104, 2009.

[119] P. Mertsch and S. Sarkar. Testing astrophysical models for the PAMELA positron excess with cosmic ray nuclei. *Phys. Rev. Lett.*, 103:081104, 2009.

[120] D. Hooper, P. Blasi, and P. D. Serpico. Pulsars as the sources of high energy cosmic ray positrons. *JCAP*, 0901:025, 2009.

[121] P. D. Serpico. On the possible causes of a rise with energy of the cosmic ray positron fraction. *Phys Rev.*, D79:021302, 2009.

[122] H. Yuksel, M. D. Kistler, and T. Stanev. TeV gamma rays from Geminga and the origin of the GeV positron excess. *Phys. Rev. Lett.*, 103:051101, 2009.

[123] G. Kane, R. Lu, and S. Watson. PAMELA satellite data as a signal of non-thermal wino LSP dark matter. *Phys. Lett.*, B681:151, 2009.

[124] M. Kamionkowski, S. M. Koushiappas, and M. Kuhlen. Galactic substructure and dark matter annihilation in the milky way halo. *Phys. Rev.*, D81:043532, 2010.

[125] J. Hisano, S. Matsumoto, and M. M. Nojiri. Explosive dark matter annihilation. *Phys. Rev. Lett.*, 92:031303, 2004.

[126] N. Arkani-Hamed, D. P. Finkbeiner, T. R. Slatyer, and N. Weiner. A theory of dark matter. *Phys. Rev.*, D79:015014, 2009.

[127] J. M. Russell and S. M. West. WIMPonium and boost factors for indirect dark matter detection. *Phys. Lett.*, B676:133, 2009.

[128] J. M. Russell, S. M. West, D. Cumberbatch, and D. Hooper. Heavy dark matter through the Higgs portal. *JHEP*, 0807:058, 2008.

[129] L. Bergstrom. Dark matter candidates. *New J. Phys.*, 11:105006, 2009.

[130] I. Cholis, L. Goodenough, D. Hooper, M. Simet, and N. Weiner. High energy positrons from annihilating dark matter. *Phys. Rev.*, D80:123511, 2009.

[131] O. Adriani *et al.* A new measurement of the antiproton-to-proton flux ratio up to 100 GeV in the cosmic radiation. *Phys. Rev. Lett.*, 102:051101, 2009.

[132] A. Kappes [IceCube Collaboration]. News from the South Pole: recent results from the IceCube and AMANDA neutrino telescopes. *Nucl. Phys.*, A827:567, 2009.

[133] E. Middell, J. McCartin, and M. D'Agostino [IceCube Collaboration]. Status and Prospects of the IceCube neutrino telescope. Proceedings of the 31st ICRC (2009).

[134] F. Halzen and S. R. Klein. Invited Review Article: IceCube: An instrument for neutrino astronomy. *Rev. Sci. Instrum.*, 81:081101, 2010.

[135] K. Garrett and G. Duda. Dark Matter: A primer. arXiv:1006.2483.

[136] M. Kawasaki, K. Kohri, and T. Moroi. Big Bang nucleosynthesis and hadronic decay of long-lived massive particles. *Phys. Rev.*, D71:083502, 2005.

[137] M. Pospelov. Particle physics catalysis of thermal Big Bang Nucleosynthesis. *Phys. Rev. Lett.*, 98:231301, 2007.

[138] K. Hamaguchi *et al.* . *Phys. Lett. B*, 650:268, 2007.

[139] T Appelquist, H. C. Cheng, and B. A. Dobrescu. Bounds on universal extra dimensions. *Phys. Rev.*, D64:035002, 2001.

[140] D. Hooper and K. M. Zurek. The PAMELA and ATIC signals from Kaluza-Klein dark matter. *Phys. Rev.*, D79:103529, 2009.

[141] R. Davis. Nobel Lecture: A half-century with solar neutrinos. *Rev. Mod. Phys.*, 75:985, 2003.

[142] M. Calicchio *et al.* [MACRO Collaboration]. Status of the MACRO experiment at Gran Sasso. *Nucl. Instrum. Meth.*, A264:18, 1988.

[143] W. Rhode *et al.* [Frejus Collaboration]. Limits on the flux of very high-energy neutrinos with the Frejus detector. *Astropart. Phys.*, 4:217, 1996.

[144] M. A. Markov. On high energy neutrino physics. *in Proceedings of the X International Conference on high energy physics*, Rochester University Department of Physics, Interscience, New York:579, 1960.

[145] R. Bionta *et al.* [IMB Collaboration]. Observation of a Neutrino Burst in Coincidence with Supernova SN 1987a in the Large Magellanic Cloud. *Phys. Rev. Lett.*, 58:1494, 1987.

[146] K. Hirata *et al.* [Kamiokande Collaboration]. Observation of a Neutrino Burst from the Supernova SN 1987a. *Phys. Rev. Lett.*, 58:1490, 1987.

[147] Y. Fukuda *et al.* The Super-Kamiokande detector. *Nucl. Instrum. Meth.*, A501:418, 2003.

[148] J. Boger *et al.* [SNO Collaboration]. The Sudbury neutrino observatory. *Nucl. Instrum. Meth.*, A449:172, 2000.

[149] A. B. McDonald, C. Spiering, S. Schonert, E. T. Kearns, and T. Kajita. Astrophysical neutrino telescopes. *Rev. Sci. Instrum.*, 75:293, 2004.

[150] P. Coyle. The ANTARES deep-sea neutrino telescope: Status and first results. arXiv:1002.0754.

[151] J. Babson *et al.* [DUMAND Collaboration]. Cosmic-ray muons in the deep ocean. *Phys. Rev.*, D42:3613, 1990.

[152] V. Aynutdinov *et al.* [BAIKAL Collaboration]. Search for a diffuse flux of high-energy extraterrestrial neutrinos with the nt200 neutrino telescope. *Astropart. Phys.*, 25:140, 2006.

[153] P. A. Rapidis *et al.* [NESTOR Collaboration]. The NESTOR underwater neutrino telescope project. *Nucl. Instrum. Meth.*, A602:54, 2009.

[154] S. Aiello *et al.* [NEMO Collaboration]. Measurement of the atmospheric muon flux with the NEMO Phase-1 detector. *Astropart. Phys.*, 33:263, 2010.

[155] J. J. Hernandez-Rey. Neutrino telescopes in the Mediterranean sea. *J. Phys. Conf. Ser.*, 171:012047, 2009.

[156] J. A. Aguilar *et al.* [ANTARES Collaboration]. First results of the instrumentation line for the deep-sea ANTARES neutrino telescope. *Astropart. Phys.*, 26:314, 2006.

[157] E. Migneco. Progress and latest results from Baikal, Nestor, NEMO and KM3NeT. *J. Phys. Conf. Ser.*, 136:022048, 2008.

[158] R. Abbasi *et al.* [IceCube Collaboration]. Limits on a muon flux from neutralino annihilations in the Sun with the IceCube 22-string detector. *Phys. Rev. Lett.*, 102:201302, 2009.

[159] W. Pauli. Dear radioactive ladies and gentlemen. *Phys. Today*, 31N9:27, 1978.

[160] J. Chadwick. Possible existence of neutron. *Nature*, 129:312, 1932.

[161] E. Fermi. An attempt of a theory of beta radiation. 1. *Z. Phys.*, 88:161, 1934.

[162] C. L. Cowan, F. Reines, F. B. Harrison, H. W. Kruse, and A. D. McGuire. Detection of the free neutrino: A Confirmation. *Science*, 124:103–104, 1956.

[163] G. Danby et al. Observation of high-energy neutrino reactions and the existence of two kinds of neutrinos. *Phys. Rev. Lett.*, 9:36–44, 1962.

[164] Martin L. Perl et al. Evidence for anomalous lepton production in e+ e- annihilation. *Phys. Rev. Lett.*, 35:1489–1492, 1975.

[165] K. Kodama et al. Observation of tau-neutrino interactions. *Phys. Lett.*, B504:218–224, 2001.

[166] C. Quigg. Gauge Theories of the strong, weak and electromagnetic interactions. *Front. Phys.*, 56:1–334, 1983.

[167] Y. Fukuda *et al.* Evidence for oscillation of atmospheric neutrinos. *Phys. Rev. Lett.*, 81:1562, 1998.

[168] B. Pontecorvo. Mesonium and antimesonium. *Sov. Phys. JETP*, 6:429, 1957.

[169] Z. Maki, M. Nakagawa, and S. Sakata. Remarks on the unified model of elementary particles. *Prog. Theor. Phys.*, 28:870, 1962.

[170] C. B. Bratton et al. Angular distribution of events from SN1987A. *Phys. Rev.*, D37:3361, 1988.

[171] K. S. Hirata et al. Observation in the Kamiokande-II Detector of the Neutrino Burst from Supernova SN 1987a. *Phys. Rev.*, D38:448–458, 1988.

[172] John N. Bahcall, P. I. Krastev, and A. Yu. Smirnov. Where do we stand with solar neutrino oscillations? *Phys. Rev.*, D58:096016, 1998.

[173] B. Aharmim *et al.* Electron energy spectra, fluxes, and day-night asymmetries of B-8 solar neutrinos from the 391-day salt phase SNO data set. *Phys. Rev.*, C72:055502, 2005.

[174] Y. Ashie *et al.* Evidence for an oscillatory signature in atmospheric neutrino oscillation. *Phys. Rev. Lett.*, 93:101801, 2004.

[175] C. Bemporad. Results from CHOOZ. *Nucl. Phys. Proc. Suppl.*, 77:159, 1999.

[176] M. C. Gonzalez-Garcia. Phenomenology with massive neutrinos. *Phys. Rept.*, 460:1, 2008.

[177] L. Wolfenstein. Neutrino Oscillations in matter. *Phys. Rev.*, D17:2369, 1978.

[178] S. P. Mikheyev and A. Y. Smirnov. Resonant neutrino oscillations in matter. *Prog. Part. Nucl. Phys.*, 23:41, 1989.

[179] H. W. Zaglauer and K. H. Schwarzer. The mixing angles in matter for three generations of neutrinos and the MSW mechanism. *Z. Phys.*, C40:273, 1988.

[180] C. W. Kim and W. K. Sze. Adiabatic resonant oscillations of solar neutrinos in three generations. *Phys. Rev*, D35:1404, 1987.

[181] A. S. Joshipura and M. V. N. Murthy. Analytic conditions for three neutrino resonant oscillations in matter. *Phys. Rev.*, D37:1374, 1988.

[182] T. Ohlsson and H. Snellman. Three flavor neutrino oscillations in matter. *J. Math. Phys.*, 42:2345, 2001.

[183] T. Ohlsson and H. Snellman. Neutrino oscillations with three flavors in matter of varying density. *Eur. Phys. J.*, C20:507, 2001.

[184] P. Osland and T. T. Wu. Solar MSW effect with three generations of neutrinos. *Phys. Rev.*, D62:013008, 2000.

[185] M. Cirelli *et al.* Spectra of neutrinos from dark matter annihilations. *Nucl. Phys.*, B790:338, 2008.

[186] A. Strumia and F. Vissani. Neutrino masses and mixings and ... arXiv:hep-ph/0606054.

[187] A. M. Dziewonski and D. L. Anderson. Preliminary reference earth model. *Phys. Earth Planet. Interiors*, 25:297–356, 1981.

[188] J. N. Bahcall and R. K. Ulrich. Solar Models, neutrino experiments and helioseismology. *Rev. Mod. Phys.*, 60:297, 1988.

[189] R. Gandhi, C. Quigg, M. H. Reno, and I. Sarcevic. Ultra-high energy neutrino interactions. *Astropart. Phys.*, 5:81, 1996.

[190] S. I. Dutta, M. H. Reno, and I. Sarcevic. Tau neutrinos underground: Signals of muon-neutrino —> tau neutrino oscillations with extragalactic neutrinos. *Phys. Rev.*, D62:123001, 2000.

[191] P. Lipari. Lepton spectra in the earth's atmosphere. *Astropart. Phys.*, 1:195, 1993.

[192] G. Moreau and M. Chemtob. R-parity violation and the cosmological gravitino problem. *Phys. Rev.*, D65:024033, 2001.

[193] T. K. Gaisser and M. Honda. Flux of atmospheric neutrinos. *Ann. Rev. Nucl. Part. Sci.*, 52:153, 2002.

[194] R. Enberg, M. H. Reno, and I. Sarcevic. Prompt neutrino fluxes from atmospheric charm. *Phys. Rev.*, D78:043005, 2008.

[195] M. Honda, T. Kajita, K. Kasahara, S. Midorikawa, and T. Sanuki. Calculation of atmospheric neutrino flux using the interaction model calibrated with atmospheric muon data. *Phys. Rev.*, D75:043006, 2007.

[196] P. Salucci, F. Nesti, G. Gentile, and C. F. Martins. The dark matter density at the Sun's location. arXiv:1003.3101.

[197] G. Jungman, M. Kamionkowski, and K. Griest. Supersymmetric dark matter. *Phys. Rept.*, 267:195, 1996.

[198] G. Gelmini, P. Gondolo, and E. Roulet. Neutralino dark matter searches. *Nucl. Phys.*, B351:623, 1991.

[199] K. Griest and D. Seckel. Cosmic asymmetry, neutrinos and the Sun. *Nucl. Phys.*, B296:1034, 1988.

[200] S. Eidelman *et al.* Review of particle physics. *Phys. Lett.*, B592:1, 2004.

[201] D. Groom, N. Mokhov, and S. Striganov. Muon stopping power and range tables 10-MeV to 100-TeV. *Atomic Data and Nuclear Data Tables*, 78:183, 2001.

[202] P. Lipari and T. Stanev. Propagation of Multi-TeV muons. *Phys. Rev.*, D44:3543, 1991.

[203] S. I. Dutta, M. H. Reno, I. Sarcevic, and D. Seckel. Propagation of muons and taus at high energies. *Phys. Rev.*, D63:094020, 2001.

[204] E. V. Bugaev, A. Misaki, V. A. Naumov, T. S. Sinegovskaya, S. I. Sinegovsky, and N Takahashi. Atmospheric muon flux at sea level, underground and underwater. *Phys. Rev.*, D58:054001, 1998.

[205] M. C. Gonzalez-Garcia, F. Halzen, and S. Mohapatra. Identifying Galactic PeVatrons with neutrinos. *Astropart. Phys.*, 31:437, 2009.

[206] M. C. Gonzalez-Garcia, F. Halzen, and M. Maltoni. Physics reach of high-energy and high-statistics icecube atmospheric neutrino data. *Phys. Rev.*, D71:093010, 2005.

[207] S. Desai *et al.* [Super-K Collaboration]. Search for dark matter WIMPs using upward through-going muons in Super-Kamiokande. *Phys. Rev.*, D70:109901, 2004.

[208] D. Hooper and G. Servant. Indirect detection of Dirac right-handed neutrino dark matter. *Astropart. Phys.*, 24:231, 2005.

[209] V. Barger, W. Y. Keung, and G. Shaughnessy. Monochromatic neutrino signals from dark matter annihilation. *Phys. Lett.*, B664:190, 2008.

[210] F. Halzen and D. Hooper. Prospects for detecting dark matter with neutrino telescopes in light of recent results from direct detection experiments. *Phys. Rev.*, D73:123507, 2006.

[211] E. Behnke *et al.* [COUPP Collaboration]. Improved Spin-Dependent WIMP limits from a Bubble Chamber. *Science*, 319:933, 2008.

[212] G. J. Alner *et al.* [UK Dark Matter Collaboration]. Limits on WIMP cross-sections from the NAIAD experiment at the Boulby Underground Laboratory. *Phys. Lett.*, B616:17, 2005.

[213] J. Kopp, T. Schwets, and J. Zupan. Global interpretation of direct dark matter searches after CDMS-II results. *JCAP*, 1002:014, 2010.

[214] D. S. Akerib *et al.* [CDMS Collaboration]. Limits on spin-dependent wimp-nucleon interactions from the cryogenic dark matter search. *Phys. Rev.*, D73:011102, 2006.

[215] J. Angle *et al.* [XENON Collaboration]. Limits on spin-dependent WIMP-nucleon cross sections from the XENON10 experiment. *Phys. Rev. Lett.*, 101:091301, 2008.

[216] G. J. Alner, *et al.* ZEPLIN-II limits on WIMP-nucleon interactions. *AIP Conf. Proc.*, 1166:218, 2009.

[217] H. S. Lee *et al.* [KIMS Collaboration]. Limits on WIMP-nucleon cross section with Csl(Tl) crystal detectors. *Phys. Rev. Lett.*, 99:091301, 2007.

[218] J. Hisano, M. Kawasaki, K. Kohri, and K. Nakayama. Positron/Gamma-ray signatures of dark matter annihilation and Big-Bang nucleosynthesis. *Phys. Rev.*, D80:029907, 2009.

[219] J. Hisano, M. Kawasaki, K. Kohri, T. Moroi, and K. Nakayama. Cosmic rays from dark matter annihilation and Big-Bang nucleosynthesis. *Phys. Rev.*, D79:083522, 2009.

[220] D. Suematsu, T. Toma, and T. Yoshida. Enhancement of the annihilation of dark matter in a radiative seesaw model. *Phys. Rev.*, D82:013012, 2010.

[221] C. Arina, F. X. Josse-Michaux, and N. Sahu. Constraining Sommerfeld enhanced annihilation cross sections of dark matter via direct searches. *Phys. Lett.*, B691:219, 2010.

[222] X. J. Bi, X. G. He, and Q. Yuan. Parameters in a class of leptophilic models from PAMELA, ATIC and Fermi. *Phys. Lett.*, B678:168, 2009.

[223] S. Baek and P. Ko. Phenomenology of U(1)(L(mu)-L(tau)) charged dark matter at PAMELA and colliders. *JCAP*, 0910:011, 2009.

[224] J. Kumar, J. G. Learned, and S. Smith. Light dark matter detection prospects at neutrino experiments. *Phys. Rev.*, D80:113002, 2009.

[225] J. F. Beacom, N. F. Bell, and G. D. Mack. Upper bounds on the dark matter total annihilation cross section. *Phys. Rev. Lett.*, 99:231301, 2007.

[226] H. Yuksel, S. Horiuchi, J. F. Beacom, and S. Ando. Neutrino constraints on the dark matter total annihilation cross section. *Phys. Rev.*, D76:123506, 2007.

[227] C. Weinheimer. The neutrino mass direct measurements. In *Proceedings of 10th International Workshop on Neutrino Telescopes, Venice, Italy*, 2003.